DOE/ET-0065/7

Damage Analysis and Fundamental Studies

Quarterly Progress Report
July-October, 1979

November 1979

U.S. Department of Energy
Assistant Secretary for Energy Technology
Office of Fusion Energy

Available from:

National Technical Information Service (NTIS)
U.S. Department of Commerce
5285 Port Royal Road
Springfield, Virginia 22161

Price: Printed copy: $9.00
Microfiche: $3.00

DOE/ET-0065/7
UC-20,20c

Damage Analysis and Fundamental Studies

Quarterly Progress Report
July-October, 1979

November 1979

U.S. Department of Energy
Assistant Secretary for Energy Technology
Office of Fusion Energy
Washington, D.C. 20545

FOREWORD

This report is the seventh in a series of Quarterly Technical Progress Reports on *"Damage Analysis and Fundamental Studies"* (DAFS) which is one element of the Fusion Reactor Materials Program, conducted in support of the Magnetic Fusion Energy Program of the U. S. Department of Energy. Other elements of the Materials Program are:

- Alloy Development for Irradiation Performance (ADIP)
- Plasma-Materials Interaction (PMI)
- Special Purpose Materials (SPM).

The DAFS program element is a national effort composed of contributions from a number of National Laboratories and other government laboratories, universities, and industrial laboratories. It was organized by the Materials and Radiation Effects Branch, Office of Fusion Energy, DOE, and a Task Group on *Damage Analysis and Fundamental Studies* which operates under the auspices of that Branch. The purpose of this series of reports is to provide a working technical record of that effort for the use of the program participants, for the fusion energy program in general, dnd for the Department of Energy.

This report is organized along topical lines in parallel to a Program Plan of the same title (DOE/ET-0032/2) so that activities and accomplishments may be followed readily, relative to that Proyram Plan. Thus, the work of a given laboratory may appear throughout the report. Separate chapters report the work that is specific to each of the subtasks around which the program is structured: A. Environmental Characterization, B. Damage Production, and C. Damage Microstructure Evolution and Mechanical Behavior. The Table of Contents is annotated for the convenience of the reader.

This report has been compiled and edited under the guidance of the Chairman of the Task Group on *Damage Analysis and Fundamental Studies*, D. G. Doran, Hanford Engineering Development Laboratory, and his efforts, those of the supporting staff of HEDL and the many persons who made technical contributions are gratefully acknowledged. M. M. Cohen, Materials and Radiation Effects Branch, is the Department of Energy counterpart to the Task Group Chairman and has responsibility for the OAFS Proyram within DOE.

Klaus M. Zwilsky, Chief
Materials and Radiation
Effects Branch
Office of Fusion Energy

CONTENTS

	Page
Foreword	iii
Figures	xi
Tables	xvii
CHAPTER 1. IRRADIATION TEST FACILITIES	1
1. Rotating Target Neutron Source (RTNS)-II Operations (LLL)	3

A tabulation is given of experiments performed to date. System improvements have reduced down-time and maintenance costs. Large target (hence, highest flux) operation is delayed until at least summer of 1980.

2. Nuclear Data for FMIT (HEDL)	7
A. Deuteron and Neutron Induced Activation of FMIT Accelerator, Beam Transport, and Target Materials	8

Initial measurements have been made of the activation of FMIT structural materials by 35 MeV deuterons.

B. Neutron Cross Sections for Transport Calculations	9

The inclusion of appropriate self-shielding has significantly improved multi-group cross sections for iron used in transport calculations.

C. Neutron Transport Measurements	9

Plans are proceeding for measurement of the transport of high energy neutrons through a massive iron target to check calculational tools.

CONTENTS (Cont'd)

Page

D. Cross Section Prediction 10

A study of the systematics of angular distributions has yielded a useful set of differential cross section parameters.

E. Microscopic Neutron Yield Model 12

Backward angle data have been included in the analysis of microscopic Li(d,n) yields.

CHAPTER 2. SUBTASK A: ENVIRONMENTAL CHARACTERIZATION 15

1. Experiments at the Oak Ridge Research Reactor (ANL) 17

Preliminary dosimetry results are presented for the MFE1 experiment in core location C7 of the Oak Ridge Research Reactor. Whereas the thermal flux at a given row is isotropic, a steep fast flux gradient from South to North is indicated. The total flux is about 50-60% lower than neutronics calculations and the spectrum is much softer than measured previously in core position E7, apparently due to differences in the core loading.

2. Helium Accumulation Neutron Dosimetry for the Be(d,n) Irradiation Environment (RIES) 22

Helium analyses have been completed for several additional Be(d,n)-irradiated helium accumulation dosimetry segments, and an initial Be(d,n) fluence map has been constructed.

CONTENTS (Cont'd)

3. FMIT Damage Parameter Sensitivity Study (HEDL) 32

Hemispherical reflectors could increase the high flux volume from a D-Li source but most of the useful test volume would be sacrificed.

4A. Use of the Magnetic Fusion Energy Computer Center (BNL) 36

The RSIC version of MORSE has been converted for use on the NMFECC 7600 and CRAY computers. Unexplained differences in results from the two machines have been observed.

46. Damage Analysis (BNL) 38

The evaluation of ionization-assisted processes for producing displacement damage in insulators is being evaluated.

5. Development of the STAYSL Computer Code (ANL) 41

Variance-covariance cross-section and flux files have been created for the STAYSL computer code, and it has been interfaced with our SPECTER code to generate errors in all calculated damage parameters.

CONTENTS (Cont'd)

CHAPTER 3. SUBTASK B: DAMAGE PRODUCTION 41

1A. The Time Dependence of Defect Configurations in a Collision Cascade (LLL) 50

Dynamic computer simulations of collision cascades in tungsten show recombination by defect migration that is an order of magnitude larger than predicted from equilibrium transport theory.

1B. In-Situ Creep Testing Juring Irradiation with High-Energy Neutrons (LLL) 55

The first in-situ creep experiment was conducted at RTNS-II; transient creep effects were observed in niobium irradiated at 550°C.

2. Displacement Functions for Polyatomic Materials (LASL) 61

A multi-parameter analytic fit to displacement functions for polyatomic materials has been developed.

3. RTNS-II Irradiation Program (HEDL) 65

Binary alloys based on Cu and Ni and micro-tensile specimens of stainless steel, Ni, and Ti6Al4V have been prepared for irradiation at RTNS-II during the next quarter.

CONTENTS (Cont'd)

CHAPTER 4. SUBTASK C: DAMAGE MICROSTRUCTURE EVOLUTION AND MECHANICAL BEHAVIOR 71

1. Swelling and Cavity Growth in Simultaneously Bombarded 316 SS (W-R&D) 74

Simultaneous bombardment of 316 SS with Si and He at 500-750°C to several dpa produced swelling that correlated with cavity growth; an enormous swelling rate was observed in solution annealed material ut 600°C. Evidence is given relating cavity alignment to the formation of acicular precipitates, and rapid cavity growth to solute segregation.

2. The Radiation Induced Order/Disorder Transformation in Cu_3Au (U. Wisconsin) 88

A model is given for radiation disordering and radiation-enhanced ordering. It is shown to fit all available order versus dose data for Cu_3Au using one set of diffusion parameters.

3. Temperature Dependence of Swelling in Single- and Dual-Ion Irradiated 316 Stainless Steel (ANL) 128

In solution annealed and aged MFE 316 stainless steel, two swelling peaks were found for dual-ion irradiated samples, while only one peak was observed for single-ion irradiations of helium-preinjected samples.

CONTENTS (Cont'd)

4. The Effect of Pulsed Irradiation on Microstructure Evolution (HEDL) 138

The model used to describe microstructural evolution during cyclical irradiation was modified to include transients at the beginning and end of each pulse.

5. The Occurrence of Deformation Twinning During Tensile Testing of Type 316 Stainless Steel Irradiated by Helium Ions (U. Virginia) 154

Elevated temperatures or helium irradiation can promote the formation of deformation twins in stainless steel pulled to fracture; neutron irradiation does not.

FIGURES

Page

CHAPTER 1

2D. Cross Section Prediction

FIGURE 1. A Comparison of Calculated Angular Distributions with Measurements of Inelastic Scattering of Protons by Iron 11

CHAPTER 2

2. Helium Accumulation Neutron Dosimetry for the Be(d,n) Irradiation Environment

FIGURE 1. Cross Sectional View of the Be(d,n) Inner Irradiation Package 23

FIGURE 2. Measured Helium Concentrations in Be(d,n)-Irradiated Pure Element Ring Segments 24

FIGURE 3. Ring Segment Helium Concentrations Normalized to Initial Be(d,n) Fluence Map 27

FIGURE 4. Contours of Constant Fluence for Midplane of Top Helium-Generation Specimen Layer in Be(d,n)-Irradiated Inner Package 28

4A. Use of the Magnetic Fusion Energy Computer Center

FIGURE 1. Neutron Spectra Generated by the RSIC Version of MORSE on the MFECC 7600 and CRAY Computers 39

FIGURE 2. Gamma-Ray Spectra Generated by the RSIC Version of MORSE on the MFECC 7600 and CRAY Computers 39

5. Development of the STAYSL Computer Code

FIGURE 1. STAYSL Results for the Oak Ridge Research Reactor 45

FIGURES (Cont'd)

Page

CHAPTER 3

1A. The Time Dependence of Defect Configurations in a Collision Cascade

FIGURE 1. The Time Development of Two Collision Cascades 53

FIGURE 2. Defect Jump Rates During the Development of a 2.5 keV Collision Cascade 54

1B. In-Situ Creep Testing During Irradiation with High-Energy Neutrons 55

FIGURE 3. Beam On-Bean Off In-Situ Creep Test of Niobium at 550°C 57

3. RTNS-II Irradiation Program

FIGURE 1. Micro-Tensile Specimens of Stainless Steel Which Will be Irradiated in HEDL Experiment No. 4 at RTNS-II G7

FIGURE 2. Closeup of Gripping Mechanism of the Micro-Tensile Specimen Uniaxial Test Device 68

CHAPTER 4

1A. Swelling and Cavity Growth in Simultaneously Bombarded 316 SS

FIGURE 1. Swelling as a Function of Temperature for 20% Cold-Worked 316 SS 75

FIGURE 2. ;lean Cavity Diameters for Both SA and 20% CR 316 SS at tlie Various Experimental Temperatures 76

FIGURE 3. Swelling as a Function of Temperature for SA 316 SS with Representative Microstructures 77

FIGURES (Cont'd)

1B. Postulated Origin of Cavity Alignment in SA 316 SS at 600°C

FIGURE 4. Microstructures Induced in SA 316 SS at a Relatively Low Damage Rate (2.9 x 10^{-5}dpa/s) and Moderate He Level 79

FIGURE 5. Postulated Precipitation Sequence, Producing Cavity Alignment, in SA 316 SS 80

FIGURE 6. Cavity and Precipitate Microstructures in SA 316 SS Simultaneously Bombarded at 600°C 82

FIGURE 7. Coniparison of Energy Dispersive X-Ray Analyses Obtained in the Matrix and at a Cavity/Precipitate Interface 83

2. The Radiation Induced Order/Disorder Transformation in Cu_3Au

FIGURE la. The Rate of Change of Order as a Function of Order Parameter S Under Fast Neutron Irradiation at 27°C 96

FIGURE lb. As for Figure la but at 302°C 97

FIGURE 2. The Enhanced Steady-State Vacancy Concentration Caused by Fast Neutron Irradiation Versus Reciprocal Temperature 98

FIGURE 3. The Order/Disorder Rate Under Fast Neutron Irradiation as a Function of Reciprocal Temperature for Two Values of S 100

FIGURE 4a. The Steady-State Degree of Order, S, as a Function of Temperature for Fast Neutrons and Thermal Neutrons 101

FIGURE 4b. The Matrix Diffusion Parameters (D_vC_v) for Fast Neutrons as a Function of Temperature 103

FIGURE 4c. As for Figure 4b but for Thermal Neutrons

FIGURES (Cont'd)

Page

FIGURE 5. A Typical Set of Time Dependent Results with the Parameters of Table 1 and $K = 1.4 \times 10^{-9}$ dpa/sec and $\rho = 1.7 \times 10^{13}/m^2$ 106

FIGURE 6. The Resistivity as a Function of Temperature for the Disordered and Ordered States 102

FIGURE 7. The Thermal Equilibrium Order Curve as a Function of Temperature 1151

FIGURE 8a. The Change of Order During Fast Neutron Irradiation of Cu_3Au at 4°K from Kirk and Blewitt 111

FIGURE 8b. The Change of Order During Fast Neutron Radiation of Cu_3Au at 150°C from Kirk and Blewitt 112

FIGURE Sc. As Figure 8b but for a Lower Initial Order Parameter and $\rho_d = 2.7 \times 10^{13}/m^2$ 113

FIGURE 8d. As for Figure 8b but for Thermal Neutron Irradiation at 135°C with $\varepsilon = 20$, $K = 2.5 \times 10^{-10}$ dpa/sec and $\rho_d = 10^{12}/m^2$ 114

FIGURE 9. The Data of Cook and Cushing for Fast Neutron Irradiation at 35°C and 106°C 119

FIGURE 10a.. Order/Disorder Change tinder Thermal Neutron Irradiation at 80°C Measured by Glick et al. Fitted Using $K = 2 \times 10^{-9}$dpa/sec and $\rho_d = 1.5 \times 10^{16}/m^2$ 120

FIGURE 10b The Fast Neutron data of Siegel at 40°C, Fitted Using $K = 3 \times 10^{-9}$ and $\rho_d = 8 \times 10^{14}/m^2$ 121

3. Temperature dependence of Swelling in Single- and Dual-Ion Irradiated 316 Stainless Steel

FIGURE 1. Bright-Field Dark-Field Pairs Showing Precipitate-Coated Cavities in Preinjecced Single-Ion and Oual-Ion Irradiated 316 Stainless Steel 131

FIGURE 2. Absorption Contrast Micrographs of Dual-Ion Irradiated 316 Stainless Steel 132

FIGURES (Cont'd)

		Page
FIGURE 3.	Temperature Dependence of Cavity Number Density in Dual-Ion Irradiated 316 Stainless Steel	133
FIGURE 4.	Temperature Dependence of Cavity Size in Dual-Ion and Preinjected Single-Ion Irradiated 316 Stainless Steel	134
FIGURE 5.	Temperature Dependence of Swelling in Dual-Ion and Preinjected Single-Ion Irradiated 316 Stainless Steel	135
FIGURE 6.	Temperature Dependence of Cavity Number Density in Preinjected Single-Ion Irradiated 316 Stainless Steel	137

4. The Effect of Pulsed Irradiation on Microstructure Evolution

FIGURE 1.	Typical Vacancy and Interstitial Concentration Profiles During an Irradiation Cycle	140
FIGURE 2.	Defect Concentration Profiles During Initial Transient	143
FIGURE 3.	Defect Concentration Profiles During Initial Transient	143
FIGURE 4.	Fluence Dependence of Void Growth for Several Pulse Periods at 540°C	145
FIGURE 5.	Fluence Dependence of Void Growth for Several Pulse Periods at 550°C	145
FIGURE 6.	Fluence Dependence of Void Growth for Several Pulse Periods at 560°C	146
FIGURE 7.	Fluence Dependence of Void Concentration for Several Pulse Periods at 540°C	146
FIGURE 8.	Fluence Dependence of Void Concentration for Several Pulse Periods at 550°C	147

FIGURES (Cont'd)

Page

FIGURE 9. Fluence Dependence of Void Concentration for Several Pulse Periods at 560°C 147

FIGURE 10. Fluence Dependence of Void Swelling for Several Pulse Periods at 540°C 148

FIGURE 11. Fluence Dependence of Void Swelling for Several Pulse Periods at 550°C 14:

FIGURE 12. Fluence dependence of Void Swelling for Several Pulse Periods at 560°C 149

FIGURE 13. Fluence Dependence of Swelling for Several Damage Rates at 550°C 149

FIGURE 14. Fluence Dependence of Void Concentration for Several Damage Rates at 550°C 150

FIGURE 15. Fluence Dependence of Void Growth for Several Damage Rates at 550°C 150

5. The Occurrence of Deformation Twinning During Tensile Testing of Type 316 Stainless Steel Irradiated by Helium Ions

FIGURE 1. Transmission Electron Micrograph of Ligaments Along a Crack Flank in Unirradiated Type 316 Stainless Steel Tensile-Tested at 600°C 156

FIGURE 2. Transmission Electron Micrograph of a Single "Tooth" from Figure 1 158

FIGURE 3. Scanning Electron Micrograph of a Crack Flank in Type 316 Stainless Steel Irradiated with Heliuiii Ions of 80 keV to a Fluence of 3×10^{17} cm^{-2} ana Tensile-Tested at 600°C 161

TABLES

Page

CHAPTER 1

1. Rotating Target Neutron Source (RTNS)-II Operations

TABLE 1. RTNS-II Irradiation Experiments 5

CHAPTER 2

1. Experiments at the Oak Ridge Research Reactor

TABLE 1. Flux Measurements for ORR-MFE 1 19

2. Helium Accumulation Neutron Dosimetry for the Be(d,n) Irradiation Environment

TABLE 1. Be(d,n)-Irradiated Helium Accumulation Neutron Dosimetry Rings 23

TABLE 2. Approximate Relative Helium-Generation Rates of Pure Elements 29

3. FMIT Damage Parameter Sensitivity Study

TABLE 1. Effect of Hemispherical Reflector On Damage Parameters Along the Beam Axis (X,0,0) 34

5. Development of the STAYSL Computer Code

TABLE 1. Comparison of Estimated Cross Section Errors with Integral Test Results for Be(d,n), E_d = 14 - 40 MeV 43

TABLE 2. Damage Parameters for ORR Calculated with STAYSL Flux Covariances 45

TABLES (Cont'd)

Page

CHAPTER 3

1A. The Time Dependence of Defect Configurations in a Collision Cascade

TABLE 1. Coinparison of Fully Dynamic and Binary Calculations for 2.5 keV Cascades in Tungsten 50

CHAPTER 4

2. The Radiation Induced Order/Disorder Transformation in Cu_3Au

TABLE 1. Parameters Used in Fitting Cu_3Au Data 95

4. The Effect of Pulsed Irradiation on Microstructure Evolution

TABLE 1. Defect Concentration Expressions Used in the Current Computer Model 142

CHAPTER 1
IRRADIATION TEST FACILITIES

I. PROGRAM

Title: RTNS-II Operations (WZJ-16)
Principal Investigator: C. M. Logan
Affiliation: Lawrence Livermore Laboratory

11. OBJECTIVE

The objectives of this work are operation of OFE's RTNS-II (a 14-MeV neutron source facility), machine development, and support of the experimental program that utilizes this facility. Experimenter services include dosimetry, handling, scheduling, coordination, and reporting.

111. RELEVANT DAFS PROGRAM TASK / SUBTASK

TASK II.A.2,3,4.
TASK II.B.3,4.
TASK II.C.1,2,6,11,18.

IV. SUMMARY

RTNS-II is dedicated to materials research for the fusion power program. Its primary use is to aid in the development of models of high-energy neutron effects. Such models are needed in interpreting and projecting to the fusion environment engineering data obtained in other neutron spectra.

V. ACCOMPLISHMENTS AND STATUS

A. FY79 Irradiations. - N. E. Ragaini, M. W. Guinan and C. M. Logan. (LLL)

Routine RTNS-II irradiations were begun in mid March 1979. Since that time nine experimental assemblies with over 700 samples have been irradiated. These contained experiments from 14 individuals

representing 10 laboratories. With the exception of an in-situ creep experiment all irradiations were conducted at room temperature.

Table 1 lists these experiments. In addition, a number of calibration runs for dosimetry and beam characterization were also made in February, March and April. The start of each experiment is indicated as well as the final completion date. In many cases the maximum fluences listed were accumulated in a number of separate runs, between which other experiments were run. The fluences listed are all based on the $^{93}Nb(n,2n)^{92m}Nb$ reaction using a cross-section of 463 mb.[1] The approximate fluences given in the last column are based on rough dosimetry results prior to history corrections while those in parentheses are target fluences for experiments in progress or for which counting has not yet been completed.

B. RTNS-II Status - C. M. Logan and D. W. Heikkinen (LLL)

A number of significant improvements have been made in accelerator and target systems which will improve machine reliability. X-rays resulting largely from stopping of back-streaming electrons daiiiage fibre optics and threaten solid state electronics. We have installed local shielding in the high-voltage terminal to protect vulnerable components; thereby reducing machine down-time and maintenance costs. Work continues on the beam-spot monitoring system. We have improved neutron source and accelerator diagnostics. Complete time-history information of neutron production is now recorded and used for dosimetry analysis. The target bearing lubrication systein has been improved resulting in longer bearing life and improved reliability.

Stainless steel beam pipe has proven susceptible to damage from very short bursts of beam. We have replaced all four-inch beam pipe with water-cooled copper.

Severe problems continue to plague the development of large

TABLE I

RTNS-II IRRADIATION EXPERIMENTS

DATE START	DATE COMPLETE	MATERIALS IRRADIATED	MEASUREMENT	LABORATORY	MAXIMUM FLUENCE n/cm^2
3/19/79	5/15/79	Ni, Nb & SS	Mechanical properties	PNL	3.4×10^{17}
3/19/79	9/21/79	TFTR Glass	Density & Optical Properties	ANL	$\sim 2 \times 10^{18}$
3/19/79	9/21/79	A15 Superconductors	Transition Temperature Critical Field & Current	BNL/LLL LLL	9×10^{17}
3/19/79	9/21/79	Nb_3Sn	Critical Current		8×10^{17}
3/19/79	10/19/79	Ni, Nb & SS	Mechanical Properties	PNL	(2×10^{18})
4/3/79	4/3/79	Au TEM Foils	Sub-Cascade Structure	ANL	4.9×10^{15}
4/3/79	4/4/79	TFTR SS	Hydrogen Trapping	SANDIA	1.4×10^{16}
4/5/79	4/8/79	Cu, Ni, V, Nb, Ti, & SS TEM Disks	Microstructure / Microhardness	HEDL/UCSB	3.9×10^{17}
6/6/79	6/29/79	CU, Ni, V, Nb, Ti, & SS TEM Disks	Microstructure / Microhardness	HEDL/UCSB	$1\ 2 \times 10^{13}$
6/6/79	6/29/79	Ni-Al & Ni-Si TEM Disks	Nucleation Studies	LLL/ANL	$5\ 4 \times 10^{17}$
7/2/79	7/2/79	Zr_3Al TEM Disks	Cascade Size & Structure	UW/LLL	6.5×10^{15}
8/14/79	8/16/79	Nb	In-Situ Creep 400°-600° C	LLL	7.5×10^{16}
9/24/79	10/5/79	MACOR Ceramic (TFTR Insulators)	Thermal / Mechanical	LASL	$(1 \times 10^{16}$
9/24/79	--	Glass-Bonded Mica (TFTR Insulators)	Thermal / Mechanical	LASL	(1×10^{18})
9/24/79		MACOR Ceramic (TFTR Insulators)	Thermal / Mechanical	LASL	$(1 \times$

(50 cm) targets. Bond quality is inadequate. Initial targets delaminate when pressurized. Large target operation will not occur until at least summer 1980.

VI. REFERENCCS

1. D. R. Nethaway, J. Inorg. Nucl. Chem. 40 1285 (1978).

VII. FUTURE WORK

The anticipated operating schedule for the next quarter is as follows:

Week beginning	
October 15	Jones (PNL)
October 22	Panayotou (HEDL)
October 29	Panayotou (HEDL)
November 5	Maintenance
November 12	Guinan (LLL)
November 19	Pilgrims (USA)
November 26	Barmore (LLL)
Deceiiiber 3	Opperman (HEDL)
December 10	Opperman (HEDL)
December 17	Opperman (HEDL)
December 24	Holiday
January 2	Maintenance
January 7	Clinard/Jesser (LASL/Univ. of Virginia)
January 14	Clinard/Jesser (LASL/Univ. of Virginia)
January 21	Clinard/Jesser (LASL/Univ. of Virginia)
January 28	Install HEDL Furnace

VIII. PUBLICATIONS

None

I. PROGRAM

Title: Nuclear Data for FMIT (WH025/EDK)
Principal Investigator: R. E. Schenter
Affiliation: Hanford Engineering Development Laboratory (HEDL)

II. OBJECTIVE

The objective of this work is to supply nuclear data needed for damage studies and in the design and operation of the Fusion Material Irradiation Testing (FMIT) facility.

111. RELEVANT DAFS PROGRAM PLAN TASK/SUBTASK

All tasks that are relevant *to* FMIT use, with emphasis on:

SLJBTASK	**II.A.2.3**	Flux Spectra Definition in FMIT
TASK	II.A.4	Gas Generation Rates
SUBTASK	II.A.5.1	Helium Accumulation Monitor Development
SUBTASK	II.B.l.2	Acquisition of Nuclear Data

IV. SUMMARY

Measurements of deuteron induced activation of FMIT accelerator, beam transport, and target materials were initiated in order to provide data to optimize design from the standpoint of maintenance.

Multi-group neutron transport cross sections have been supplied to the FMIT architect-engineer for many materials having no previous evaluation for energies above the 20 MeV ENDF/B limit. Improvements in self-shielding corrections have been made.

Plans are proceeding for measurement of the transport of high energy neutrons through a massive iron target to check calculational tools.

The study of the systematics of angular distributions has been completed, yielding a set of useful parameters.

The study of the microscopic Li(d,n) yields is continuing with inclusion of backward angle data.

V. ACCOMPLISHMENTS AND STATUS

A. Deuteron arid Neutron Induced Activation of FMIT Accelerator, Beam Transport, and Target Materials -- D. L. Johnson (HEDL), C. M. Castaneda and M. L. Johnson (U. C. Davis).

Small losses of the deuteron beam will occur during acceleration and transport to the Li target. Activation induced by such losses, as well as activation of the target itself, will provide a significant contribution to gamma radiation fields that will exist during maintenance operations.

Initial measurements of deuteron induced activation were performed by observation of decay gamma rays after bombardment with 35 MeV deuterons at the University of California at Davis. The objective was to measure the production rate in important materials of all significant gamma decaying isotopes with half lives longer than about an hour. The production rate coupled with known decay properties will allow calculations of the radiation dose from irradiated material for any combination of irradiation time and subsequent decay time.

Stacked foil targets were used which will allow determination of the energy dependence of radioisotope production reactions. Measurements were performed on targets of lithium, the FMIT target material; on copper and gold, for the accelerator system; and on carbon, aluminum, tantalum, and lead for possible use in the high energy beam transport system. Additional measurements are planned for other candidate materials that may be activated by deuterons.

B. Neutron Cross Sections for Transport Calculations -- F. M. Mann and R. E. Schenter (HEDL).

When calculating flux in a pure medium using multi-group techniques, great care must be exercised to use the appropriate self-shielded group cross sections. New cross sections have been generated for pure iron using the infinitely dilute iron cross sections from ORNL. The difference in flux, as calculated using the ORNL and HEDL sets, are over two orders of magnitude at 4 feet into the slab. Monte Carlo results confirm that the new HEDL self-shielded cross sections are more appropriate.

The LASL cross section processing system NJOY[1] has largely been converted to the RL UNIVAC 1100144. Coupled neutron-gamma P5 cross section sets have been calculated for Cu, Cd, and Dh, using ENDF/B-V as a data base. Besides multi-group transport sets, the system is capable of producing Monte Carlo sets, kerma factor sets, damage parameter sets, and diffusion theory sets. After HEDL obtains the high speed link to the MFE computer system at LLL, the system will be operated there.

C. Neutron Transport Measurements -- D. L. Johnson (HEDL).

Planning has begun for measurements of the transmission of FMIT neutrons through thick iron. The objective is to confirm neutron transport calculations used for predictions of radiation heating in the FMIT test cell walls. Neutrons are to be produced by 35 MeV deuterons incident on a 2 cm. thick lithium target. The conceptual design of this experiment has the target placed at the center of a sphere of solid iron that is 30 inches in diameter. Neutron spectra will he observed with detectors placed outside the sphere.

A conceptual design of the sphere has been completed and bids for construction have been requested. The design includes penetrating holes for passive dosimeters which will allow the sphere to be used as a bench mark neutron field for passive dosimetry as well as for active dosimetry.

D. Cross Section Prediction -- F. M. Mann (HEDL) and C. Kalbach (Triangle Universities Nuclear Laboratory)

The study of the systematics of experimental angular distributions for particles emitted in the pre-equilibrium phase of nuclear reactions has been completed. Such information will enable the calculation of unmeasured angular distributions for shielding and damage parameter studies.

The work is based on an expansion of the differential cross section in Legendre polynomials and on an unpublished theory by Feshbach, Kerman, and Kawaii. Their theory divides the pre-equilibrium states into two classes, a multi-step compound part (MSC) which is symmetric about 90° and a multi-step direct part (MSD) which is forward peaked. Thus the differential cross section $d\sigma/d\Omega d\varepsilon$ is

$$\frac{d\sigma}{d\Omega d\varepsilon}(\Theta,\varepsilon) = \sigma(\varepsilon)\left[f\sum_{\ell=0}^{\ell_{max}} b_\ell(\varepsilon)\, P_\ell(\cos\Theta) + (1-f)\sum_{\substack{\ell=0\\ \Delta\ell=2}}^{\ell_{max}} b_\ell(\varepsilon) P_\ell(\cos\Theta)\right]$$

where σ is the angle-integrated cross section, and f is the ratio of MSD to MSC contribution. The ratio f is taken from a new version of the pre-equilibrium code PRECO. The $b_\ell(\varepsilon)$ were determined from ^{103}Rh (p,n)[2], ^{109}Ag (p,n)[3], and ^{120}Sn (p,p′)[4] data. The b_ℓ's so determined give very good agreement between calculations and these experiments as well as for ^{54}Fe (p,p′)[4] and a series of proton- and complex particle-induced reactions in the iron region[5]. An example of the agreement is shown in the accompanying Figure 1.

The b_ℓ's are found to be nearly independent of incoming and outgoing particle type, incoming energy, and target type. The main dependence is on the energy of the outgoing particle. The b_ℓ's were given the form

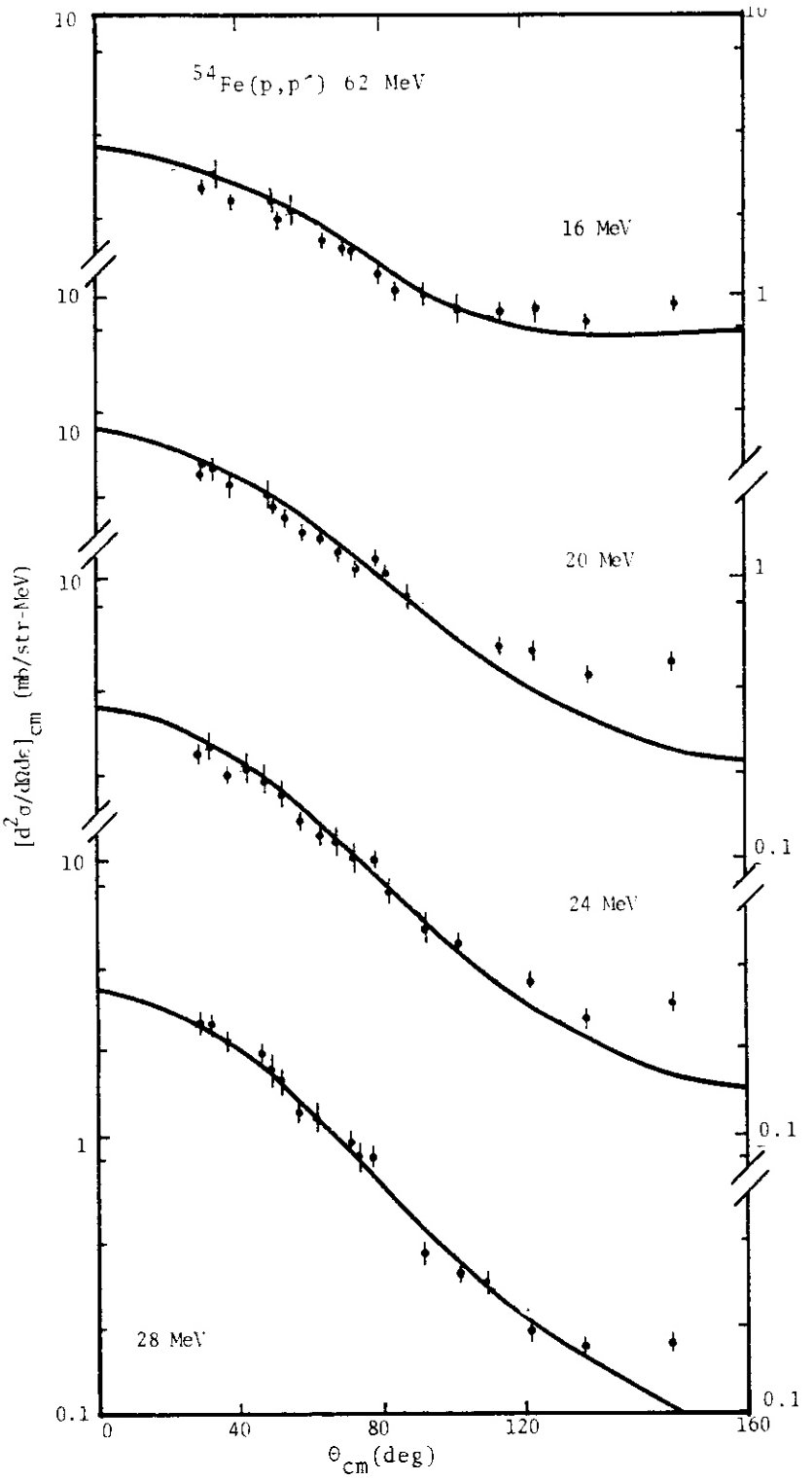

FIGURE 1. A Comparison of Calculated Angular Distributions With Measurements of Inelastic Scattering of Protons by Iron.

$$b_\ell(\varepsilon) = \frac{(2\ell+1)}{1 + \exp\left[A_\ell(B_\ell - \varepsilon)\right]}$$

where A_ℓ and B_ℓ were found to be independent of energy

$$A_\ell = 0.028 + .0042\ \ell(\ell + 1)\ \ \mathrm{MeV}^{-1}$$

and $$B_\ell = 89.6 - 84.4\ \left[\ell(\ell + 1)\right]^{-\frac{1}{2}}\ \ \mathrm{MeV}$$

E. Microscopic Neutron Yield Model -- F. M. Mann and F. Schmittroth (HEDL).

The analysis of Li(d,n) yield data was extended by inclusion of data for angles greater than 90°. Preliminary fits using the FERRET[6] generalized least squares program indicate little change to previous forward angle fits ($\theta < 70°$) when the backward angles are introduced. However, the agreement at backward angles is greatly enhanced.

VI. REFERENCES

1. R. E. MacFarlane, R. J. Barrett, D. W. Muir, and R. M. Boicourt, "The NJOY Nuclear Data Processing System: User's Manual". LA-7584-M Los Alamos Scientific Laboratory, December 1978.
2. C. Kalbach, S. M. Grimes, and C. Wong, Z. Phys. A 275 (1975) 175.
3. S. M. Grimes, J. D. Anderson and C. Wong, Phys. Rev. C 13 (1976) 2224.
4. F. E. Bertrand and R. W. Peele, Phys. Rev. C 8 (1973) 1045.
5. J. Bisplinghoff, J. Ernst, R. Lohr, T. Mayer-Kuckuk, and P. Meyer, Nucl. Phys. A 269 (1976) 147.
6. F. Schmittroth, "Generalized Least-Square for Data Analysis," HEDL-TME 77-51 (1978)

VII. FUTURE WORK

More measurements of deuteron induced activation of FMIT materials will be performed. Results will be compared to previous calculations.

More evaluations of neutron cross sections for transport calculations will be done as needed by the FMIT architect-engineer and for predictions in the FMIT test cell.

Measurements of the transmission of FMIT neutrons through thick iron will be completed.

The computer code HAUSER*5 will be modified to include the study of angular distributions.

The microscopic neutron yield model will be updated to include backward angle data.

VIII. PUBLICATIONS

A paper on nuclear data needs of FMIT will be presented at the International Conference on Nuclear Cross Sections for Technology, Knoxville, Tennessee (October 1979).

CHAPTER 2

SUBTASK A: ENVIRONMENTAL CHARACTERIZATION

I. PROGRAM

Title: Dosimetry and Damage Analysis
Principal Investigator: L. R. Greenwood
Affiliation: Argonne National Laboratory

II. OBJECTIVE

To establish the best practicable dosimetry for mixed-spectrum reactors and to provide dosimetry and damage analysis for MFE experimenters.

III. RELEVANT DAFS PROGRAM TASK/SUBTASK

SUBTASK 11. A.l.l Flux-spectral definition in a tailored fission reactor.

IV. SUMMARY

Preliminary dosimetry results are presented for the MFE 1 experiment in the Oak Ridge Research Reactor (ORR). There appear to be several important differences between the MFE 1 results at full power (30 MW) in core position C7 and the spectral measurements at low power (1 MW) in core position E7, presumably due to differences in fuel loading.

V. ACCOMPLISHMENTS AND STATUS

A. Experiments at the Oak Ridge Research Reactor - -

L. R. Greenwood and R. R. Heinrich (ANL)

Preliminary results are available for the ORR-MFE 1 experiment. The irradiation was conducted in core position C7 between February 13, 1978 and June 28, 1978. The average power level was 22.52 MW over the total

time of 134.7 days; however, the reactor was down for about 25 days during this period. Gamma heating problems early in the run necessitated some changes in the core configuration with unknown effects on our dosimetry experiments.

Four dosimetry wires (Ni, Co-Al, Ti, and Fe) were placed in four aluminuin tubes at the four corners of the 24" long irradiation capsule. One of the four aluminum tubes also contained 107 small helium accumulation fluence monitors (HAFM) which are now being analyzed by H. Farrar IV of Rockwell International (see the previous report in this series, DOE/ET-0065/6).

Six dosiiiietry reactions were analyzed at twelve locations for each group of four wires by cutting each wire into one-inch long segments and Ge(Li) counting every other piece. The reactions which were analyzed included $^{54}Fe(n,p)^{54}Mn$, $^{58}Fe(n,\alpha)^{59}Fe$, $^{58}Ni(n,p)^{58}Co$, $^{60}Ni(n,p)^{60}Co$, $^{59}Co(n,\gamma)^{60}Co$, and $^{46}Ti(n,p)^{46}Sc$. Calculations show that thermal burn-up corrections are severe for ^{58}Co; measurements indicate a 60% reduction in ^{58}Co in the highest flux regions. The $^{58}Ni(n,p)^{58}Co$ reaction thus cannot be used for flux determinations, leaving only five reactions for analysis.

The fluence results for the highest flux region ($\sim$ 3" below midplane) are listed in Table I. As can be seen, the results are distinctly different frorii the low-power, spectral irradiation reported previously. In particular, the following measurements should be noted:

1. The fast flux (>0.92 MeV) decreases sharply ($\sim$ 40%) from South (towards core center) to North! Only a 10% change was measured in core position E7.
2. The thermal flux is nearly isotropic, differing by less than 5% among the four corners of the capsule at each row.
3. The thermal-to-fast flux ratio changes from about 2.4 on the South side to about 4.0 on the North side, whereas the

low-power results gave a ratio of only 1.2! Neutronics calculations predict a ratio of 2.3 for the center of C7.

4. The total flux is about 50-60% lower than neutronics calculations, although the spectrum is reasonably similar.

These results have some serious implications for materials studies in the MFE 1 experiment. First of all, the steep fast flux gradient from South-to-North was not anticipated and was not seen in core position E7 or neutronics calculations. This gradient increases the uncertainty of damage calculations since the exact specimen location is now very important. The spectrum also appears to change with position and does not agree with our low-power spectral measurement. Since part of the spectrum (∿ 1-500 keV) cannot be easily measured on long irradiations, an additional uncertainty will be added to damage parameters. Reasons for these differences are now being explored and complete flux and damage maps will be available shortly.

Table I. FLUX MEASUREMENTS FOR ORR-MFE 1

Flux x 10^{14} n/cm^2 -s
Average Power Level = 22.5 MW
For fluence, multiply by 1.164 X 10^7 s
Core Location C7.

Energy Region	Core Position[a]				Neutronics[b] Calculation
	SW	SE	NE	NW	
Thermal	1.60	1.68	1.60	1.64	2.57
> .92 MeV	0.66	0.62	0.39	0.39	1.11
Total (estimated)					6.98

[a]SW stands for Southwest; the South side is closest to the center of the core.

[b]Values scaled to 22.5 MW from calculations by T. Gabriel (1979).

VII. FUTURE WORK

Analysis of the dosimetry results for ORR-MFE 1 will be completed during the next quarter. The foil measurements will be integrated with helium measurements now being done by H. Farrar IV (Rockwell International). Fluence and damage maps will be generated covering all experimental locations.

I. PROGRAM

Title: Helium Generation in Fusion Reactor Materials

Principal Investigators: D. W. Kneff, H. Farrar IV

Affiliation: Rockwell International, Energy Systems Group

II. OBJECTIVE

The objectives of this part of the fusion program at Rockwell International are to measure helium generation rates of materials for Magnetic Fusion Reactor applications in the Be(d,n) neutron environment, to characterize the Be(d,n) neutron fluence and neutron energy distributions as a function of position relative to the neutron source, and to develop helium accumulation fluence monitors for neutron fluence and energy spectrum dosimetry for the various fusion-program neutron test environments.

III. RELEVANT DAFS PROGRAM PLAN TASK/SUBTASK

SUBTASK II.A.2.1	Flux-Spectral Definition in the Be(d,n) Field
SUBTASK II.A.4.3	Be(d,n) Helium Gas Production Data
SUBTASK II.A.5.1	Helium Accumulation Monitor Development

IV. SUMMARY

Helium analyses have been completed for several additional Al, Fe, Ni, and Cu pure element helium accumulation dosimetry segments irradiated in a Be(d,n) neutron field. The results have been combined with earlier helium accumulation results to construct an initial high-energy (~6-32 MeV) neutron fluence map for the high-flux region of the Be(d,n) irradiation field.

V. ACCOMPLISHMENTS AND STATUS

Helium Accumulation Neutron Dosimetry for the Be(d,n) Irradiation Environment — D. W. Kneff, Harry Farrar IV, and M. M. Nakata (Rockwell International, Energy Systems Group)

Helium analyses have been completed for several additional Al, Fe, Ni, and Cu pure element helium accumulation dosimetry segments irradiated in a Be(d,n) neutron field. This irradiation, described in detail in previous reports,[1,2] was conducted with 30-MeV deuterons using the isochronous cyclotron at the University of California at Davis. This was a joint experiment with Argonne National Laboratory (ANL) and Lawrence Livermore Laboratory (LLL), with the objectives of measuring the spectrum-integrated helium generation cross sections of several materials, characterizing the Be(d,n) neutron environment, and developing the use of helium accumulation neutron dosimetry. The present report describes the use of the heliuiii dosimetry results to construct an initial fluence map of the high-flux region of the Be(d,n) neutron field.

The geometry of the inner (high-flux region) irradiation package included in the Be(d,n) irradiation is reproduced in Figure 1, to show the relative positions of the pure element dosimetry wire rings. These rings, oriented concentrically with the package axis, were sandwiched along with several other heliuni accumulation materials between stacks of radiometric dosiinetry foils. The average distances and neutron source angles of the dosimetry rings relative to the center of the beryllium target are given in Table 1.

Following the 93-hour irradiation, the rings were etched, to remove helium recoil effects, and each was typically segmented into 15-30 specimens for individual helium analysis. The analysis results for Al, Fe, Ni, and Cu are shown graphically in Figure 2, where the helium concentrations measured in the individual segments are plotted as a function of angular

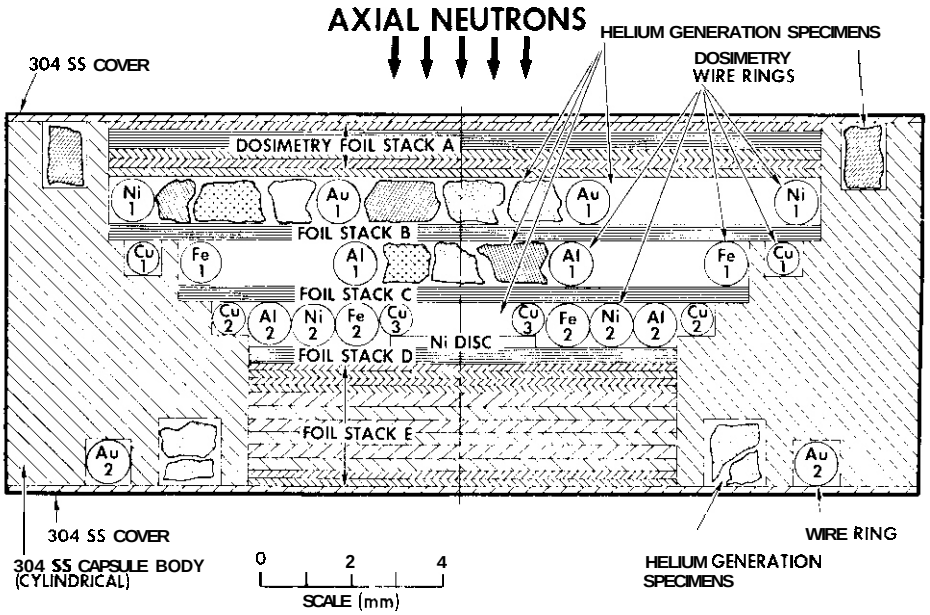

FIGURE 1. Cross Sectional View of the Be(d,n) Inner Irradiation Package.

TABLE 1

Be(d,n)-IRRADIATED HELIUM ACCUMULATION NEUTRON DOSIMETRY RINGS

Ring	Distance* (mm)	Angle*	Ring	Distance* (mm)	Angle*
Al-1	16.7	8.6:	Ni-1	16.9	26.3°
Al-2	18.4	13.6	Ni-2	18.2	10.3°
Fe-1	17.5	19.5°	Cu-1	17.9	23.6°
Fe-2	18.0	7.2°	cu-2	18.5	16.3°
			cu-3	17.8	4.2°

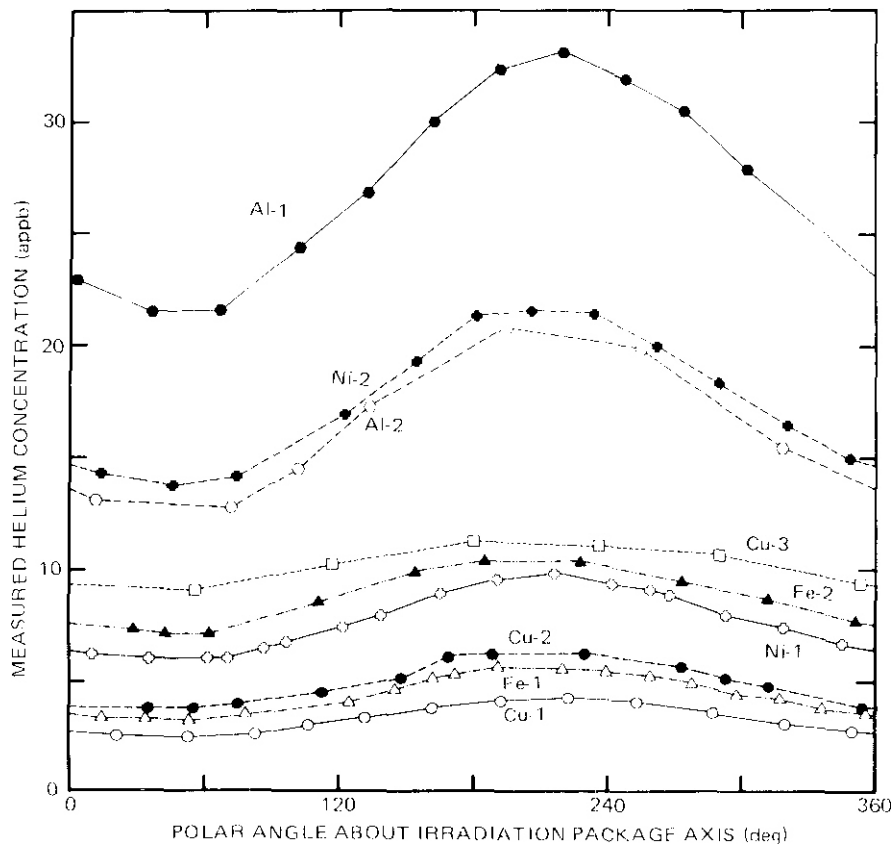

FIGURE 2. Measured Helium Concentrations in Be(d,n)-Irradiated Pure Element Ring Segments.

position about the irradiation package axis (polar angle in the plane of the ring). Examination of Figure 2 shows the same trend for all of the rings: a smooth variation in helium concentration approximating a single-cycle sine wave. The sinusoidal shape indicates that the package axis was slightly offset froiii the neutron source axis, and the amplitude provides a measure of that offset. The smoothness of the curves indicates that the deuteron beam was fairly uniform, as expected because of the ~±0.5-mm beam rastering in both the horizontal and vertical directions. The fact that the curves for different rings of the same element had different ranges of heliuiii concentrations is due to the different positions of the rings relative to the neutron source.

The initial neutron fluence map reported here was based on a comparison of these helium accumulation results with an initial model of the three-dimensional fluence profile, where the helium results were used to modify the model. This technique is similar to that used for RTNS-I, where an initial fluence profile was generated using radiometric foil dosimetry.[3] Note that a more detailed characterization of the Be(d,n) neutron environment will be made later, in a joint effort with ANL and LLL, by folding together all the radiometric and helium accumulation results to obtain detailed neutron fluence and energy spectrum profiles.

In the present case, detailed mapping of the radiometric data has not yet been performed. Instead, an initial fluence profile was derived from a least-squares cubic fit to the time-of-flight data of Meulders, *et al.*[4] This gave an empirical expression for the neutron fluence angular distribution (neutron source angle with respect to the deuteron beam axis). This expression was multiplied by a linear function approximating the variation in neutron fluence with distance from the beryllium target, to produce a three-dimensional model. The linear function was obtained from an approximate fit to the ANL counting results[5] for those radiometric foil segments from foil stacks A-E, Figure 1, irradiated along the package axis. The initial fluence profile model was thus:

$$\Phi = (C_o + C_1\xi + C_2\xi^2 + C_3\xi^3)(K_1 + K_2 d), \qquad (1)$$

where Φ is the total neutron fluence, ξ is the neutron source angle (in degrees), d is the distance from the center of the beryllium target, and C_i and K_i are constants.

To compare the helium accumulation data with this model, it was first noted that all of the curves in Figure 2 have similar shapes. This indicates that the Al, Fe, Ni, and Cu(n,total helium) cross sections, when integrated over the forward-direction Be(d,n) neutron spectra, have similar energy responses. These integrated responses also appear to be

roughly constarit as a .function of energy, as supported by the limited cross section information available.[6] For the preliminary data analysis discussed here. therefore, these four dosimetry materials were assumed to provide an approximately energy-insensitive measure of the total neutron fluence ≥6 MeV. Then comparing the data with the model, the axis of the irradiation package was deterinined to be offset froiii the neutron source axis by 1.03 mm in the horizontal direction, and 0.74 mm in the vertical direction. In addition, the initial assumed angular fluence dependence was found to be too steep. This was expected, since the model assumed a point neutron source, whereas the irradiation employed a rastered deuteroi beam, producing a ~6-mm-diameter neutron source spot ~13 mm from the front face of the irradiation package. To take this into consideration, the iiiodel was adjusted empirically for the angular gradient by replaciny the angle ~ by an effective angle f~, where f (= 1.045) is a constant.

The measured helium concentrations were then normalired to the fluences calculated using this adjusted fluence model, including offset corrections, arid the results are shown in Figure 3. Ideally, these curves should be flat. The structure remaining after these adjustments were made is attributed to a combination of the noncircular deuteron beam shape, slight curvature variations in the dosimetry wire rings, and variations in energy dependence in the helium-generation cross sections. For example, all of the curves in Figure 3 have similar slight structure, with dips at -60° and $\sim 230^{\circ}$. This suggests that the deuteron beam rastering, which presumably produced a noncircular neutron source profile (not yet folded into the map), did not have quite the same sweep in the horizontal and vertical directions. The overlap of the normalized heliuni concentrations for the multiple rings of each element support:; the assumption that the energy responses of the four dosimetry materials are similar over the neutron source angles covered (-4°-26°). Any energy sensitivity cannot be evaluated now, as there is presently insufficient information to unfold it from target solid angle effects. However, it is small over the source

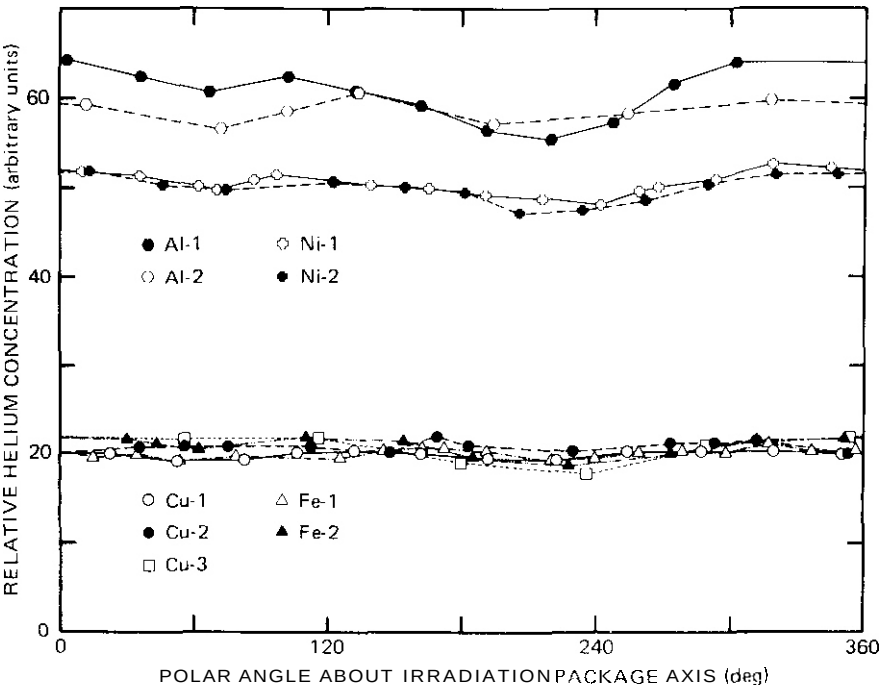

FIGURE 3. Ring Segment Helium Concentrations Normalized to Initial Be(d,n) Fluence Map.

angles measured, based on the small angular adjustment made to the initial fluence model.

The small scatter of the data about the curves in Figures 2 and 3 gives an estimated upper limit to the uncertainties in the individual helium analyses of about ±2%. This is approximately what would be expected from an analysis of the individual uncertainties of the helium measurement technique.

This initial mapping effort demonstrates that a significant amount of information can be obtained from a simple analysis of helium accumulation dosimeters, and that the neutron fluence is a very sensitive function of position. This is shown graphically in Figure 4, where the contours of constant fluence generated from the map are shown for the central plane of the first layer of helium-generation materials. The fluence varies by a factor of 8 over this 2-cm^2 irradiation area. The large fluence gradients

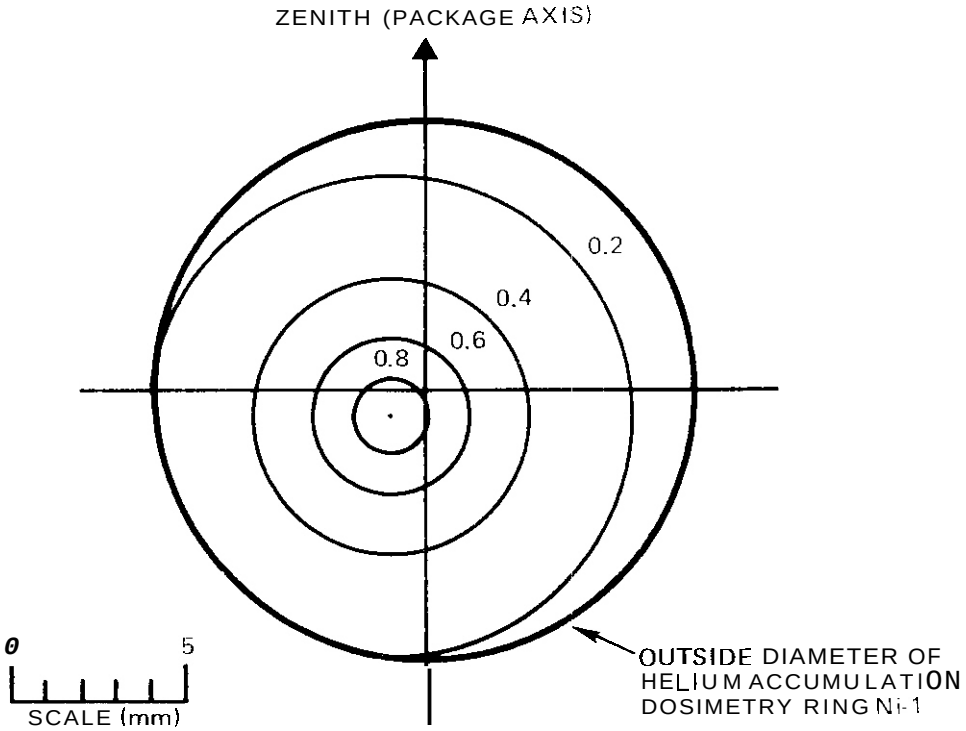

FIGURE 4. Contours of Constant Fluence for Midplane of Top Helium-Generation Specimen Layer in Be(d,n)-Irradiated Inner Package (Units are Fractional Fluence Values Relative to Midplane Fluence Maximum).

are also clearly shown by the large heliuni concentration variations produced in each dosinietry ring by the small, 1.3-mm package offset from the beam axis. This offset produced approximately a factor of 2 variation in fluence around the periphery of the irradiation region depicted in Figure 4. This demonstrates the importance of including passive dosimetry in Be(d,n) and Li(d,n) irradiations requiring accurate irradiation information.

The results of this fluence map were used to recalculate the relative total heliuni generation cross sections of the four dosimetry materials used here. The results, given in Table 2, are the same as the more preliminary values previously reported for these four elements.[7] Coinparison with the T(d,n) results measured in RTNS-I for ~14.8-MeV neutrons,[8]

TABLE 2

APPROXIMATE RELATIVE HELIUM-GENERATION RATES OF PURE ELEMENTS

Element	Helium-Generation Rates Relative to Copper	
	Be(d,n) 30-MeV Deuterons	T(d,n) RTNS-I
cu	1	1
Al	2.9	2.80
Fe	1.0	0.94
Ni	2.4	1.92

also listed in Table 2, shows that the relative total helium-generation cross sections for the two irradiation environments are similar. This further supports the conclusion that the energy sensitivity of these dosimeters is small over the neutron source angles investigated.

In summary, the results to date from this Be(d,n) irradiation indicate that the four analyzed helium accumulation dosimetry inaterials (Al, Fe, Ni, and Cu) have similar but slowly varying energy responses over the neutron source angles investigated ($\sim 4^{o}$-26°). Any one of these inaterials can thus be used to map out the high-energy neutron fluence profile in detail. These materials effectively provide one detector response for combining with radiometric dosimetry to unfold the neutron energy spectra. Other materials are presently being examined for different energy responses. These include, for example, heavier elements (such as gold) that were also irradiated in the Be(d,n) experiment. Several other materials with varying low-energy (—0-6 MeV) neutron responses are now being tested in other neutron environments, including fission reactors.

VI. REFERENCES

1. D. W. Kneff and H. Farrar IV, Helium Generation in Fusion Reactor Materials, Technical Progress Report for Period April-September 1977, AI-DOE-13219, Atomics International, Canoga Park, CA, January 1978.

2. D. W. Kneff, H. Farrar IV, and M. M. Nakata, "Helium Generation in Fusion Reactor Materials," in Damage Analysis and Fundamental Studies, Quarterly Progress Report, DOE/ET-0065/2,3, and 4, U.S. Department of Energy, Mdy 1979.

3. H. Farrar IV, D. W. Kneff, R. A. Britten, and R. R. Heinrich, "Fluence Mapping of RTNS-I by Helium Accumulation and Foil Activation Methods," Proc. Symp. on Neutron Cross-Sections from 10 to 40 MeV, M. R. Bhat and S. Pearlsiein, eds., BNL-NCS-50621, pp. 175-184, Brookhaven National Laboratory, NY, July 1977.

4. J. P. Meulders, P. Leleux, P. C. Macq, and C. Pirart, "Fast Neutron Yields and Spectra from Targets of Varying Atomic Number Bombarded with Deuterons from 16 to 50 MeV," Phys. Med. Biol. 20, 235 (1975).

5. L. R. Greenwood. "Experiments at tne U.C. Davis Cyclotron, Be(d,n), E_d = 30-40 MeV," in Damage Analysis and Fundamental Studies, Quarterly Progress Raport October-December 1978, DOE/ET-0065/4, U.S. Department of Energy, May 1973.

6. See, fot- example, D. I. Gat-ber and R. R. Kinsey, Neutron Cross Sections, Volume II, Curves," 5NL 325, Third Edition, National Neutron Cross Section Center, Brookhaven National Laboratory, January 1976.

7. D. W. Kneff, H. Farrar IV, and M. M. Nakata, "Helium Generation in Fusion Reactor Materials," in Damage Analysis and Fundamental Studies, Quarterly Progress Report January-March 1979, DOE/ET-0065/5, U.S. Department of Energy, May 1979.

8. H. Farrar IV and D. W. Kneff, "Helium Generation in Twelve Pure Elements by 14.8-MeV Neutrons," Trans. Am. Nucl. Soc. 28, 197 (1978).

VII. FUTURE WORK

Helium analyses of the Be(d,n)-irradiated pure elements will continue. Other heliuiii accumulation dosiiiietry materials, such as gold, will be investigated in detail for different neutron energy sensitivities. The helium accumulation results will be combined with ANL and LLL radiometric counting results to produce a more detailed characterization of the Be(d,n) neutron field.

VIII. PUBLICATIONS

A paper entitled "Helium Accumulation Neutron Dosimetry for Fusion Program Be(d,n) and Li(d,n) Neutron Test Environments" was prepared for presentation at the Third ASTM-EURATOM Symposium on Reactor Dosimetry, Ispra, Italy, on October 1, 1979.

I. PROGRAM

Title: Irradiation Effects Analysis (WH011/EDA)
Principal Investigator: D. G. Doran
Affiliation: Hanford Engineering Development Laboratory

II OBJECTIVE

The objective of this work is to predict the spatial variations of radiation daiiiage parameters within the test volume of the Fusion Materials Irradiation Test (FMIT) facility, and the sensitivity of these parameters to cross section and spectrum uncertainties.

III. RELEVANT DAFS PROGRAM PLAN TASK/SUBTASK

SUBTASK II.A.2.4 Flux Spectrum Definition in FMIT
II.B.l .5 Calculation of Displacement Cross Sections

IV. SUMMARY

Interest in the possibilities of tailoring neutron spectra in the high flux (greater than 10^{14} n/cm^{2}s) volume of the FMIT test cell led to the calculations summarized in this report. These calculations show that hemispherical reflectors can increase the high flux volume by as much as a factor of two (from S.6 cm^3 to 11.2 cm^3). however, this increase is purchased at the cost of essentially all remaining, useful, test cell irradiation space. For the reflectors considered, increases in damage rates tend to be small (generally less than several percent).

V. ACCOMPLISHMENTS AND STATUS

A. FMIT Damage Parameter Sensitivity Study -- J. 0. Schiffgens and L. L. Carter (HEDL)

1. Introduction

High energy (35 MeV) deuterons in FMIT produce neutron spectra with large components of high energy (>14 MeV) neutrons.[1,2] Monte Carlo calculations have recently been made to determine the feasibility of significantly altering FMIT neutron spectra and associated damage parameters at test cell locations where the pristine flux is greater than 10^{15} n/cm^{2}s, and at the same time increase the high flux irradiation volume. For these calculations, hemispherical shells of various materials were assumed to be centered at the intersection of the beam with the lithium (source) backing plate. Beryllium, stainless steel, tungsten, and uranium (natural and 235) shells with inner radii (I) of 2.54 and 5.08 cm and outer radii (0) of 10.16, 15.24, and 22.86 cm were considered. The parameters calculated in this study were the volume within which the flux is greater than 10^{15} n/cm^{2}s (V_ϕ), the flux (ϕ), and the displacement and helium production rates at various locations within V_ϕ.

2. Results

The calculations showed that the volume V_ϕ increased from 5.6 cm^3 (the pristine volume) to 6.3 cm^3 (+13%), 6.7 cm^3 (+20%), 7.1 cm^3 (+27%), 7.6 cm^3 (+37%), and 10.7 cm^3 (+93%) when it was enclosed in stainless steel, beryllium, tungsten, natural uranium and uranium -235 hemispherical reflectors, with I's of 5.08 cm and 0's *of* 15.24 cm (except U-235 where 0 is 10.16 cm), respectively. The corresponding peak fluxes ϕ_p increased from 2.42 x 10^{15} n/cm^{2}s (the pristine flux) to 2.46 x 10^{15} n/cm^{2}s (+1.5%), 2.48 x 10^{15} n/cm^{2}s (+2.2%), 2.49 x 10^{15} n/cm^{2}s (+2.8%), 2.52 x 10^{15} n/cm^{2}s (+3.8%), and 2.62 x 10^{15} n/cm^{2}s (+8.0%), respectively. It should be noted that large increases in V_ϕ are accompanied by only minor increases in the average flux within V_ϕ. Of the non-fissionable reflectors, a tungsten shell with an 1/0 of 2.54 cm/22.86 cm produced the largest increase in V_ϕ, from 5.6 cm^3 to 9.9 cm^3.

For shells with an 1/0 of 2.54 cm/10.16 cm, displacement and helium production rates in copper were calculated for tungsten and natural

uranium reflectors at two positions, as shown in Table 1. The maximum increase in flux it positions 1 and 2 was 8 and 31 percent, respectively, and was essentially all in the 0 to 5 MeV range. Corresponding maximum increases in helium production rates of 2.5 and 2.3 percent were obtained, together with maximum increases in displacement rate of 2.3 and 8.5 percent.

	Pristine $V_{\cdot}$ = 5.6 cm^3		
.0	2.42 x 10^{15}	220	1890
1.64	1.03 x 10^{15}	106	1050
	Tungsten $V_{\cdot}$ = 9.7 cm^3 (+73%)		
.0	2.57 x 10^{15}	223	1940
1.64	1.28 x 10^{15}	112	1050
	Natural Uranium $V_{\cdot}$ = 11.2 cm^3 (+100%)		
.0	2.61 x 10^{15}	225	1890
1.64	1.35 x 10^{15}	115	1070

VI. REFERENCES

1. J. O. Schiffgens, R. L. Simons, F. M. Mann, and L. L. Carter. Damage Analysis and Fundamental Studies Quarterly Technical Progress Report, DOE/ET-0065/5, January-March 1979, p. 53; DOE/ET-0065/4, October-December 1978, p. 42.

2. J. O. Schiffgens, R. L. Simons, F. M. Mann, and L. L. Carter, "Spatial Variations of Damage Parameters in FMIT and Their Implications," Proceedings, First Topical Meeting on Fusion Reactor Materials, January 29-31, 1979, Miami Beach, Florida.

VII. FUTURE WORK

Spatial variations in PKA spectra will be analyzed and calculations to better define the effects of possible cross section uncertainties will be made.

VIII. PUBLICATIONS

None.

I. PROGRAM

Title: Damage Analysis and Dosimetry Radiation Damage Analysis
Principal Investigator: A. N. Goland
Affiliation: Brookhaven National Laboratory

II. OBJECTIVE

Radiation damage analysis studies associated with the use of electrical insulators in fusion reactors.

III. RELEVANT JAFS PROGRAMS PLAN TASK/SUBTASK

SUBTASK II.A.2.3 Flux Spectral Definition in FMIT

SUBTASK II.B.l Calculation of Displacement Cross Sections

IV. SUMMARY

The RSIC version of the MORSE neutron gamma-ray transport code has been converted for use on the MFECC 7600 and CRAY computers. Runs made at BNL and the MFECC using the 7600's yield identical results. Runs made at the MFECC using the CRAY and the 7600 yield neutron spectra that differ by 30%.

Evaluation of ionization assisted processes for producing displacements in insulators is in progress. The work is not yet complete and will be described in a future quarterly report.

V. ACCOMPLISHMENTS AND STATUS

A. Use of the Magnetic Fusion Energy Computer Center: A. N. Goland, H. C. Berry, G. F. Dell, O. W. Lazareth and A. B. Scott.

During the last quarter a major effort has been made to complete the transfer of neutron transport calculations to the computers at the Magnetic Fusion Energy Computer Center. This transfer has included the following steps:

1) adaptation of the RSIC version of MORSE to the MFECC 7600 computer,

2) adaptation of the RSIC version of MORSE to the CRAY computer,

3) alteration of MORSE-L, the Livermore version of MORSE, to incorporate the BNL neutron generator and uncollided flux estimator subroutines.

1. Adaptation of the RSIC version of MORSE to the MFECC 7600

The adaptation consisted of making the fortran consistent with the conventions used at the MFECC as well as resolving differences in the loaders, compilers, control language, and tape formats. The random number generator used on the MFECC 7600 was the same as the one used at BNL. Runs made using the RSIC version of MORSE at the MFECC and at BNL yielded identical results. All flux values and random number sequences were identical The computer time required to run the same job at both facilities was within 10% of being equal.

2. Adaptation of the RSIC version of MORSE to the CRAY

The random number generator used on the 7600 is written in machine language. This would not work on the CRAY. Instead a random number generator, RNFL, from the MFECC was used.

A comparison was made between the MFECC 7600 and the CRAY for a coupled $n+\gamma$ transport problem having FMIT geometry. Several items were noticed:

a. It was determined that the MFECC random number generator, RNFL, works differently on the CRAY than it does on the 7600. A different random number generator that gives the same sequences on the CRAY and the 7600 has been developed at the MFECC. This generator will be used in MORSE in the future.

b. Comoarisons of neutron and gamma-ray spectra obtained with the 7600 and the CRAY are shown in Figures 1 and 2. Neutrons produced by 35 MeV deuterons incident upon a 2 cm thick lithium target were transported through a sample assembly approximated by a $30 \times 20 \times 20$ cm^3 block of iron having an average density of 1.925 g/cm^3. Except at the highest and lowest energies the neutron spectrum obtained with the CRAY is consistently 30% higher than that obtained using the 7600. Within the uncertainties of the calculations the gamma-ray spectra overlap. At present the only known difference in the two calculations is the different behavior of the random number generator on the two computers.

3. Alteration of MORSE-L

The source version of MORSE-L has been made available for general access. The 6NL neutron generator source subroutine as well as the estimator for the uncollided flux have been incorporated into it. MORSE-L is so large that overlays must be used to load it onto the 7600. This has been done, and the program is currently being debugged. The availability of both MORSE-L and the RSIC version of MORSE will provide a consistency check for our calculations.

B. Damage Analysis

Damage produced in multicomponent materials by recoil atoms and by energetic electrons resulting from gamma ray interactions have been reported previously.[1,2] For materials lighter than copper less than 50%

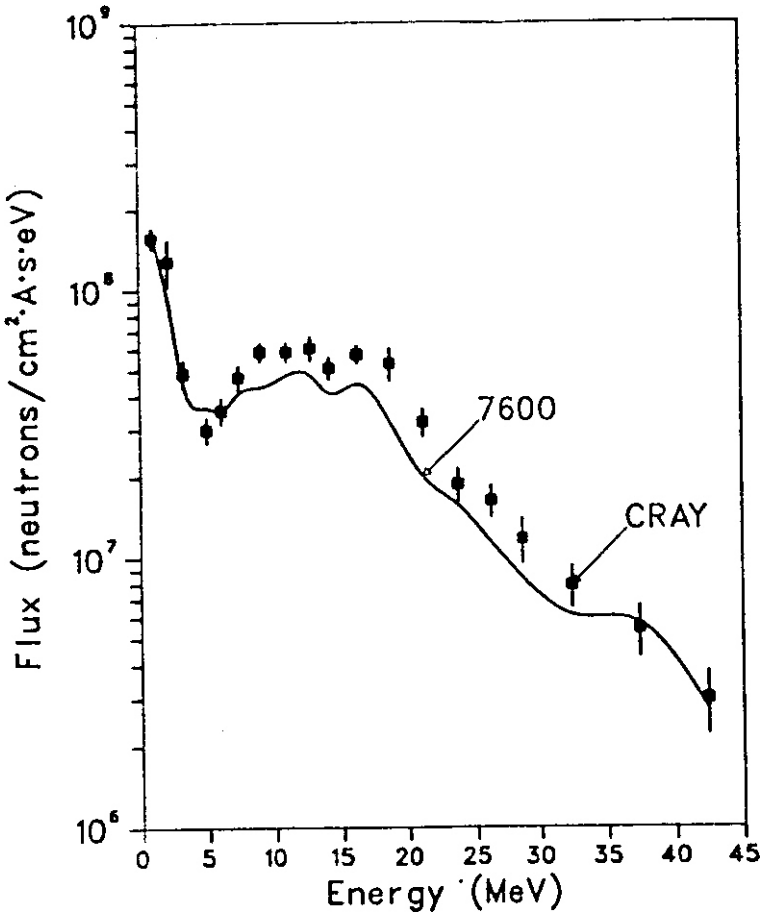

Figure 1. Neutron spectra generated by the RSIC version of MORSE on the MFECC 7600 and CRAY computers. Problem parameters: $30 \times 20 \times 20$ cm^3 Fe block, density = 1.925 g/cm^3, detector depth = 12 cm.

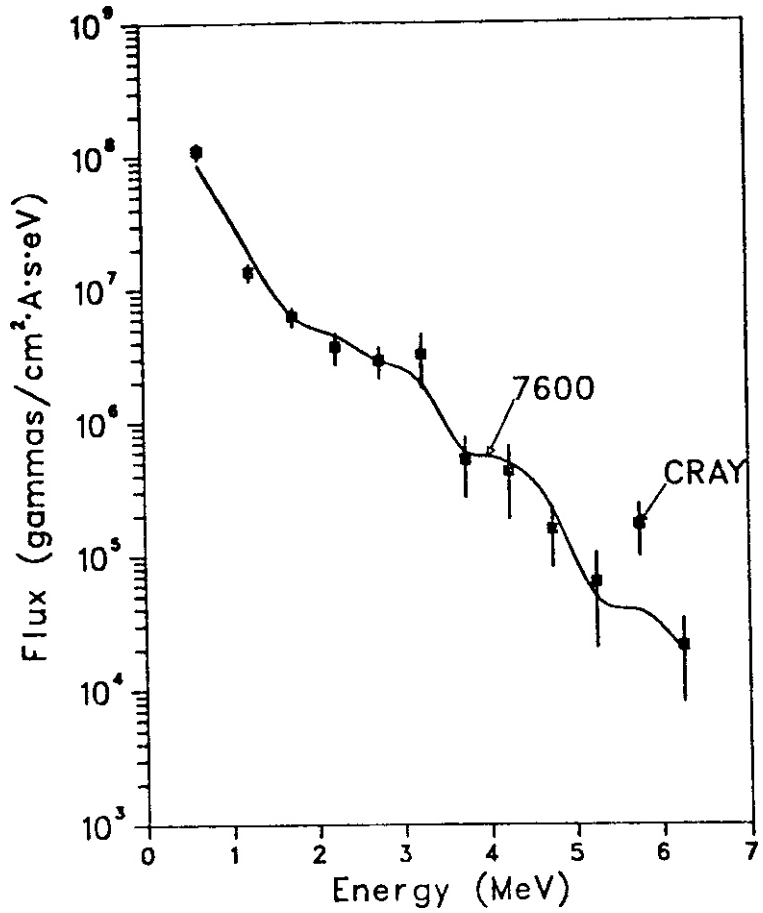

Figure 2. Gamma-ray spectra generated by the RSIC version of MORSE on the MFECC 7600 and CRAY computers. Problem parameters: $30 \times 20 \times 20$ cm^3 Fe block, density = 1.925 g/cm^3, detector depth = 12 cm.

of the primary knock-on atom energy is dissipated in producing displacements. The balance of the energy might be dissipated by processes that produce displacements through other mechanisms. Currently the magnitude of ionization assisted displacement processes is being evaluated.[3] This work is not yet complete and will be presented in a future quarterly report.

VI. REFERENCE';

1. A. N. Goland, H. C. Berry, G. F. Dell and 0. W. Larareth, Damage Analysis and Fundamental Studies Quarterly Technical Progress Report, Jan-Mar 1979, p. 43, DOE/ET-0065/5.

2. A. N. Goland, H. C. Berry, G. F. Dell and O. W. Lazareth, Damage Analysis and Fundamental" Studies Quarterly Technical Progress Report, April-June 1979, in print, DOE/ET-0065/6.

3. B. S. Yarlagadda and J. E. Robinson, J. Nuc. Mat. 63, 466 (1976).

I. PROGRAM

Title: Dosimetry and Damage Analysis
Principal Investigator: L. R. Greenwood
Affi1iation: Argonne National Laboratory

II. OBJECTIVE

To improve neutron spectra measurement techniques and to determine flux-spectra errors and uncertainties in calculated damage parameters.

III. RELEVANT DAFS PROGRAM TASK/SUBTASK

Task 11. A.3 Sensitivity Studies
Improved dosimetry techniques also relevant to:
Task II. A.l Fission Reactor Dosimetry
Task II. A.2 High-Energy Neutron Dosimetry

IV. SUMMARY

Neutron flux and cross-section error and covariance files have been developed for routine dosimetric applications of the STAYSL code. A complete description of the input data files is given along with some applications of STAYSL. A paper has been prepared for presentation at the Third ASTM-EURATOM Symposium on Reactor Dosimetry at Ispra, Italy, in October 1979.

V. ACCOMPLISHMENTS AND STATUS

A. Development of the STAYSL Computer Code - -
L. R. Greenwood (ANL)

In the last quarterly report (DOE/ET-0065/6) we reported that the STAYSL! code written by F. G. Perey (ORNL) was now operational at Argonne, hut without the use of covariance effects. We have now developed procedures for adding covariance errors for routine dosimetric applications. In order to take advantage of our previously developed cross-section:' and associated error files, as well as cadmium cover and neutron self-shielding programs, the input to STAYSL has been modified to be compatible with our Monte Carlo code SANDANL.[3]

There are three types of uncertainty in the input data used for flux-spectral analysis, namely, activation errors, nuclear cross-section errors, and input flux errors. In addition to this, covariance errors must be specified for all related parameters. The STAYSL code then uses a least-squares technique to find the minimum value of ;? for the output flux-spectrum which best fits the input data. At present, only activation errors can he treated rigorously. Errors due to counting uncertainties, detector calibration, and nuclear data are typically less than 2% and covariance effects are negligible.

Nuclear cross-section errors and covariances can in principle he deduced from the available experimental data and such files will be published in ENDF/B-V. In the meantime, we will continue to use our cross-section error files derived from W. N. McElroy et al,[4] extended to 44 MeV as required for high energy dosimetry. Table I compares our cross-section error estimates with the results of integral testing in Be(d,n) fields. As can be seen, our error estimates tend to be conservatively large.

Input flux errors are unfortunately the most difficult to define. For example, the reactor neutronics calculations used as input generally have no error estimates available. Consequently, we have somewhat arbitrarily assigned flux errors on the basis of integral data testing and our past experience. Sensitivity studies have been done to assess

Table I. Comparison of Estimated Cross Section Errors with Integral Test Results for Be(d,n), E_d = 14 - 40 MeV. The 90% energy sensitivity limits are given.

Reaction	Energy Range (MeV)	Estimated Range of Errors (±%)	Measured Integral Errors (±%)
$^{115}In(n,n')^{115m}In$	2 - 23	8 - 20	3
$^{238}U(n,f)$	2 - 30	6 - 15	4
$Ti(n,p)^{46}Sc$	5 - 33	15 - 50	14
$Ti(n,p)^{47}Sc$	3 - 33	15 - 50	15
$^{48}Ti(n,p)^{48}Sc$	7 - 27	15 - 50	7
$Fe(n,p)^{54}Mn$	4 - 33	10 - 40	6
$^{56}Fe(n,p)^{56}Mn$	6 - 23	10 - 30	4
$^{59}Co(n,p)^{59}Fe$	5 - 24	10 - 40	8
$^{58}Ni(n,p)^{58}Co$	4 - 23	6 - 30	9
$^{60}Ni(n,p)^{60}Co$	6 - 23	10 - 40	14
$^{27}Al(n,\alpha)^{24}Na$	7 - 21	6 - 15	3
$^{54}Fe(n,\alpha)^{51}Cr$	6 - 28	15 - 40	36
$^{59}Co(n,\alpha)^{56}Mn$	7 - 24	10 - 40	4
$^{45}Sc(n,2n)^{44m}Sc$	13 - 27	10 - 20	14
$^{58}Ni(n,2n)^{57}Ni$	13 - 28	20 - 30	14
$^{59}Co(n,2n)^{58}Co$	12 - 27	10 - 20	9
$^{59}Co(n,3n)^{57}Co$	22 - 36	20 - 40	28
$Zr(n,2n)^{89}Zr$	13 - 28	15 - 30	13
$^{93}Nb(n,2n)^{92m}Nb$	10 - 22	10 - 20	7
$^{169}Tm(n,2n)^{168}Tm$	10 - 23	10 - 20	7
$^{169}Tm(n,3n)^{167}Tm$	18 - 30	10 - 30	9
$^{197}Au(n,2n)^{196}Au$	9 - 24	10 - 20	9
$^{197}Au(n,3n)^{195}Au$	18 - 29	10 - 30	6
$^{197}Au(n,4n)^{194}Au$	27 - 40	15 - 30	11
$^{238}U(n,2n)^{237}U$	7 - 16	20 - 40	11

the importance of these error assignment:. In regions *of* good, overlapping foil coverage, increasing the input. flux errors will only increase the output flux errors up to a point where no further effect is seen. This procedure can be used to determine maximum error limits if no other guidance is available. However, in regions of poor foil coverage, this procedure will fail and one must rely on past experience.

Flux and cross-section self-covariances have been estimated using a Gaussian function with a full width of several energy groups. In other words, we are saying that nearby groups must he very strongly correlated; however, widely spaced groups are almost entirely independent. This statement is analogous to smoothing the iteration in SAND II and also avoids the problem of discontinuities in the output flux spectrum, especially at sharp resonances in the cross-section, which are not physical. Covariances between different cross-sections must be determined from experimental data and we must wait for their publication in ENDF/B-V.

So far, our experience with STAYSL is generally similar to the results obtained with SANDANL. In both cases, the input flux uncertainties strongly dominate the output flux uncertainties. The STAYSL code treats input flux errors more realistically since our perturbation procedures in SANDANL produce non-physical, long-term correlations. Output flux errors thus appear to be more physically reasonable in STAYSL.

Figure 1 shows a flux spectrum determined at the Oak Ridge Research Reactor (ORR) at a reduced power of 1 MW. This may be compared with the results of SANDANL published in the previous report (DOE/ET-0065/6). Both show large errors in the 1-500 keV region where foil coverage is always very poor in a mixed-spectrum reactor. The output flux covariance file from STAYSL has also been interfaced with our damage parameter codes and Table II lists calculated damage rates and errors for the ORR spectrum shown in Fig. 1.

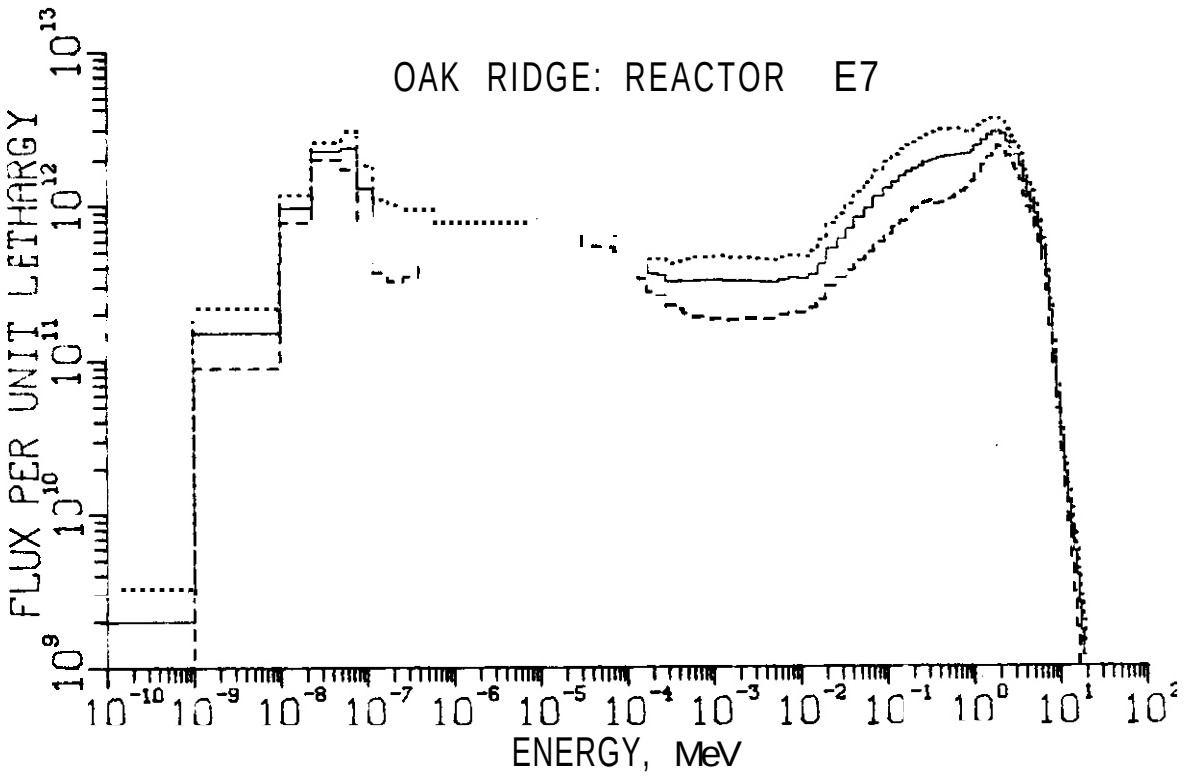

Fig. 1. STAYSL results for the Oak Ridge Research Reactor. Twenty-one reactions were measured in core location E7 at a reduced power of 1 MW. Differential flux times neutron energy is plotted. The dashed lines represent one standard deviation errors.

Table 11. Damage Parameters for ORR Calculated with STAYSL Flux Covariances. The spectrum is shown in Fig. 1, although the power is renormalized to 30 MW.

Material	Damage (DPA/yr)	Helium (ppm/yr)
Ni	5.7 ± 0.6	22.6 ± 2.5[a]
Cu	5.5 ± 0.6	1.4 ± 0.2
Nb	5.4 ± 0.6	0.31 ± 0.04
Au	4.4 ± 0.4	0.0030 ± 0.0005

[a] $^{58}Ni(n,\gamma)^{59}Ni(n,\alpha)$ process not included.

VI. REFERENCES

1. F. G. Perey, Least-Squares Dosimetry Unfolding: The Program STAYSL, ORYL-TM-6062 (1977).
2. L. R. Greenwood, Extrapolated Neutron Activiation Cross-Sections for Dosimetry to 44 MeV, ANL-TM-115 (1978).
3. G. R. Odette, Trans. Am. Nucl. Soc. 22, 803 (1975); revised by L. R. Greenwood.
4. W. N. McElroy and L. S. Kellogg, Nucl. Technol. 25, 180 (1975).

VII. FUTURE WORK

We intend to use the STAYSL code for most routine dosimetry performed for the fusion program. As new cross-section variance-covariance files are published in ENDF/B-V, they will be incorporated into the code.

VIII. PUBLICATIONS

1. L. R. Greenwood, Uncertainties and Covariances of Spectra Derived from Integral Measurements, Proceedings of the Third ASTM-EURATOM Symposium on Reactor Dosimetry, Ispra, Italy, Oct. 1-5, 1979.

CHAPTER 3

SUBTASK B: DAMAGE PRODUCTION

I. PROGRAM

Title: 14 MeV Neutron Irradiations (WZJ-14)
Principal Investigator: M. Guinan/W. Barmore
Affiliation: Lawrence Livermore Laboratory

II. OBJECTIVE

The objective of this work is the characterization of the primary damage state resultiny from 14 MeV neutron irradiations and the determination of the influence of neutron spectral effects on defect production and distribution.

III. RELEVANT DAFS PROGRAM TASK/SUBTASK

SUBTASK	II.B.2.3	Cascade Production Methodology
	II.B.3.2	Studies of Metals
	II.C.6.3	Microstructure Correlations
	II.C.11.4	Creep Under High-Energy Neutron Irradiations

IV. SUMMARY

A. The results of fully dynamic computer simulations of collision cascades in tungsten show an abrupt decrease in defect production efficiency beginning at energies about 10 times the minimum threshold energy. A detailed analysis of the time development of a typical cascade reveals that this drop in efficiency is primarily due to recombination by defect transport during the cascade cooling phase. This transport is an order of magnitude larger than that predicted from equilibrium transport theory.

B. In-Situ creep studies on niobium at 550°C have recently been completed at RTNS-II. Preliminary analysis of the data indicate that it should possible to extract steady state defect concentrations under irradiation as well as provide information on the thermal stability of glide plane barriers produced by the irradiation.

V. ACCOMPLISHMENTS AND STATUS

A. The Time Dependence of Defect Configurations in a Collision Cascade - R.W. Guinan, J. H. Kinney and R. N. Stuart (LLL)

1. Introduction

Both experiments and fully dynamic computer simulations[1] reveal a marked decrease in defect production efficiency at PKO energies of a few keV, whereas binary-collision calculations[2] do not. However, when fully dynamic calculations are terminated at the end of the displacement process, both the number and separation of Frenkel pairs can be in good agreement with the results of binary calculations[3] when the same interatomic potential is used. An additional comparison for 2.5 keV cascades is given in Table 1. The results of the binary calculations of Beeler and Besco[4] are compared to two sets of dynamic calculations, one using the Beeler-Besco potential (II) and the other a potential (I) developed by Wilson and Bisson of Sandia Laboratories, Livermore.

TABLE 1

Comparison of Fully Dynamic and Binary Calculations for 2.5 keV Cascades in Tungsten

	Dynamic Models		Binary Collision
Cascade Volume	540	600	670
Initial Displacements	25	29	25
After Recombination	9	12	13
After Cascade Cooling	3.3	5.8	--

The dynamic result using the same potential is in good agreement with the binary calculation with respect to cascade size and initial displacements. When unstable pairs are eliminated using the appropriate recombination volume[5], agreement is maintained, indicatiny that the defect distributions are similiar. If the dynamic calculations are run long enough to allow the cascades to cool, as Table 1 shows, a substantial fraction of the defects recombine.

The simplest model we might consider to account for the additional recombination would involve the use of a larger effective recombination volume. The results of binary calculations[6] covering a wide energy range as well as the present results show that the fractional decrease obtained by increasing the volume is nearly independent of the cascade energy. On the other hand, the dynamic results after cascade cooling show a pronounced energy dependence in the low kilovolt range. Thus, a model must be developed which reproduces the observed energy dependence.

2. Time Dependence

The development of an energetic cascade can be roughly divided into three phases:

I. A collision phase, lasting a few tenths of a picosecond, during which the PKO energy is shared among successive generations of recoil atoms until none of the recoils has enough energy to leave its lattice site.

II. A relaxation phase lasting the order of half a picosecond (a few lattice vibration periods) during which defects begin to assume their equilibrium configurations, the closest unstable pairs collapse, and more isolated defects develop their surrounding strain fields.

III. A cooling phase of the order of picoseconds during which the cascade region reaches local thermal equilibrium with its surroundings.

The three phases are delineated in Figure 1, where the number of displaced atoms in both a 600 eV and a 2.5 keV cascade are plotted as a function of time. The number of displaced atoms reaches a maximum shortly before the erid of phase I and decreases rapidly during the [illegible] of phase II. Since the recombination of a close pair begins as soon as the interstitial has stopped, phase II starts well before the end of phase I. A large fraction of the defects remaining at the end of phase II recombine during phase III as a result of the substantial defect migration occurring [illegible]

This is illustrated in Figures 2.(a) and 2.(b) for interstitials and vacancies respectively. In each figure the observed defect jump rate is plotted as a function of time for the 2.5 keV cascade used in Fig. 1. Recombination jumps were riot included in determining the jump rates for either defect.. Relatively high jump rates are still observed well into phase III where the cascade region has cooled considerably.

To put these observations in perspective, we tiave calculated the jump rdtes expected from equilibrium thermodynamics using meas.r-jump rates for tnis potential[7,8] and an effective temperature based on the total energy in the cascade volume. These rates are shown as the dashed lines which begin at. the end of phase I. While the assumption of local equilibrium is a very poor one duriny phase II, it is not unreasonable most of phase III where the jump rates are more than an order of magnitude greater than expected.

3. Discussion

It seems clear that the reduction in defect production efficiency calculated in the low kilovolt range is the result of defect migration. The cause of the high migration rates is not yet clear. Although there are several possible explanations, including the persistance of 'hot' spots or jumps induced by nearby recombinations, the answer will require detailed studies of several more cascades to accumulate enough statistics to evaluate the various possibilities.

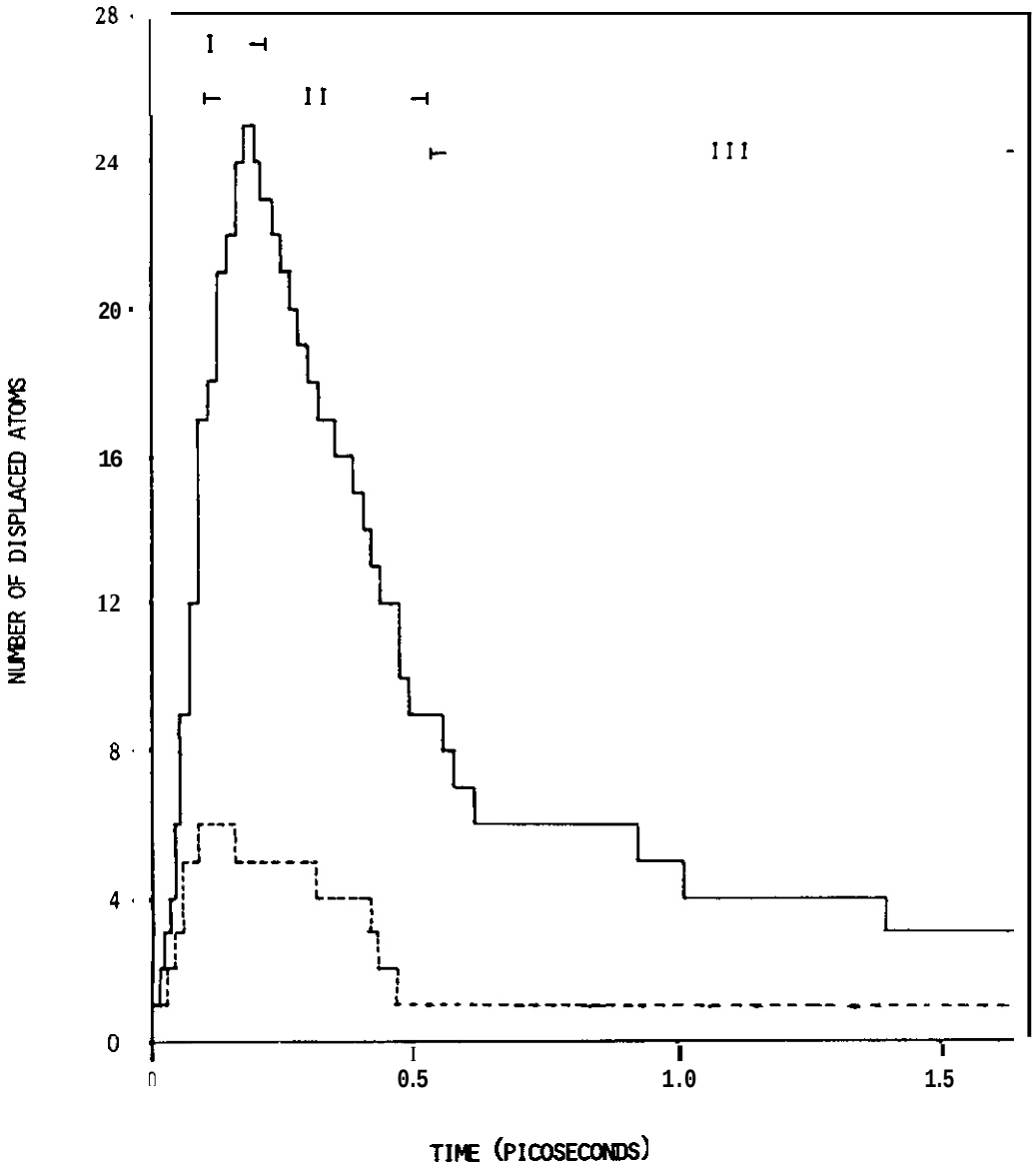

FIGURE 1. The time development of two collision cascades. The number of displaced atoms is given as a function of time for a 600 eV (---) and a 2.5 keV (—) collision cascade.

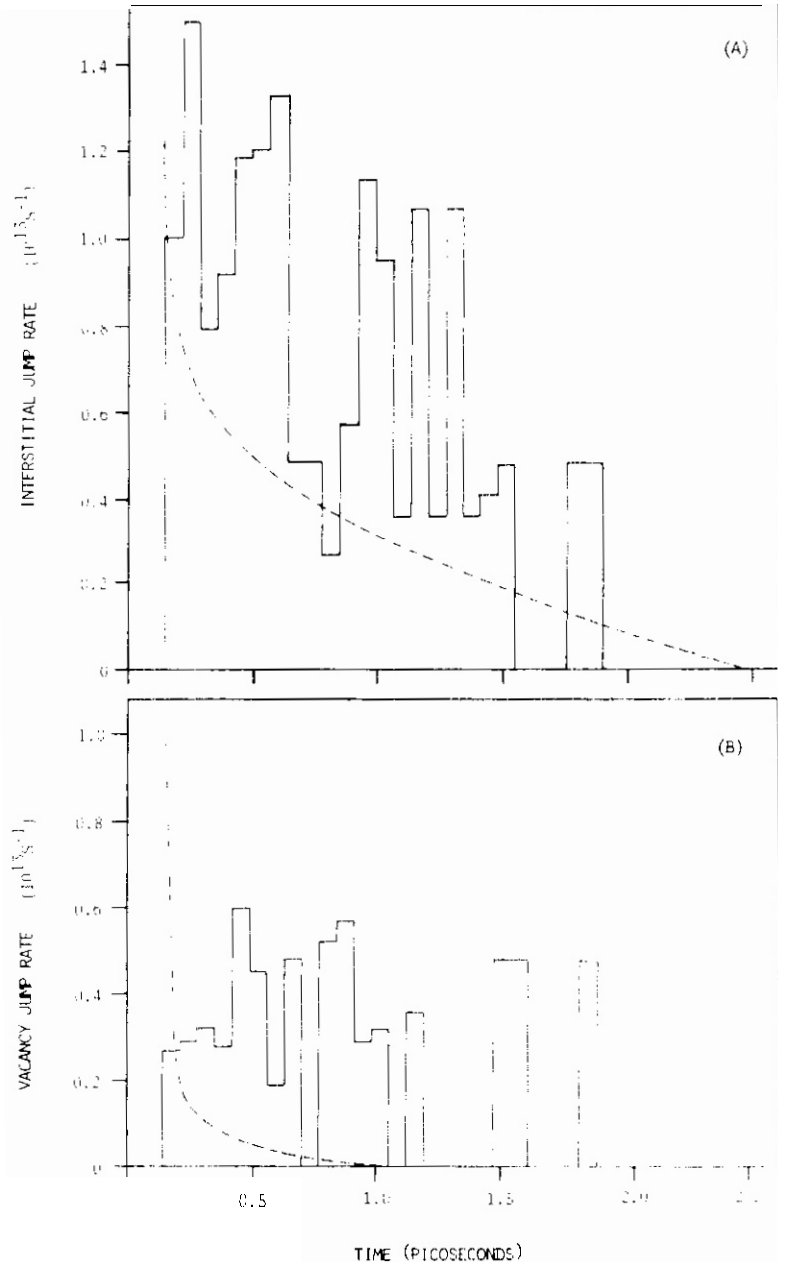

FIGUKC 2. Defect jump rates duriny the development of a 2.5 keV collis cascade. (a) Interstitial jump rate vs time. (b) Vacancy rate vs time. The dashed line in each figure is the expecte jump rate assuming thermal equilibrium.

B. In-Situ Creep Testing During Irradiation With High-Energy Neutrons - W. L. Barmore, A. W. Ruotola and E. L. Raymond (LLL)

1. Introduction

In experiments last year, significant changes in the creep behavior of niobium in the temperature range 450 to 600°C were produced by irradiation with high-energy neutrons.9 The in-situ creep experiments were conducted at the Be(d,n) source at the University of California at Davis, using 35 MeV deuterons. The neutron flux was 2×10^{16} $n/m^2 \cdot s$ ($E > 1$ MeV) with a high component of neutrons with energies greater than 4 MeV.

In this exploratory study, two types of radiation-induced effects on the creep behavior of niobium were observed. One effect was short-term, began with the onset of irradiation, and was observable for about one minute. The second effect was longer term and progressive.

After establishing a steady-state thermal creep rate at 600°C the beam was instantaneously turned on. There was an immediate increase in creep rate, followed by a continuous, long-term decrease in creep rate. When the beam was turned off, there was an immediate decrease in creep rate followed by a continuous, long-term increase in creep rate.

These effects of neutron irradiation on the creep behavior of niobium can be rationalized in terms of a glide-climb model.9 During neutron irradiation, significant numbers of defects are generated above the equilibrium concentration normally present during thermal creep. Some vacancies and interstitials avoid recombination in the cascade region and are free to participate in kinetic processes. The more mobile interstitials escape from the cascade regions and interact with dislocations, thereby enhancing the climb rate over dispersed barriers. It is this enhancement that is associated with the instantaneous increase in creep rate.

Excess vacancies in the cascade regions are presumably trapped by impurity atoms and other vacancies forming small clusters. In the sequential climb-glide process of creep, the defect clusters apparently act as randomly (dispersed obstacles to dislocations gliding on slip planes. As irradiation continues, the size and density of the clusters increase, and the creep rate decreases progressively. An eventual steady-state creep rate during irradiation at constant flux, temperature, and stress is anticipated. It is assumed that the average size and density of defect clusters would be maintained essentially constant. in a state dynamic equilibrium.

When the beam was turned off, there was a sudden decrease in creep rate resulting froni an abrupt decrease in the number of defects arriving at the sites of climb events. The subsequent gradual increase in creep rate is probably associated with the dissolution of vacancy clusters. When recovery is complete, the creep rate in the absence of neutron irradiation is expected to return to the steady-state thermal value.

2. Results

The in-situ creep apparatus[10] has been reconfigured and interfaced with the 23G mm diameter RTNS-II target. We have also completed computer load control and data acquisition of pertinent variables for testing. Our first creep test at RTNS-II war, run mid-August on an annealed niobium specimen at 550 and 600°C and stresses near 120 MPA. With RTNS-II operating at a source strength of 1.1 x 10^{13} neutrons/second, the flux at the sample was 1.2 x 10^{16} n/m^2-s.

In this most complex, fully instrumented in-situ experiment that has been run under 14 MeV neutron irradiation, pronounced perturbations in creep behavior were produced at. 550°C by cycling the high energy neutron beam quickly on dnd off the highly stressed minispecimen. Deformation rates jumped momentarily by 30-50% when the beam was flashed onto the specimen and decreased a similar amount upon beam removal (Fig. 3).

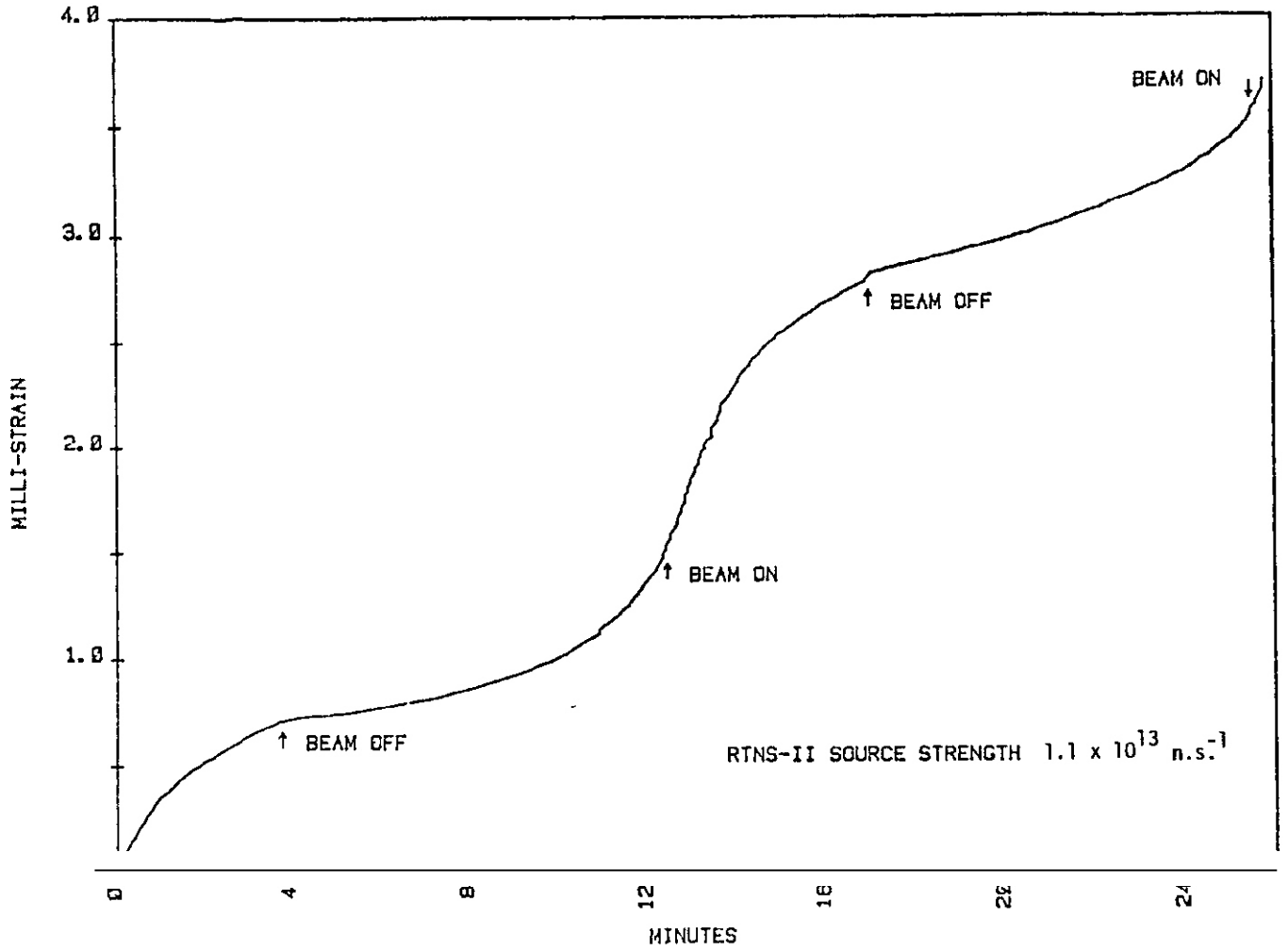

FIGURE 3. Beam on - beam off in-situ creep test of niobium at 550°C. flux at the sample position was 1.2 x 10^{16} n/m^2-s.

Accelerated rates are attributed to an instantaneous increase in concentration of radiation induced point defects in the material. Decelerated rates apparently resu't from the rapid removal of excess defects when the beam is abruptly turned off.

Preliminary analysis of our data indicates that the effects of 14 MeV neutron irradiation on the creep of niobium observed in this experiment are similar to effects observed on creep of niobium under high energy neutrons from the Be(d,n) source at U.C. Davis.[9]

3. Conclusions

The neutron flux at the RTNS-II is sufficient, even with small targets, to study transient creep effects in niobium. In the next in situ creep test scheduled for late November, we will investigate the effects of flux and stress levels on the creep behavior of niobium in the region 450-600"C.

When the experiments are complete, their analysis in terms of the creep model proposed should yield information on the number of defects which escape collision cascades to participate in diffusion processes as well as provide estimates of the thermal stability of cascade remnants.

VI. REFERENCES

1. M. W. Guinan, R. N. Stuart, C. E. Violet and J. H. Kinney, OAFS Quarterly Technical Progress Report, DOE/ET-0065/6, July 1979.

2. M. T. Robinson and I. M. Torrens, Phys. Rev. 9, 5008 (1974).

3. O. M. Schwartz, J. O. Schiffgens, O. G. Doran, G. R. Odette and R. G. Ariyasu, Computer Simulation for Materials Application, NBS 1, 75 (1976).

4. J. R. Beeler, Jr. and D. G. Besco, Phys. Rev. 134A, 530 (1964).

5. R. N. Stuart, M. W. Guinan and R. J. Borg, Rad. Eff. 30, 129 (1976)

6. H. L. Heinisch, OAFS Quarterly Technical Progress Report, DOE/ET-0065/5, May 1979.

7. M. W. Guinan, R. N. Stuart and R. J. Borg, Phys. Rev. B15, 699 (1977).

8. R. A. Johnson and W. D. Wilson, in Proceedings of the Internationdl Conference on Interatomic Potentials and Simulation of Lattice Defects (Eds., P. C. Gehlen, J. R. Beeler, Jr. and R. I. Jaffee), Plenum Press, N. Y., 1972, p. 301.

9. R. R. Vandervoort, W. L. Barmore and A. K. Mukherjee, Rad. Eff. 41, 113 (1979).

10. W. L. Barmore, A. W. Ruotola, and R. R. Vandervoort, Rev. Sci. Instrum. 50, 844 (1979).

VII. FUTURE WORK

A. Calculations are currently being extended to 10 keV and detaile comparisons with MARLOWE are in progress.

B. After completion of the niobium studies, in-situ creep experiments will be carried out in nickel.

VIII. PUBLICATIONS

See references 9 and 10 above.

I. PROGRAM

Title: Radiation Damage Analysis and Computer Simulation
Principal Investigator: Don M. Parkin
Affiliation: Los Alamos Scientific Laboratory of the University of California

II. OBJECTIVE

The objective of this work is to develop displacement functions for polyatomic materials.

III. RELEVANT DAFS PROGRAM PLAN TASK/SUBTASK

SUBTASK II.B.2.3 Cascade Production Methodology
II.B.4.1 Interface with other designs and other tasks
II.B.4.2 Develop theory of spectral and rate effects

IV. SUMMARY

The computer code NGFITP was developed to generate analytic fits to the displacement functions generated by the code DISPLC. After considerable investigation, it was determined that for the general case, a rational function provided the best results wherea; functions using a "damage energy" like form were not adequate. For the typical displacement function, sixteen parameters are required to define the fit function. The complexity of the displacement functions in general requires this rather large number of parameters.

V. ACCOMPLISHMENTS AND STATUS

A. Displacement Functions for Polyatomic Materials -- D. M. Parkin (LASL) and C. A. Coulter (The University of Alabama).

One of the central goals of this program is to provide displacenent functions for polyatomic materials for use by the Fusion Development and Technology community. The computer code NGFITP has been written to generate this inforriation.

As was the case with polyatomic damage energy functions, **it** was not possible to derive a universal forniula for the total, n_{ij}, and net, g_{ij}, **displacement functions.** Furthermore, the complexity of the functional behavior of n_{ij} and g_{ij} at low energy and their range of behavior for various materials iiiade the adoption of functional forms for the **fit** function difficult. In the threshold region, the behavior of n_{ij} and g_{ij} can change several times above E^d and $2E^d$ as indirect threshold energies are reached.

Initial attempts *to* develop **fit** functions of a "damage energy type" were successful for many inaterials but proved to be inadequate for the general case. A rational function of the form

$$F_{ij}(E) = (1 - E^{thr}_{ij}/E)^{N^{thr}_{ij}} R(X) \qquad (1)$$

$$X = \ln (E/E^{thr}_{ij})^{pwr}$$

$$R(X) = P(X)/Q(X)$$

$$P(X) = P_1 + P_2 X + \ldots + P$$

$$Q(X) = |(1 + P_{mordr + 2} X^{mordr})|$$

was found to give acceptable fits for the **general** case. **If** a fit is obtained for values of n_{ij} or g_{ij} above 1.0×10^{-2}, then rnordr = 10 is usually required to obtain fits with a maximum error less than 1", **the average** error being much less than 1%. Although Eq. 1 is clearly not an ideal solution, the displacement functions are most useful in computer calculated displacement cross sections and as such the cumbersome nature of Eq. 1 is not a handicap.

VI. FUTURE WORK

A report that will contain the fit parameters for a large number of materials is currently being generated.

I. PROGRAM

Title: Irradiation Effects Analysis (WHOll/EDA)
Principal Investigator: D. G. Doran
Affiliation: Hanford Engineering Development Laboratory

II. OBJECTIVE

The objective of this work is to determine the effects of high energy neutrons on daiiiage production and evolution, and the relationships of these effects to effects produced by fission reactor neutrons. Specific objectives of current work are the planning and performance of an irradiation program at the Rotating Target Neutron Source (RTNS)-II and post-irradiation testing.

III. RELEVANT DAFS PROGRAM TASK/SUBTASK

SUBTASK II.B.3.2 Experimental Characterization of Primary Damage State; Studies of Metals

II.C.6.3 Effects of Damage Rate and Cascade Structure on Microstructure; Low-Energy/ti igh-Energy Neutron Corre1ations

II.C.II .4 Effects of Cascades and Flux on Flow; High-Energy Neutron Irradiations

II .i.17.1 Microstructural Characterization; Monitor and Assess New Methodologies

II.C.18.1 Relating Low- ana High- Exposure Microstructures; Nuc1eation Experiments

IV. SUMMARY

Binary alloys based on Cu and Ni and micro-tensile specimens of stainless steel, Ni, anu Ti6Al4V have been prepared for irradiation at RTNS-II during the next quarter.

V. ACCOMPLISHMENTS AND STATUS

A. RTNS-II Irradiation Program -- N. F. Panayotou and E. K. Opperman (HEDL)

1. Specimen Preparation

a. Binary alloys and ferritics

The fabrication of the following binary alloys (composition in atomic percent) is complete:

Ni-5% Al	Cu-5% Al
Ni-5% Si	Cu-5% Ni
Ni-8% Si	Cu-50% Ni
Ni-5% Mn	Cu-5% Mn

As discussed previously[**]) these alloys will be used to study impurity effects on cascades, and cascade effects on phase stability.

We are also procuring stock material of HT-9 and other iron-base alloys. HT-9 is a commercial ferritic alloy that is currently a prime candidate for use in fusion reactors. Other ferritics of interest include Fe-0.3% Cu and pure Fe. The presence of small concentrations of copper in the ferritic steels formerly used for light water reactor pressure vessels has been found to lead to the degradation of fracture toughness under neutron irradiation. The microstructural-mechanical property response of ferritic alloys to 14 MeV neutrons is clearly of interest and specimens of selected ferritic alloys will be included in future RTNS-II irradiations.

b. Vanadium

R. H. Jones of Battelle-Northwest has reported that vanadium wire stock obtained from the DAFS stockpile has suffered extensive delamination. Based on tensile tests and our microhardness measurements we have concluded that the delamination is due in part to a large interstitial

impurity concentration in this material. Sources of higher purity vanadium are currently being investigated.

c. Micro-tensile specimens

The preparation of micro-tensile specimens and the development of techniques for testing and analyzing them are proceeding on schedule. Micro-tensile specimens (see Figure 'I) have been produced from 0.76 mm (0.030 inch) diameter stock of MFE stainless steel, Ni and Ti6Al-4V by a chemical milling technique. TEM disk specimens are available from the same material neats used for the stainless steel and Ni specimens so direct comparisons of microhardness and tensile test results will be possible.

Accurate determination of specimen dimensions is essential since each chemically milled specimen is unique. Specimen diameters are measured with a non-contacting laser system. This technique provides a rational basis for tire selection of micro-tensile specimens for irradiation.

A specially designed device for testing these specimens in uniaxial tension is shown in Figure 2. Tests on control (unirradiated) specimens of 20% CW 316 stainless steel have produced very reproducible results which correlate well with NSM Handbook values. For details of the test results and experimental procedures see the Alloy Developnient for Irradiation Performance (ADIP) quarterly progress report [2] for this reporting period.

2. Status of Irradiations

Specimen irradiations at RTNS-II have been delayed approximately seven weeks due to equipment difficulties at the facility. The third HEDL experiment, which is centered on the irradiation of TEM disk specimens of binary alloys, is currently scheduled for October 24. HEDL's fourth experiment, our first irradiation of micro-tensile specimens, is

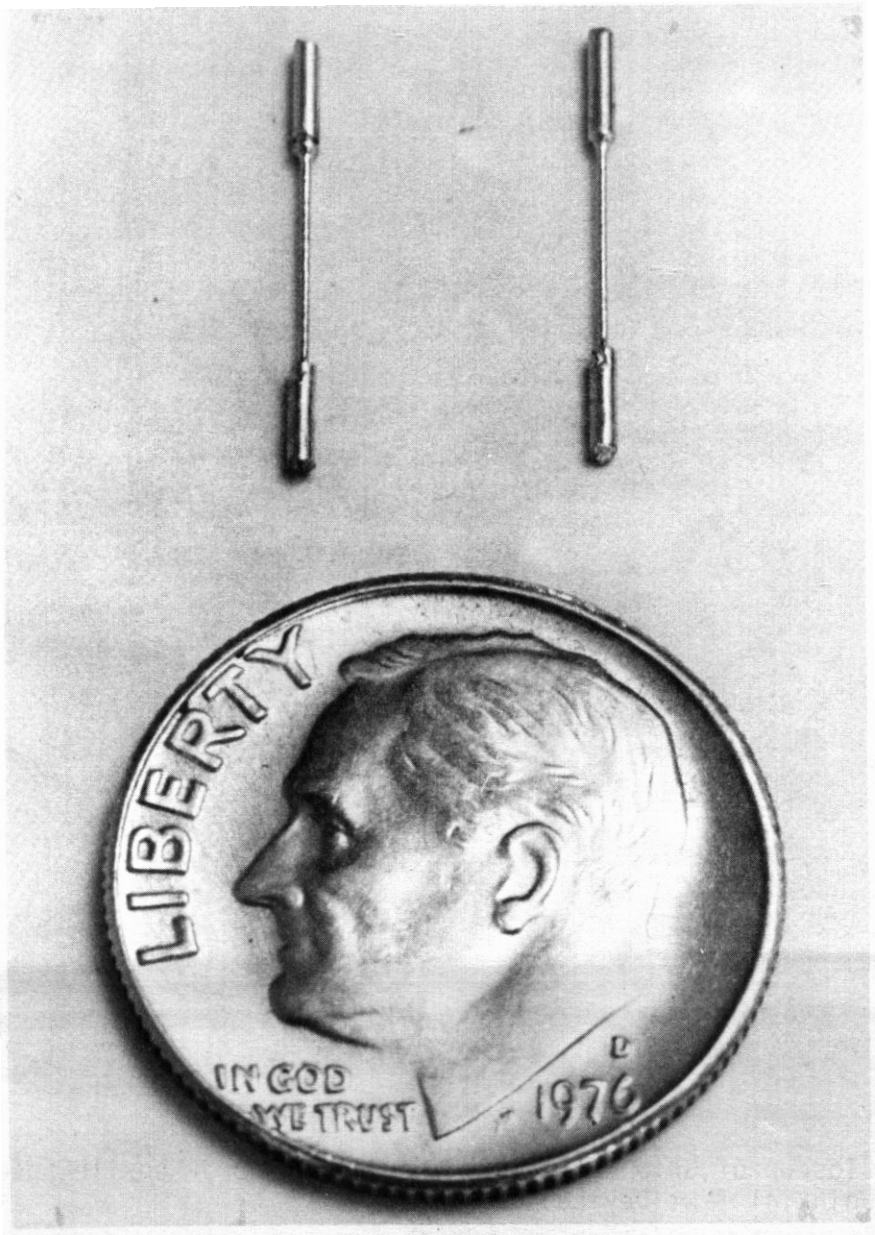

FIGURE 1. Micro-Tensile Specimens of Stainless Steel Which Will be Irradiated in HEDL Experiment No. 4 at RTNS-II.

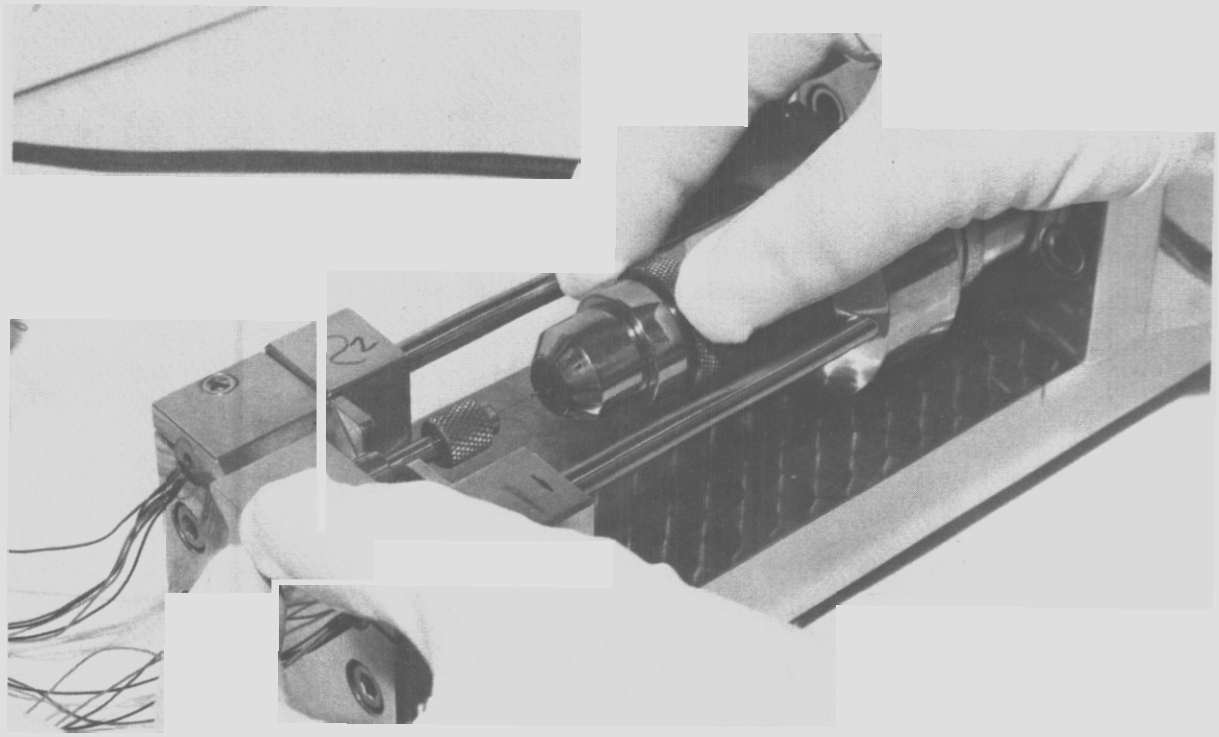

FIGURE 2. Closeup of Gripping Mechanism of the Micro-Tensile Specimen Uniaxial Test Device.

currently scheduled for December 3.

Dosimetry results were obtained from LLL for HEDL experiment No. 1. This irradiation was terminated prematurely due to RTNS-II equipment problems. The data indicate that the peak fluence sustained was 3.9 x 10^{17} n/cm^2 (E $\sim$14 MeV) rather than the goal fluence of 10^{18}. Furthermore, the measured peak and minimum fluence values differed by only a factor of 15, rather than the factor of 30 predicted from calculated flux maps. We suspect that this result is due to a larger than expected effective deuteron beam diameter at the target. Although short term (several hours) dosimetry by LLL indicates a 1 cm beam diameter, there was no mechanism in place during our first experiment whereby the beam position could be directly monitored over an extended period of time. It is postulated that beam motion increased the effective spot size. The dosimetry values correlate well with calculations using spot sizes of 1.5 to 2 cm.

Modifications of the beam line at the facility which will allow for the reproducible positioning of the deuteron beam on the target have now been completed.[3]

The analysis of the dosimeters from HEDL experiment No. 2 is nearing completion.

VI. REFERENCES

1. Damage Analysis and Fundamental Studies Quarterly Progress Report, January-March 1979, DOE/ET-0065/5, May 1979.

2. Alloy Development for Irradiation Performance Quarterly Progress Report, July-September 1979, DOE/ET-0058/7.

3. Damage Analysis and Fundamental Studies Quarterly Progress Report, April-June 1979, DOE/ET-0065/6, July 1979.

VII. FUTURE WORK

1. Microhardness and TEM examinations of irradiated specimens from HEDL experiments 1 and 2 will be continued.

2. HEDL RTNS-II experiments 3 and 4 will be irradiated.

3. Test data from bench tests of the 1st generation RTNS-II furnace will be analyzed.

VIII. PUBLICATIONS

None.

CHAPTER 4

SUBTASK C: DAMAGE MICROSTRUCTURE EVOLUTION AND MECHANICAL BEHAVIOR

I. PROGRAM

Title: Irradiation Response of Materials

Principal Investigators: S. Wood, J. A. Spitznagel and W. J. Choyke

Affiliation: Westinghouse Research and Development Center

11. OBJECTIVE

The objective of this work is to assess the phenomenology and mechanisms of microstructural evolution in materials exposed to simultaneous helium injection and creation of atomic displacement damage by a second ion beam.

III. RELEVANT DAFS PROGRAM TASK/SUBTASK

SUBTASK II.C.I, II.C.2, II.C.3, II.C.5, II.C.9, II.C.18

IV. SUMMARY

Swelling and mean cavity diameter curves are compared for 316SS targets of solution annealed (1050°C) and 20% cold worked material subjected to dual-ion bombardment with He and Si ions in the 500-750°C temperature range. Both conditions show a direct correlation between swelling and mean cavity diameter, whereas the cavity number densities are essentially constant. This suggests that swelling is linked to cavity growth rather than nucleation. Rapid cavity growth at 600°C in SA 316SS is reflected by a tremendous swelling which is not observed in the cold worked condition. A precipitation sequence for acicular precipitates leading to cavity alignment is postulated, and it is suggested that the temperature sensitivity of the rapid cavity growth regime in SA 316SS is related to solute segregation.

V. ACCOMPLISHMENTS AND STATUS

A. Swelling and Cavity Growth in Simultaneously Bombarded 316SS

Dual bombardment experiments utilizing He and Si^{+6} were performed at temperatures of 500-750°C, and preliminary data on cavity number densities and swelling reported previously[**)] have now been updated to include more recent data. The temperature dependence of swelling in the 20% cold worked material is given in Fig. 1, for a damage level of 2.5-5.0 dpa, damage rate of $\sim 1 \times 10^{-4}$ dpa/s, and appm He/dpa ratio of ~7-13. Characteristic void microstructures are included for each experimental temperature. At, or below, 600°C no visible cavities were imaged with the TEM, but this may reflect failure to detect very small bubbles beyond the limit of instrumental resolution. Peak swelling *is* around 10 vol % at 650°C and is directly correlated with mean cavity diameter (Fig. 2) since cavity number density (not shown) is essentially constant ($\sim 5 \times 10^{14}$ cavities/cm^3) over the entire temperature range. Swelling in solution annealed (SA) material for a damage level of 1.4-5.0 dpa and appm He/dpa ratio ~13 (Fig. 3) can also be correlated with mean cavity diameter. This suggests that for both conditions, changes in swelling are associated with cavity growth rather than nucleation.

The enormous swelling observed at 600°C in the SA 316SS is often accompanied by cavity alignment and appears to be related to acicular precipitate formation. This is discussed further in the next section. Attempts to quantify the vol % swelling at this temperature are now in progress – the value quoted (~100%) is merely an estimate derived from stereo transmission electron microscopy observations. Conventional cavity sizing techniques utilizing the Zeiss Particle Size Analyzer are not applicable because of the dendritic nature of the cavities. Thus, an upper bound or maximum swelling value is being determined by use of a quantamet automated image analysis system.

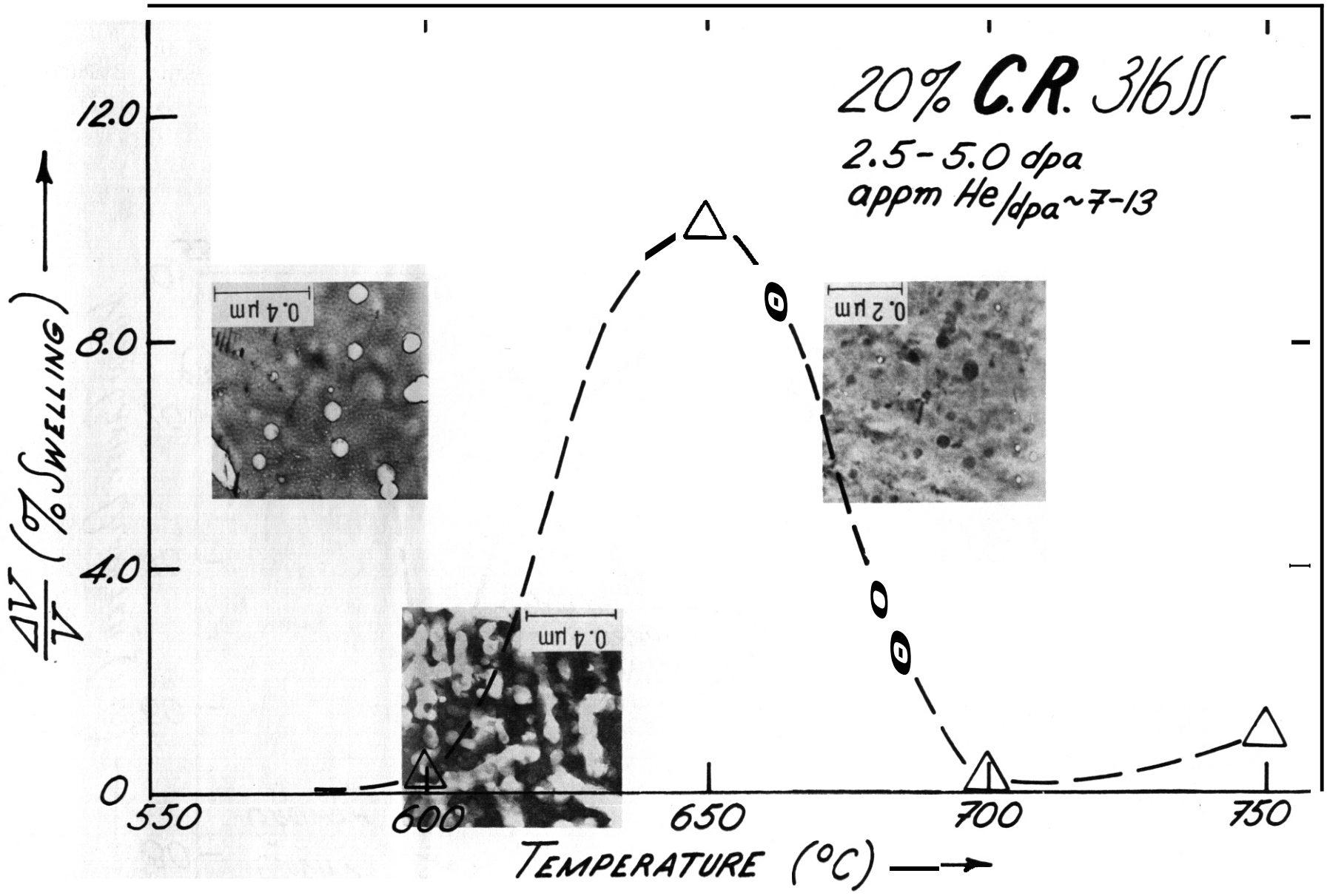

FIGURE 1. Swelling as a Function of Temperature for 20% Cold-Worked 316 SS. Representative Microstructures are shown for each data point.

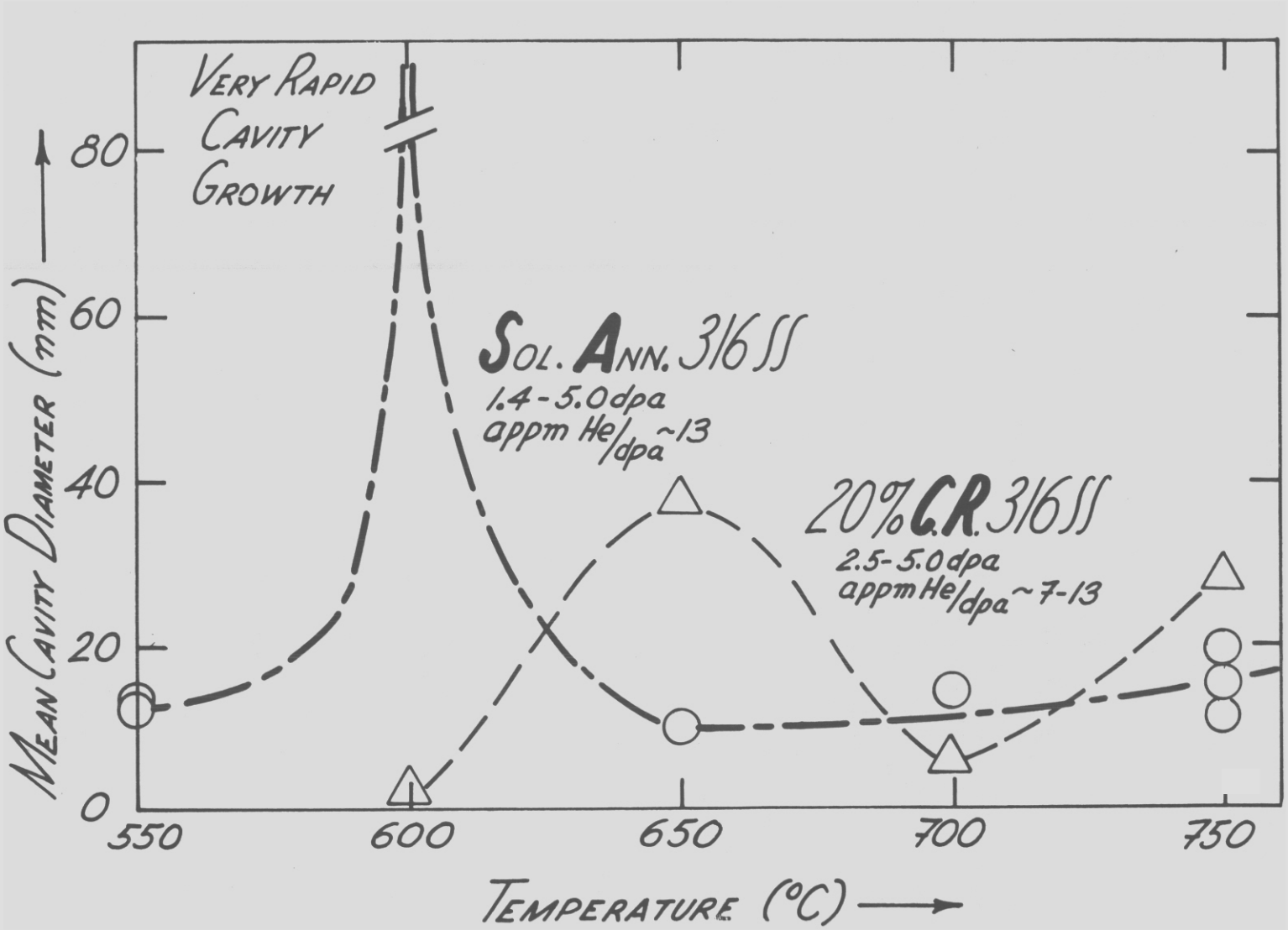

FIGURE 2 Mean Cavity Diameters for Both SA and 20% CR 316 SS at the Various Experimental Temperatures Note correlation with swelling curves in Figures 1 and 3.

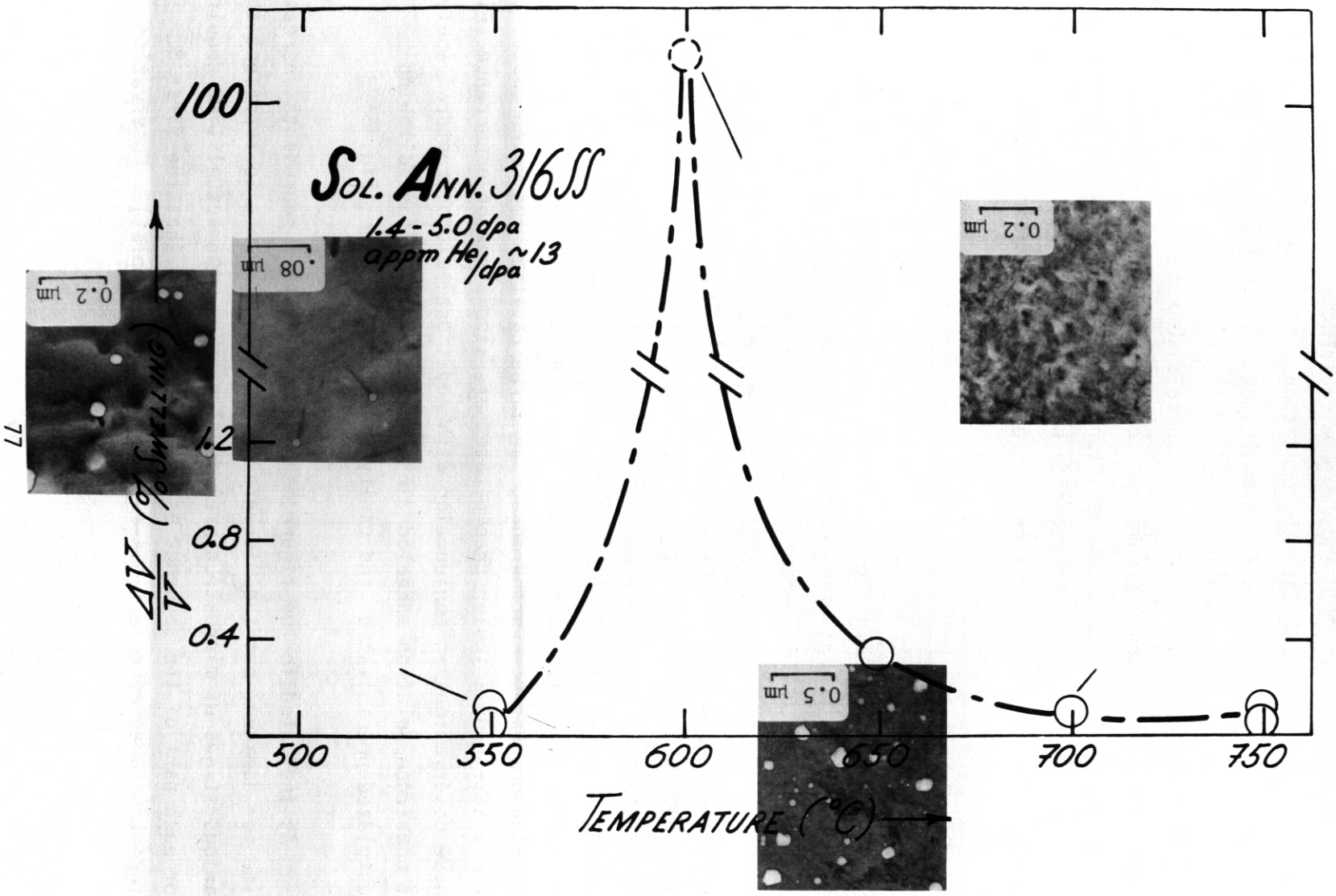

FIGURE 3. Swelling as a Function of Temperature for SA 316 SS with Representative Microstructures.

Acicular precipitate formation has also been observed in cold-worked 316SS, as shown in the 700 and 750°C microstructures presented in Fig. 1. However, it is apparent that the conditions for rapid growth were not met for the range of temperatures investigated. Since it is believed that nucleation of acicular precipitates occurs on dislocations, one might anticipate a larger volume fraction in cold worked material because of the higher dislocation density compared to a solution annealed condition. This is not observed, however. Competition among the numerous nucleation sites apparently results in a high density of precipitate nuclei of "subcritical" size which do not have a chance to grow to a stable acicular configuration.

B. Postulated Origin of Cavity Alignment in SA 316SS at 600°C

As presented in an earlier report[2, 3], simultaneous implantation of helium and bombardment with the heavy ion beam at damage rates of $\sim 2.5 \times 10^{-5}$ - 1.0×10^{-4} dpa/s may result in very rapid cavity growth at 600°C in solution annealed 316SS. This rapid growth phenomenon is often accompanied by the alignment of cavities in [110] directions which link up to produce the dendritic networks observed previously.[2] It has been determined that the occurrence of this excessive voidage is very temperature sensitive and is also critically dependent upon both the atomic displacement and helium injection rates, being suppressed at both high helium levels and high dpa rates. Furthermore, the large cavities are often coated with precipitate, and acicular precipitates are also a common occurrence (Fig. 4). These observations in conjunction with additional microstructural analyses of bombarded solution annealed 316SS specimens yield the following postulated precipitation and cavity alignment sequence (Fig. 5).

As indicated in the figure, the horizontal axis represents increasing time (or damage), but the micrographs are intended only to represent the various stages of microstructural development -- the actual time required for each part of the sequence is not known. (Note that the first 3 microstructures represent non-explosive growth samples). Observations

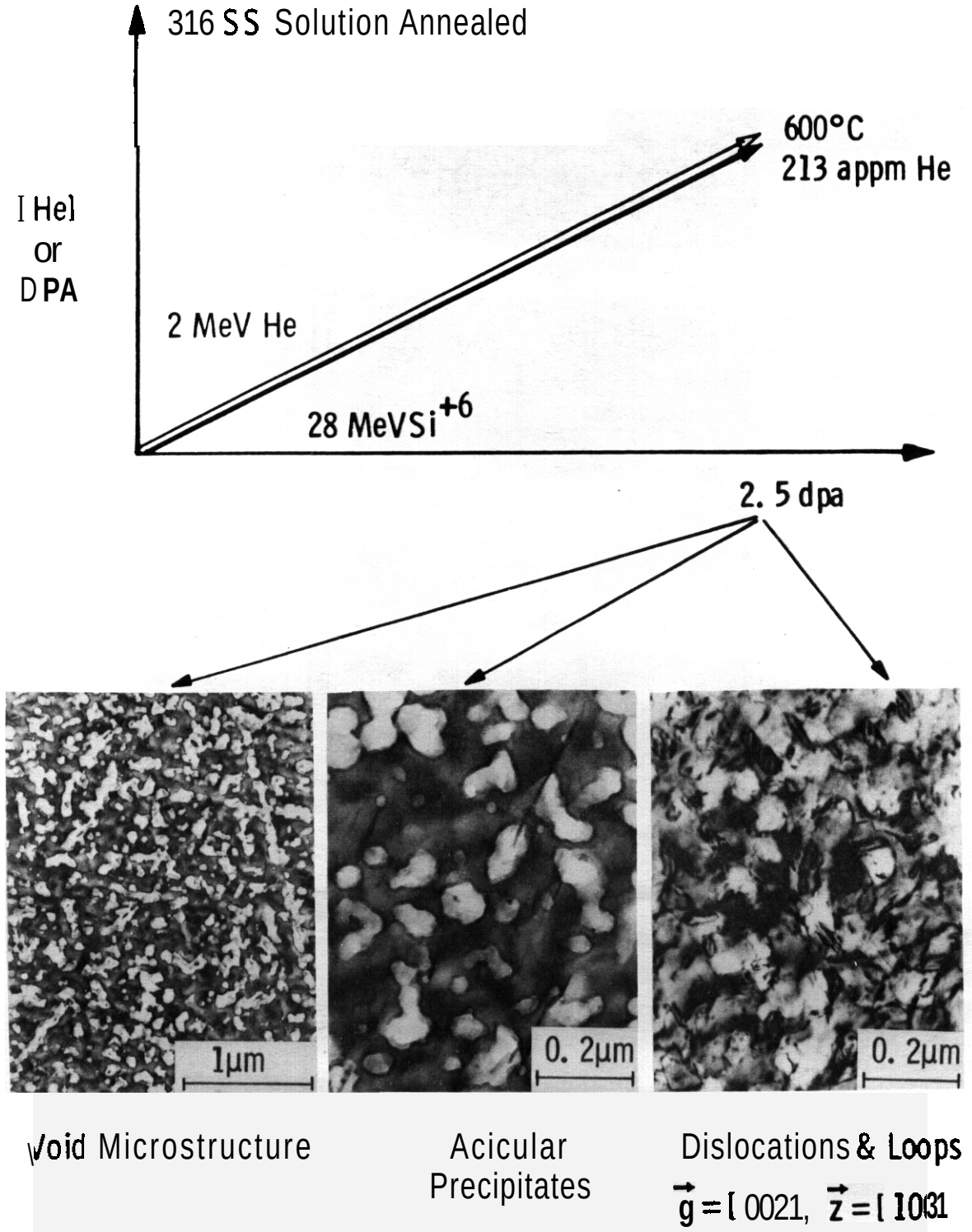

FIGURE 4. Microstructures Induced in SA 316 SS at a Relatively Low Damage Rate (2.9×10^{-5} dpa/s) and Moderate He Level.

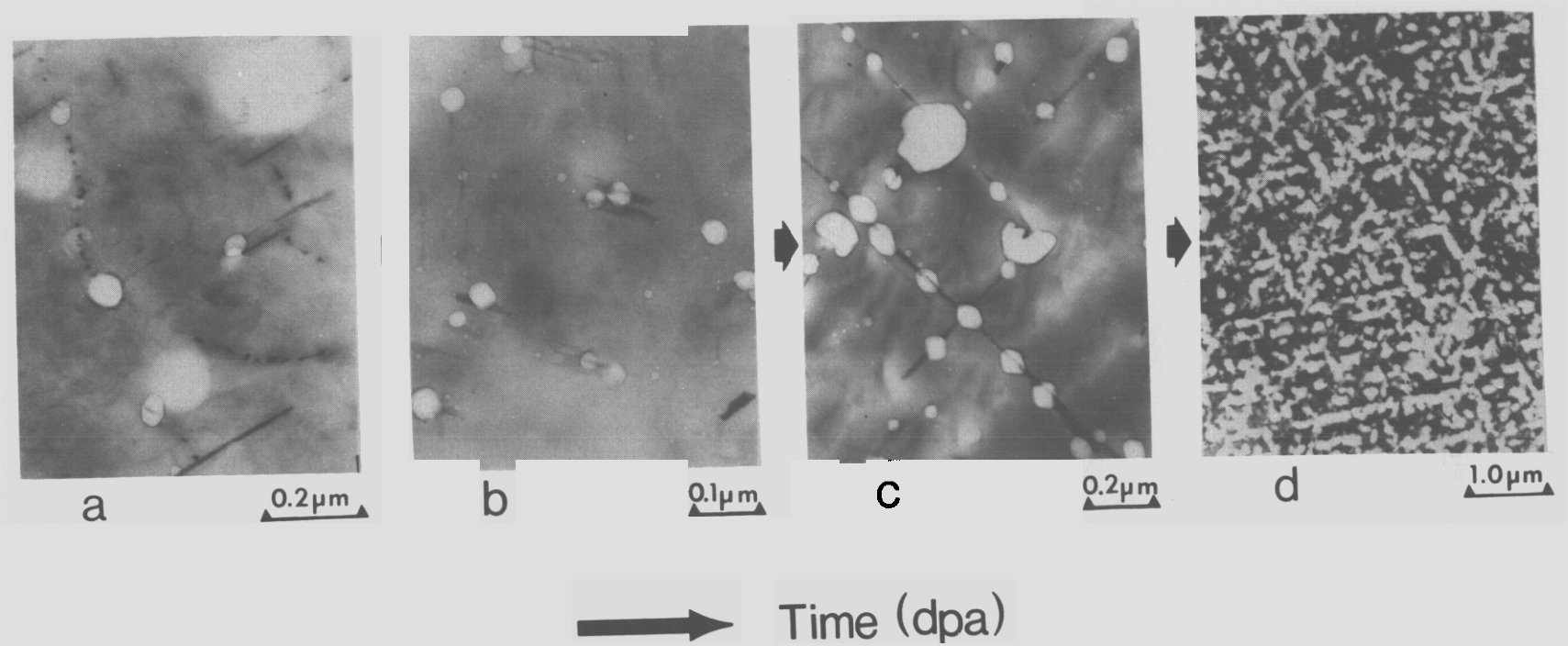

FIGURE 5. Postulated Precipitation Sequence, Producing Cavity Alignment, in SA 316 SS

suggest that the initial nucleation sites of the acicular precipitates are dislocations (Fig. 5a), and that these small particles grow and coalesce to produce the more common needle-shaped particles (Figs. 5a, b). All types of these precipitates act as preferential sites for cavity nucleation, and they are usually aligned along [110] directions. They can grow to lengths of 1 or 2 μm (Fig. 5c). This micrograph clearly shows how cavity alignment in [110] directions may arise due to selective nucleation along the length of the needle-shaped phase. Subsequent cavity growth and coalescence could, therefore, yield the dendritic morphologies observed at 600°C (Figs. 4 and 5d).

Another observation worthy of note is that many of the cavities associated with acicular precipitates show little evidence of the precipitate actually passing through the cavity. This suggests redistribution of the second phase material, perhaps around the cavity, which is supported by the transmission electron microscopy results presented in Fig. 6. The bright field image (Fig. 6a) shows several of the acicular precipitates associated with smaller cavities. The corresponding dark field image (utilizing the reflection indicated in Fig. 6c) also shows precipitate coatings around the larger cavities. This result indicates that both phases have the same crystal structure and tends to support the redistribution idea. Further work is in progress, using scanning transmission electron microscopy and energy dispersive X-ray analysis to determine the chemistry and structure of both the coatings and the acicular precipitates. Preliminary analyses comparing the matrix composition with that at the precipitate-cavity interface indicate a Ni, Si, P and Cu enrichment of the latter (Fig. 7).

Precipitation is obviously enhanced by the segregation of Si, Ni etc. to point defect sinks during irradiation, and several previous observations of Ni_3Si[4,5] and silicide formation[6] (e.g. G-phase) have been made in either neutron or Ni^{+6} ion irradiated 316SS. The formation of a Ni, Si-rich second phase can thus also occur during dual-ion bombardment. Another

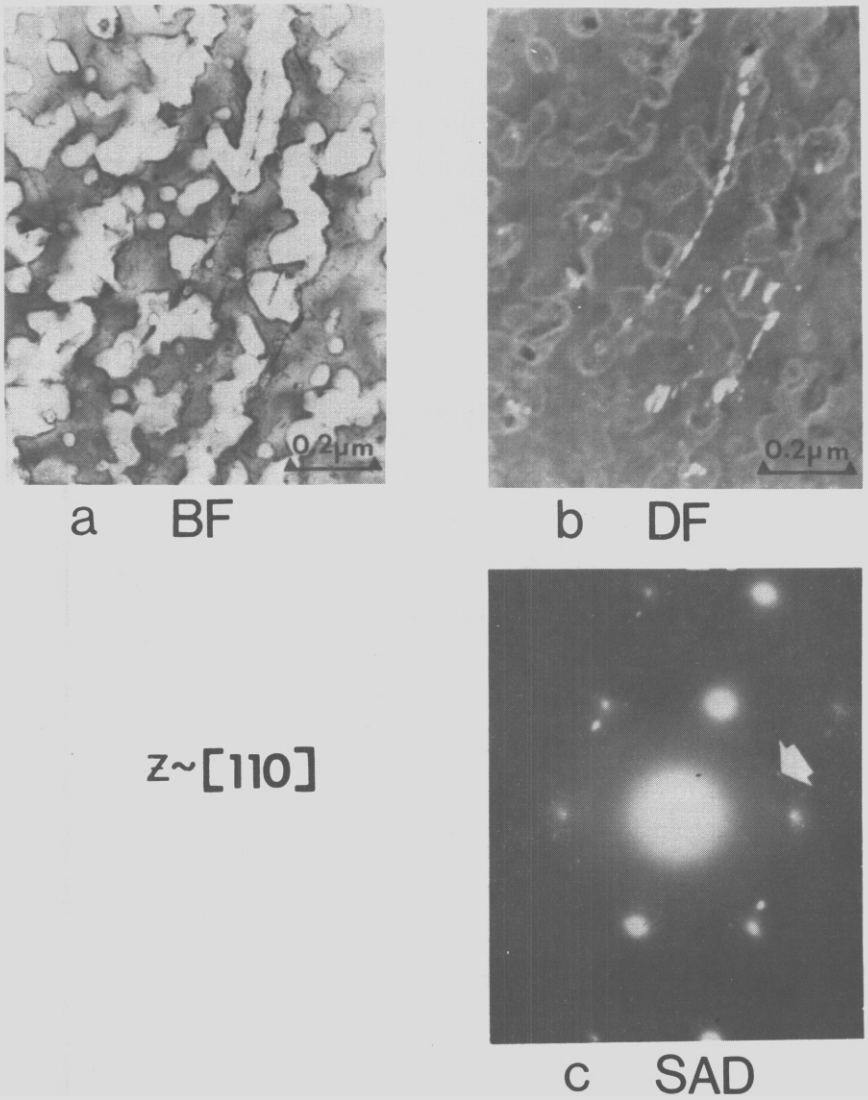

FIGURE 6. Cavity and Precipitate Microstructures in SA 316 SS Simultaneously Bombarded at 600°C; A, B are bright and dark field micrographs, respectively, and C shows the reflection used for B.

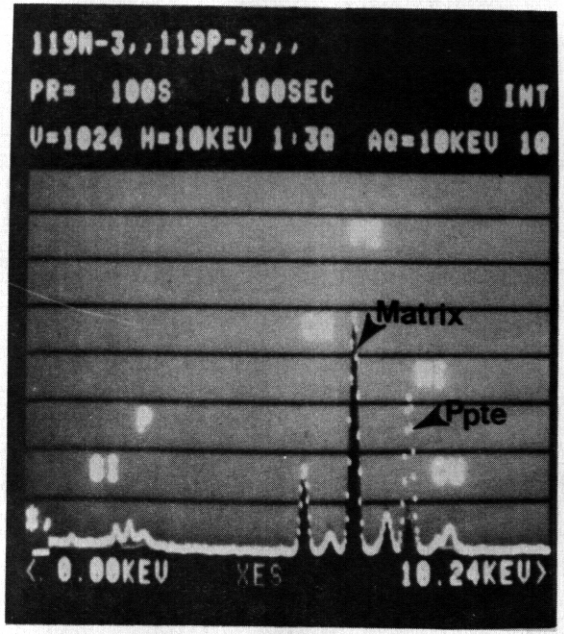

FIGURE 7. Comparison of Energy Dispersive X-ray Analyses Obtained in the Matrix and at a Cavity/Precipitate Interface (Labeled Ppte).

factor, which we suspect is linked to the excessive voidage observed at 600°C, in SA 316SS, is the predicted temperature dependence of solute segregation given by the Johnson and Lam kinetic model.[7] This definitely indicates that segregation passes through a maximum at some intermediate temperature. At low temperatures irradiation produced defects are relatively immobile so that recombination rates will be relatively high, thus reducing the fraction of defects (and solute) which reaches sinks. At high temperatures, solute segregation is inhibited by enhanced recombination due to a higher equilibrium vacancy concentration and faster back-diffusion. Experimental confirmation of this predicted temperature dependence of solute segregation has been obtained by Potter et al[8] in a Ni-12.7 at % Si alloy irradiated at 3×10^{-3} dpa/s by 3.5 MeV Ni^{+} ions. For this material, maximum solute segregation occurred at ~575°C, which is very close to the 600°C at which the excessive swelling occurs in SA 316SS.

Hence, to summarize, it is suggested that the cavity alignment observed in SA 316SS at 600°C is a direct result of heterogeneous nucleation of cavities on acicular precipitates which are aligned in [110] directions. Subsequent cavity growth and coalescence produces the dendritic networks so frequently seen in this material. The temperature sensitivity of the excessive voidage is believed to be directly related to the temperature dependence of solute segregation. If segregation is maximized at 600°C, this will yield, initially, a larger volume fraction of precipitates to serve as nucleation sites and may also contribute to rapid cavity growth if Si moves by a coupled solute-vacancy mechanism since Si is known to segregate towards void surfaces[9]. Most importantly, the results suggest that high helium levels and cold work reduce the tendency for acicular precipitate formation and for rapid cavity growth and coalescence.

VI. REFERENCES

1. J. A. Spitznagel and W. J. Choyke, DAFS Quarterly Progress Report DOE/ET-0065/3, July-September (1978).

2. S. Wood, J. A. Spitznagel and W. J. Choyke, DAFS Quarterly Report, DOE/ET-0065/5, January-March (1979).

3. S. Wood, J. A. Spitznagel and W. J. Choyke, DAFS Quarterly Report, DOE/ET-0065/6, April-June (1979).

4. H. R. Brager and F. A. Garner, J. Nuc. Mat. 73 (1978) pp. 9-19.

5. C. Cawthorne and C. Brown, J. Nuc. Mat. 66 (1977) pp. 201-202.

6. T. M. Williams, J. M. Titchmarsh and D. R. Arkell, J. Nuc. Mat. 82 (1979) pp. 199-201.

7. L. E. Rehn et. al., J. Nuc. Mat. 74 (1978) pp. 242-251

8. P. R. Okamoto and L. E. Rehn, J. Nuc. Mat. E (1979) pp. 2-23.

9. P. R. Okamoto and H. Wiedersich. J. Nuc. Mat. 53 (1974) pp. 336-345.

VII. FUTURE WORK

STEM and EDS analyses of both acicular precipitates and the precipitate-coating on cavities in the 600°C SA 316SS samples (MFE heat) will be continued. Data from the study of the effect of vacuum ambient (i.e. changing partial pressure of oxygen) on the rapid cavity growth regime in SA 316SS at 600°C will be completed and reported. Additional experiments to investigate the particular damage and helium injection rates for which excessive cavity growth occurs are in progress, and microstructural analysis followed by data computerization will be performed. Dual-ion bombardment studies of a vanadium alloy (either V-20 Ti, Vanstar 7 or V-15 Cr-5Ti) are being initiated to determine the effects of different H and Co partial pressures in the target chamber on microstructural evolution.

TEM observations on aged and dual-ion bombarded MFE 316SS are continuing and are being compared with ANL results on the same material.

VIII. PUBLICATIONS

None

I. PROGRAM

Title: The Radiation Induced Order-Disorder Transformation in Cu_3Au
Principal Investigator: P. Wilkes
Affiliation: University of Wisconsin

II. OBJECTIVE

To understand and model the effects of radiation on microstructural stability.

111. RELEVANT OAFS PROGRAM PLAN TASK/SUBTASK

Subtask II.C.1.2. Modeling and Analysis of Effects of Material Parameters on Microstructure.

IV. SUMMARY

A model for ordered alloys is presented which describes the combined effects of radiation disordering and radiation enhanced ordering. The model uses the assumptions of Bragg-Williams ordering in a kinetic form in which the ordering energy is a linear function of order. Point defect concentrationsare introduced into the ordering kinetics so that the effect of the radiation (through enhancement of such concentrations) can be described. Both time dependent and steady-state solutions to the resulting ordering rate equation are presented.

All the available data on irradiation of Cu_3Au with fast and thermal neutrons are reviewed and presented as functions of long range order parameters (S) versus dose. All the curves at a wide variety of temperatures are fitted successfully with the model using the same diffusion parameters throughout. The implications and predictions of the model for future experiments are discussed.

V. ACCOMPLISHMENTS AND STATUS

A. The Radiation Induced Order/Disorder Transformation in Cu_3Au -- R. Zee and P. Wilkes (University of Wisconsin - Madison)

1. Introduction

Experiments have shown[1,2] that under irradiation, previously stable alloys may undergo phase transformations. Second phase particles may dissolve or new ones form. One mechanism that has been proposed to explain phase dissolution is radiation disordering.[3] It has been demonstrated that the free energy change involved in this process is often comparable to the free energy of formation of alternative phases and irradiation modified phase diagrams have been calculated on this basis.[3] The process of radiation disordering has long been known to occur and has recently been reviewed.[3,4] However, enhanced radiation ordering is also a common observation so that the situation is evidently not simple. A model which permits calculations of both ordering and disordering rates under irradiation has recently been proposed[3] and it is the purpose of this paper to apply this model to all the available data on irradiation of Cu_3Au. This has been irradiated more than any other ordered alloy in the literature and good thermal ordering data is also available.

We demonstrate in this paper that all the available data can be satisfactorily fitted with this model, using the same parameters for the diffusional behavior of the alloy throughout.

2. The Radiation Disorder Model

When an energetic particle interacts with the lattice atoms of a metal to produce a cascade of displacements, it is well known that many point defects are produced. In the process many more atoms can change position (replacements) than are displaced to produce Frenkel defects. In

an ordered alloy such replacements produce disorder. This disorder has been used to make cascade regions visible in the electron microscope.[5]

In addition to these local cascade replacements, replacement collision sequences can also produce disorder. This occurs when a chain of atoms is displaced forward leaving a vacancy behind and an interstitial at the forward end. Since each atom moves one atomic jump a previously ordered row may become disordered. Such rows are not of course visible on the electron micrographs. This type of disordering can also occur when the energetic particle is unable to produce cascades.

In all these damage processes point defects are produced and at temperatures where they are mobile, enhanced diffusion occurs. Since ordering is presumed to occur by such point defect motion, the kinetics of the ordering process will also be enhanced. Radiation disordering theory must be able to predict both ordering and disordering rates under irradiation.

Before ordering changes can be described, it is necessary to choose some way to measure the order itself. We choose the long range order parameter of Bragg and Williams,[6]

$$S = \frac{f_{A\alpha} - X_A}{1 - X_A} \qquad [1]$$

where $f_{A\alpha}$ is the probability that an A atom will be on a site in the α sublattice and X_A is the fraction of A atoms. This parameter takes no account of how the disordered atoms are arranged and in particular ignores short range order. Unlike thermal ordering, however, where short range order is critical, most radiation disordering is random. This is because the knock-on atoms have energies that are larger than the ordering energy and are thus likely to be little influenced by it. However, this ensures that the model will not be applicable to an initially disordered alloy which is likely to develop order by domain nucleation.

2a. Radiation Disordering

If the replaced atoms are exchanged randomly then the disordering rate due to irradiation is obviously dependent upon the instantaneous order

$$\left(\frac{dS}{dt}\right)_{irr} = -\varepsilon K S \qquad [2]$$

ε is the number of replacements per displaceinent and K is the displacement rate. Equation [2] only requires that at long times S should tend to zero.

The fact that, in a single set of replacements, atoms are not replaced randomly (as in a replacement sequence, for example) does not matter as long as successive sets are randomly spaced, so that no correlation occurs between neighboring sets. Departure from randomness in a single set only changes the magnitude of ε, not the form of the equation. Because Equation 2 is so general, it has been deduced for and fcund to fit many different irradiation disorder situations.(7,8)

Theoretical values for the replacement ratio ε have varied greatly, from ~ 1-1000, and this is a topic of great interest currently from the point of view of cascade studies. The calculation isverydifficult requiring first a determination of the number and size distribution of cascades and then estimates of the replacements and displacements for each size of cascade. For fast neutrons, values of $\varepsilon \gtrsim 100$ seem reasonable while for thermal neutrons values somewhat below this are expected ($\varepsilon \sim 10$). 1 MeV electrons generally give $\varepsilon \sim 1$.

2b. Enhanced Thermal Ordering

Although the thermodynamics of ordering has been heavily studied, the kinetics of ordering has been the subject of very few papers. In a

standard paper Dienes[9] used chemical rate theory for a "reaction" in which a pair of wrong or antistructure atoms transform to a right or ordered pair. The result differs from the usual chemical rate result in that increase in the degree of order (extent of reaction) increases the ordering rate. This is, of course, the essence of the ordering reaction as a cooperative process. Dienes demonstrated that if the ordering energy (the energy difference for a wrong and right pair) was taken to be a linear function of the order, the Bragg-Williams result for the equilibrium order was obtained. For the case of Cu_3Au this lies below the experimentally determined values.[10] In the chemical rate approach the rate constant for the ordering reaction is given as

$$k_1 = \nu_1 \exp(-U/k_BT)$$

while the reverse disordering reaction rate constant is

$$k_2 = \nu_2 \exp[-(U+V)/k_BT]$$

where U is the energy barrier for the pair exchange and V is the ordering energy. ν_1 and ν_2 are the frequency factors which in Bragg-Williams theory are taken to be equal. Dienes obtains

$$\left.\frac{dS}{dt}\right|_{thermal} = \nu \exp(-U/k_BT)\{X_AX_B(1-S)^2 - \exp(-V/k_BT)[S+X_AX_B(1-S)^2]\}$$

where the ordering energy $V=V_oS$.

In order to use this theory to describe the radiation enhanced thermal ordering rate $(dS/dt_{thermal*})$, it is necessary to introduce the point defect concentrations. We first assume:

i) In Cu_3Au interstitial motion does not change the degree of order. The large size difference between the atoms makes this reasonable and it is justified experimentally by the absence of ordering in stage I

annealing.[11]

ii) Ordering proceeds by a vacancy mechanism. The increased ordering rates under irradiation are good evidence for this.

The point defect concentrations can be introduced into the rate constants by assuming that the pair exchange occurs by successive vacancy jumps. The energy barrier to pair exchange (U) then becomes the energy barrier to vacancy motion in the double vacancy jump (E_m^o). The frequency is the vacancy attempt frequency divided by two for a double jump. The probability of a vacancy being in position to make the exchange is $(Z_\alpha + Z_\beta - 2)\, C_v$. The term in brackets is the number of sites around the pair, Z_α being the number of α sites around a β site and Z_β the number of β sites around an α site. C_v is the vacancy concentration. The rate constants are then

$$k_1 = (\nu_v/2)\, C_v\, (Z_\alpha + Z_\beta - 2) \exp(-E_m^o/k_B T) \qquad [3]$$

$$k_2 = (\nu_v/2)\, C_v\, (Z_\alpha + Z_\beta - 2) \exp[E_m^o + v)/k_B T]$$

With these changes we can now write the ordering rate as,

$$\frac{dS}{dt}_{thermal} = (Z_\alpha + Z_\beta - 2)(\nu_v/2) C_v \exp(-E_m^o/k_B T)\{X_A X_B (1-S)^2\} \qquad [4]$$

As we have noted irradiation increases the vacancy concentration C_v and so enhances dS/dt. To include this effect we use rate theory following Brailsford and Bullough[12] to obtain C_v. The use of this theory implies that the point defects have reached steady-state concentrations, so that

$$\frac{\partial C_i}{\partial t} = 0 = K_i - D_i C_i k_i^2 - \alpha C_i C_v \qquad [5]$$

$$\frac{\partial C_v}{\partial t} = 0 = K_v - D_v C_v k_v^2 - \alpha C_i C_v + Z_v D_v \rho_d C_{ve}$$

$$K_i = K(1-f_i)$$

$$K_v = K(1-f_v) \quad .$$

K_i and K_v are the rates of production for the defects which survive both correlated recombination (i.e., immediate recombination of a Frenkel pair) and loop collapse in the cascade. (The **f** are the fractional losses to these effects.) D_i and D_v are the interstitial and vacancy diffusion coefficients, α is the recombination constant,[12] while k_i^2 and k_v^2 are the effective sink strengths for interstitials and vacancies, respectively. We consider the case where dislocations are the dominant sinks so that the sink strengths can be written in terms of the dislocation bias factors Z_i and Z_v and the dislocation density ρ_d.

$$k_i^2 = Z_i \rho_d \qquad [6]$$

$$k_v^2 = Z_v \rho_d \quad .$$

Inserting all these parameters, the coupled equations (5) can be solved to give C_v and C_i.

The total vacancy concentration obtained by this solution is:

$$C_v = C_{ve}/2 - Z_i D_i \rho_d/(2\alpha) + \{[C_{ve}/2 + Z_i D_i \rho_d/(2\alpha)]^2 + k_v D_i Z_i/(Z_v D_v \alpha)\}^{1/2} \qquad [7]$$

where the equilibrium vacancy concentrations $C_{ve} = \exp(-E_f/k_B T)$.

Note that the vacancy diffusion coefficient is given by $D_v = D_{ov} \exp(-E_m/k_B T)$ in which the average energy for vacancy motion E_M is not necessarily the same as the energy for an <u>ordering</u> jump E_m^o since the vacancy

can move over large distances on the copper sublattice only. C_v can now be inserted into the ordering equation [4j to give the enhanced ordering rate.

2c. The Order Rate Equation

The actual ordering rate is a balance between the radiation disordering rate of equation [2] and the radiation enhanced ordering rate obtained by inserting the enhanced vacancy concentration of equation [7] into equation [4], giving

$$\frac{dS}{dt} = \frac{dS}{dt}_{irr} + \frac{dS}{dt}_{thermal^*} \qquad [8]$$

where the terms on the R.H.S. are obtained from equations [2] and [4]

Results from equation 8 using the parameters of Table 1 are shown in Figure 1. The choice of these particular values will be discussed in the next section. Here certain general features of the results are considered.

Figure 1 shows the variation of dS/dt together with that for its components dS/dt_{irr} and $dS/dt_{thermal^*}$. The latter is identical in form to $dS/dt_{thermal}$ obtained by Dienes[9] except for a multiplying factor which contains the enhanced vacancy concentration. This varies with temperature as shown in Fig. 2. At higher temperatures near the order transition temperature the multiplying factor approaches unity as there are so many thermal vacancies that the irradiation increase in their concentration is negligible. Radiation then makes little difference and the thermal ordering rate dominates. At lower temperatures the enhanced ordering rate is the dominant rate as Figure 1 shows. In this region enhanced ordering under irradiation will be observed. If the temperature is lowered still further, although the enhancement in vacancy concentration increases, vacancy mobility decreases and eventually disappears.

Table 1

Parameters Used in Fitting Cu_3Au Data

Vacancy motion energy	E_m = 0.8 eV
Vacancy ordering motion energy	E_m^o = 0.84 eV
Vacancy pre-exponential diffusion coefficient	D_{ov} = 7.8 x $10^{-5} m^2/s$
Vacancy formation energy	D_{fv} = 1.28 eV
Vibrational frequency	$\nu_v = \nu_i = 10^{13}$ Hz
Interstitial motion energy	E_{im} = 0.12 eV
Interstitial pre-exponential diffusion coefficient	D_{oi} = 7.8 x 10-7m2/s
For fast neutrons	
Vacancy loss fraction	f_v = 0.95
Replacement to displacement ratio	ε = 80
For thermal neutrons	
Vacancy loss fraction	f_v = 0.0
Replacement to displacement ratio	E = 20
Dislocation bias for interstitials	Z_i = 1.03
for vacancies	Z_v = 1.0
Recombination coefficient	$\alpha = 10^{21}/m^2 \times D_i$
Copper concentration	X_A = 3/4
Ordering energy	V_o = 0.35 eV

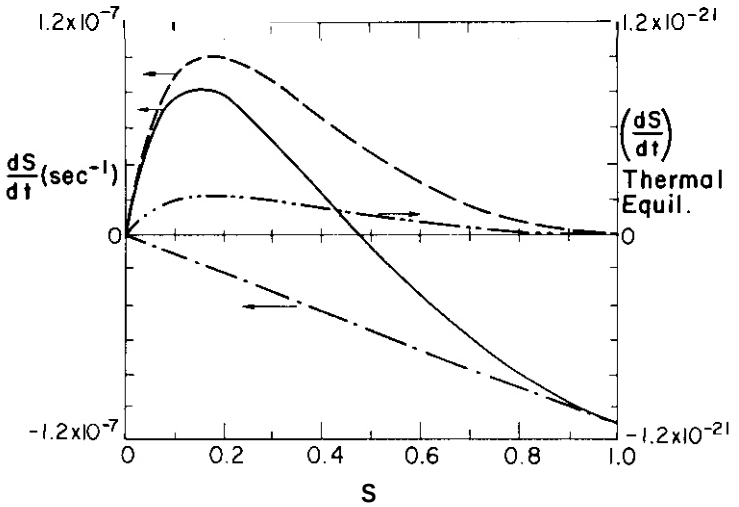

Fig. la - The rate of change of order as a function of order parameter S under fast neutron irradiation at 27°C. The irradiation rate was 1.4×10^{-9} dpa/s and ρ_d was $1.7 \times 10^{13}/in^2$.

. - Irradiation disordering rate

- - - - - The irradiation enhanced ordering rate

——— The sum of the above

- .. - .. - The thermal ordering rate in the absence of irradiation, for comparison (note: different scale).

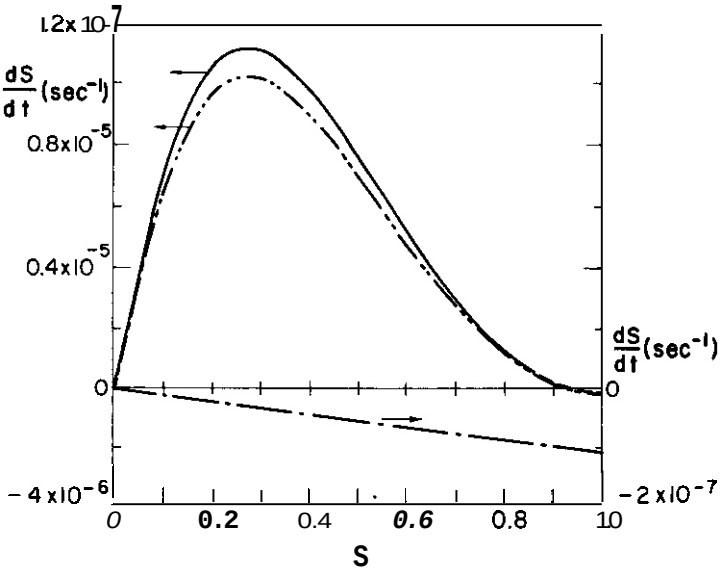

Fig. lb - As for la but at 332°C. The radiation enhanced ordering curve is so close to the solid line as to be indistinguishable except at high S. (Note different scale for radiation disordering rate.)

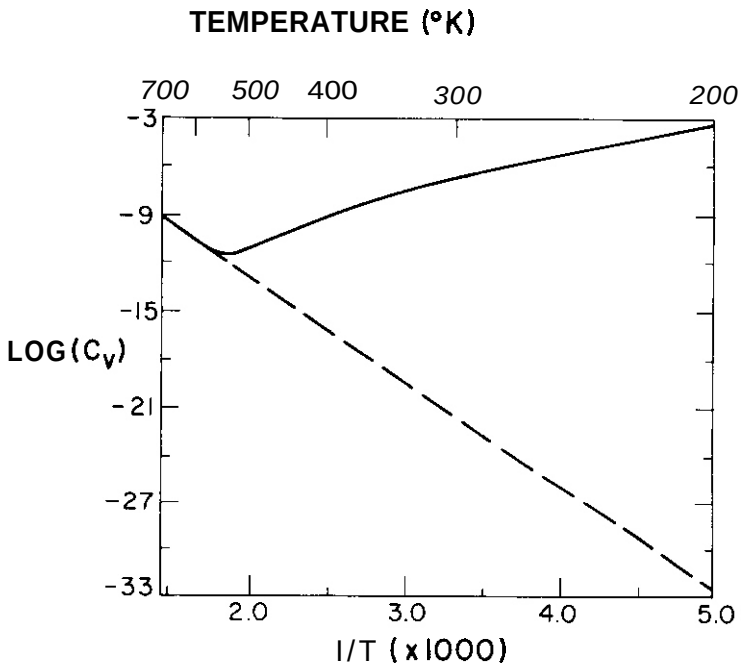

Fig. 2 - The enhanced steady-state vacancy concentration caused by fast neutron irradiation, according to equation (7), versus reciprocal temperature (solid line).

The equilibrium vacancy concentration as shown in the dashed line. The parameters used are those in Table 1 with $\rho_d = 1.7 \times 10^{13}/m^2$ and $K = 1.4 \times 10^{-9}$ dpa/sec.

Under these conditions the ordering rate is small and the disordering dominates. At a sufficiently low temperature this will always occur. The most interesting temperature region is where radiation ordering and disordering rates have the same magnitude.

It is obvious from the dS/dt curves that no useful information can be obtained from change-of-slope measurements of ordering rates at fixed S values. Figure 3 shows dS/dt for fixed S values plotted against the reciprocal of temperature. Since dS/dt can be either positive or negative no Arrhenius plot can be meaningful. In fact, the slope of such a plot can vary anywhere from $-\infty$ to $+\infty$. Over limited temperature ranges certain values of activation have been extracted[11,13] but the results, as this analysis shows, are meaningless.

Figure 1 also indicates that the ordering and disordering rates balance each other to give dS/dt = 0 over a wide range of S values, depending on temperature. These values of S define a steady-state condition under irradiation where no further change in order takes place. These steady-state values (S_∞) were determined by setting equation [8] equal to zero and solving numerically. The results are shown as a function of temperature for fast and thermal neutrons in Figure 4a.

The various temperature range effects are clearly visible. At high temperature the thermal equilibrium curve is approached. As the temperature decreases the order remains high due to the enhanced ordering from excess vacancies. As these become immobile at still lower temperatures radiation disordering dominates to give low S_∞ values. It is clear that there is a narrow temperature range over which S_∞ changes very rapidly. This range is itself strongly dependent on the rate and type of irradiation (i.e., upon εK). Fig. 4a shows a plateau in the S_∞ values in the mid-range for the fast neutron case. This arises from the vacancy behavior. At very low temperatures the enhanced vacancy concentration is very large because the immobile vacancies cannot diffuse to sinks and can

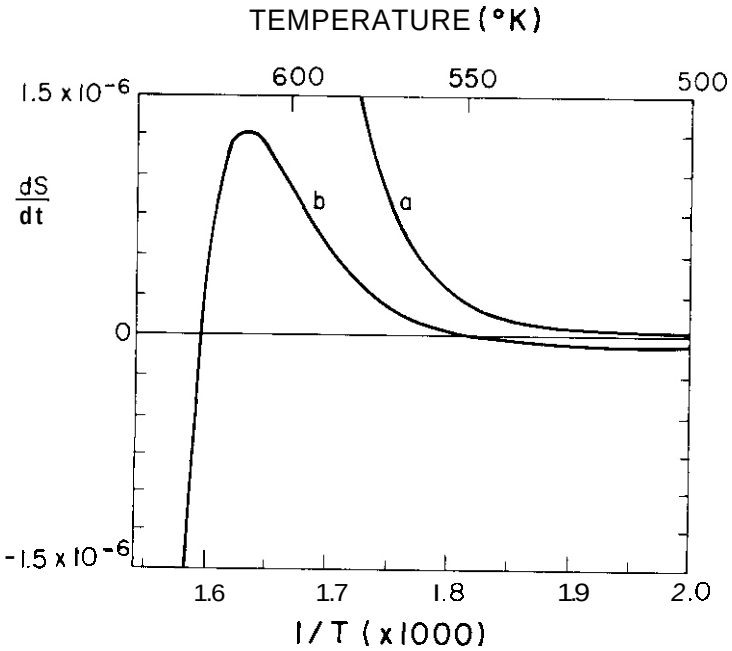

Fig. 3 – The order/disorder rate under fast neutron irradiation as a function of reciprocal temperature for two values of S

(a) S = 0.8

(b) S = **0.87**

Note **the slope for** (b) **includes a wide range** of **positive and negative values making an Arrhenius** plot **meaningless. The parameters used were** ρ_d = **1.7** x **10**^{13}/m^2 **and** K = **1.4** x 10^{-9} dpa/sec.

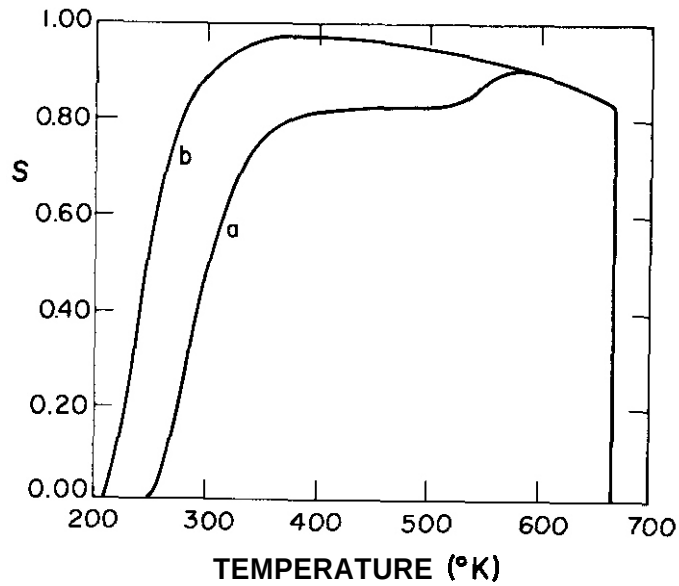

Fig. 4a - The steady-state degree of order, S, as a function of temperature for (a) fast neutrons and (b) thermal neutrons. The parameters are taken from Table 1 with

ρ_d = 1.7 x 1013/m2 and K = 1.4 x 10^{-9}dpa/s for (a)

ρ_d = $10^{12}/m^2$ and K = 2.5 x 10^{-10}dpa/s for **(b)**

only be removed by recombination with the interstitials (Fig. 2). However, in spite of this high concentration, the diffusion of matrix atoms remains low because of low vacancy mobility (Fig. 4b, 4c). In the intermediate range the matrix diffusion ($D_v C_v$) remains constant with temperature increase because the falling vacancy concentration is balanced by the increasing mobility (Fig. 4b). The enhanced ordering rate follows the matrix diffusion closely in this range giving a similar shape of the S_∞ curve of Fig. 4a to the diffusion curve in Fig. 4b.

At some low value of S_∞ the whole idea of long range order will break down. At this value the alloy will nucleate new ordered domains on reordering, rather than growing back into the oriyinal large domains by a gradual increase in S. This critical value of S is not known. (Experiments are not possible by thermal treatment since values of S in Cu_3Au between S=0.8 *at* T_c and S=O are unobtainable by this means.)

The rate equation [6] has also been solved numerically for the time dependent case, using $S=S_0$ at $t=0$ as a boundary condition. The differential equation problem solving package EPISODE[14] was used for this. However, the results were very close to a simple modification of the time dependent analytic solution given in reference 3 (where $V_0 S$ now replaces the constant v_0).

$$S(t) = 1-p + \frac{p-q}{1-\left(\frac{S_0+q-1}{S_0+p-1}\right)\exp(zt)} \qquad [9]$$

where $z^2 = \varepsilon 2K2 + 4x[x + \varepsilon K/(1-S_e)]$

$p = (-\varepsilon K+z)(1-S_e)/2x$

$q = (-\varepsilon K-z)(1-S_e)/2x$

The rate constant x is given by

$$x = \nu C_v (Z_\alpha+Z_\beta-2)\, Z_\beta[(X_A/X_B)(1-y_e + \Gamma y_e^2)]^{1/2} \qquad [10]$$

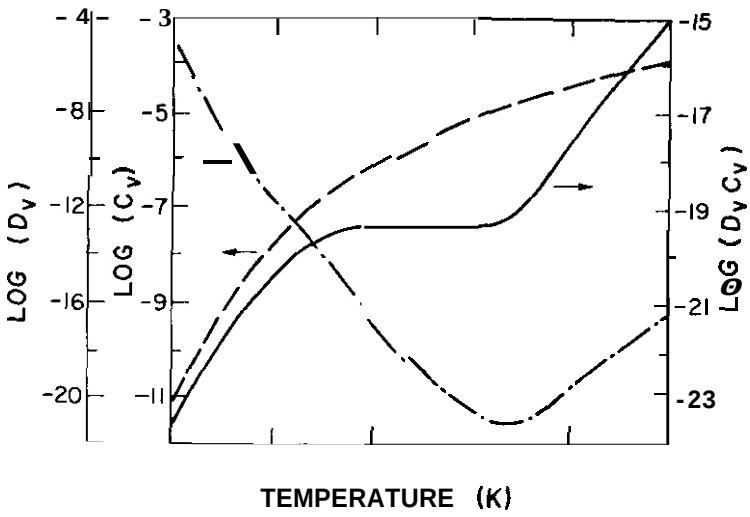

Fig. 4b - The matrix diffusion parameters ($D_V C_V$) for fast neutrons as a function of temperature (solid line). Note the plateau which gives rise *to the* plateau in Fig. 4a line (a). This arises from the balance between a falling vacancy concentration (dot and dashes) and a rising vacancy diffusion coefficient (dashed line).

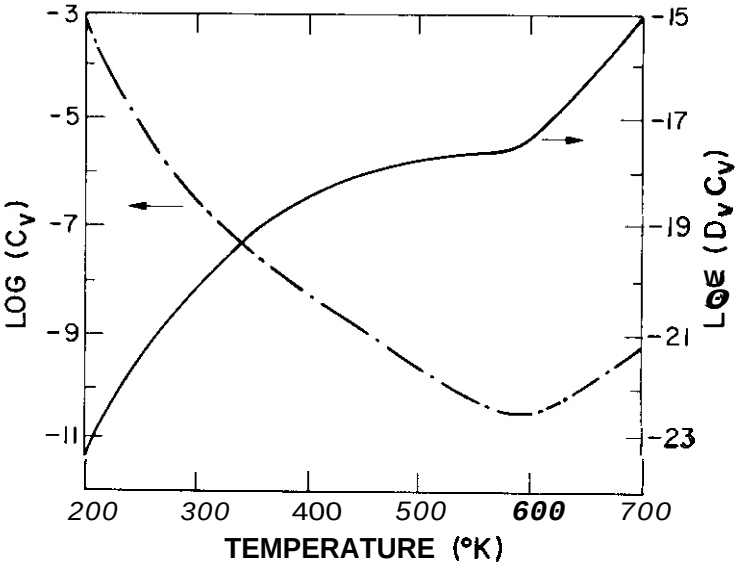

Fig. 4c – As for 4b but for thermal neutrons. Note the absence of a well-defined plateau (even with a logarithmic scale).

$$\cdot[1 + (y_e/2)\ (-V_o/k_BT + \frac{1-2\Gamma y_e}{1-y_e+\Gamma y_e^2})]$$

$$\cdot\exp\ (-E_m^0/k_BT)\ \exp\ [(V_o y_e - V_o)/2k_BT]$$

where $y_e = 1 - S_e$ and $\Gamma = X_A X_B$. A typical set of results in the middle temperature range is shown in Figure 5. These curves could be compared directly with experimental results of the order parameter under irradiation.

3. Radiation Disordering Data for Cu_3Au

No experimental values of order parameter determined directly from diffraction experiments on irradiated samples are available in the literature. However,. several experiments using electrical resistivity as a measure of order have been reported.

3a. Resistivity and the Order Parameter

There are two theories far the variation of S with electrical resistivity ρ. The first due to Muto[15] (A) gives

$$\rho_S = \Delta\rho\ \ (1-S^2) + \rho_{S=1} \qquad [11]$$

(where $\Delta\rho = \rho_{S=0} - \rho_{S=1}$)

The second theory due to Landauer[16] (B) applies to a mixture of two phases and was applied to irradiated and ordered Cu_3Au by Cook and Cushing,[17] it is expressed in conductivity terms:

$$\sigma_s = \frac{1}{4}\ \{(3\chi_2-1)\ \sigma_2 + (3\chi_1-1)\ \sigma_1 + [((3\chi_2-1)\sigma_2 + (3\chi_1-1)\sigma_1)^2 + 8\sigma_1\sigma_2]^{1/2}\} \qquad [12]$$

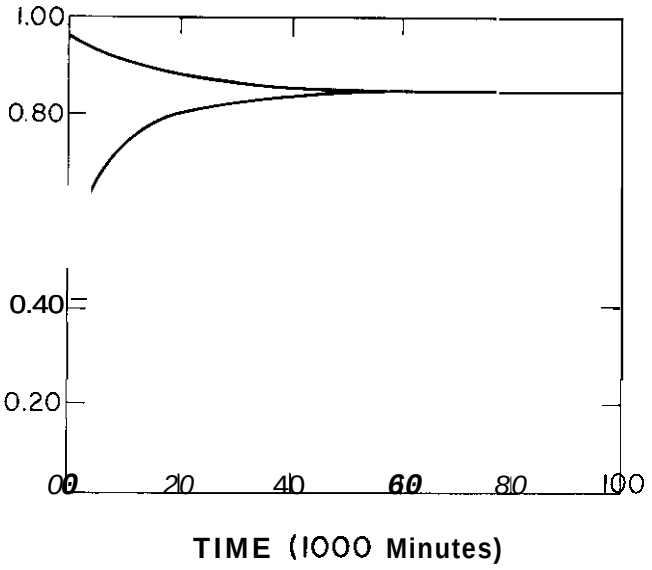

Fig. 5 - A typical set of time dependent results with the parameters of Table 1 and $K = 1.4 \times 10^{-9}$ dpa/sec and $\rho = 1.7 \times 10^{13}/m^2$.

where χ_1 is the fraction of material with conductivity a_1 and χ_2 similarly with σ_2.

This approach is of doubtful validity in an ordering alloy where disorder involves individual atoms being misplaced. A treatment like that of Muto which treats scattering from individual anti-structure atoms seems more reasonable. In addition to these two theories, Cook and Cushing (C) used a modification of Landauer's model, for which they did not claim high accuracy.

$$\sigma_s = \chi_1\sigma_1 + \chi_2\sigma_2 \quad .$$

All three models apply at constant temperature. Since $\rho_{s=1}$ and $\rho_{s=0}$ will have different temperature scattering the temperature coefficients are expected to be different. In addition well ordered Cu_3Au has an anomalous resistivity minimum[18] below about 100°K. Since the various resistivity measurements have been made at a variety of different temperatures, it is first necessary to determine $\rho_{s=1}$ and $\rho_{s=0}$ as functions of temperature. From the data of Passaglia and Love[18] at low temperatures and of Blewitt[19,20] at 0°C and 150°C it is possible to do this (Fig. 6). The resistivity anomaly[18] is clearly shown in the ordered alloy. In the disordered alloy it is much less. Taking these limits for each temperature for which data exists and using the information on the heat treatments it was possible to eliminate models B and C. Blewitt's "partially ordered" sample was quenched from 375°C after a long equilibration. From the experimental equilibrium order curve this should give a value of $S \sim 0.85$. It cannot be less than 0.75 which is the minimum value below T_c. Using the resistivity given by Blewitt of 3.7 μΩm at 4°K and 7.7 μΩm at 150°C we estimate a value of $S=0.83$ in good agreement with the equilibrium measurement. Theories B and C gave $S=0.39$ and $S=0.23$, respectively. Similar results were obtained for these two theories using other resistivity data, in all cases the S values were far too low. On the other hand, Muto's model (A) gave sensible values for S in the range

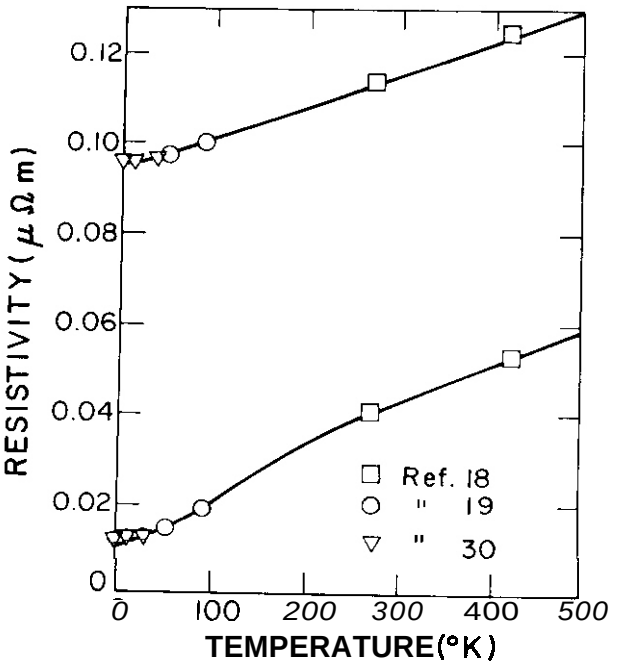

Fig. 6 - The resistivity as a function of temperature for the disordered state, S=0, (upper curve) and the ordered state, S=1.

0.8-1.0 after long time aging below T_c. In all subsequent analysis, therefore, equation [10] was used together with Figure 6 to determine S from the resistivity reported.

4. Fitting the Experimental Data

As is well known the Bragg-Williams model predicts low values of S when compared with experiment. Since our approach is phenomenological we have chosen to use a value of V_0=0.35 eV which gives a good fit to the equilibrium order parameter S_e as shown in Figure 7. In this way we obtain a correct value for the thermal ordering rate in the absence of irradiation. However, the T_c obtained from this value of V_0 by Bragg-Williams equilibrium theory will be larger than the experimental value. We simply cut-off the curve at this latter temperature T_c = 663°K.

The clearest and most complete data is that of Kirk and Blewitt.[19,20] This includes resistivity versus irradiation time for two S_0 values in a predominantly fast neutron flux at 150°C and 4°K, and one S_0 value for a primarily thermal neutron flux at 135°C. These are shown in Figure 8 with the theoretical curves fitted from our theory.

The 4°K data (Fig. 8a) are fitted with the disordering rate only (Equation 2). The only variation in these two curves is due to differing S_0 and this is fixed from the resistivity data. Both curves must have the same value of εK, so these data offer a severe test of the disordering model. Agreement is satisfactory, the small deviations probably being due to small deviations from a quadratic resistivity dependence on S.

To separate ε and K we need an independent estimate of the displacement rate K. This has been discussed by Kirk and Blewitt[19] in their own analysis of their data.

Using primary displacement cross sections of 3 barns and 5.5 barns for copper and gold, respectively, and displacement thresholds of 25 eV,

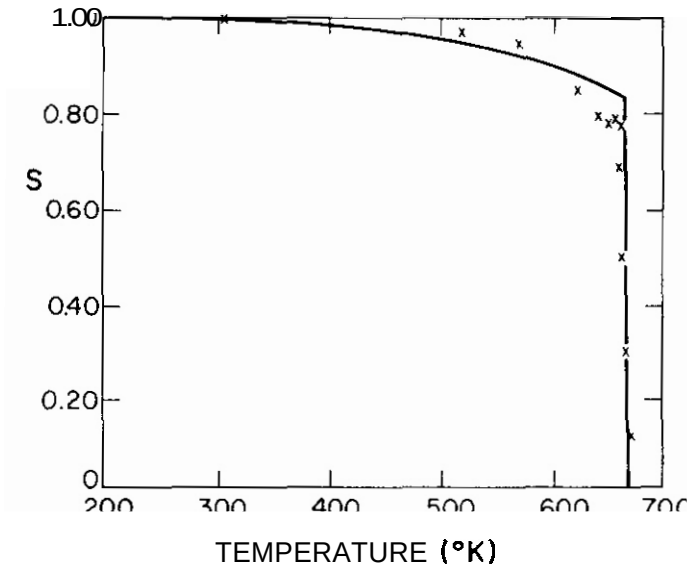

Fig. 7 - The thermal equilibrium order curve as a function of temperature (V_o = 0.35 eV). The experimental data are from Keating and Warren.[21]

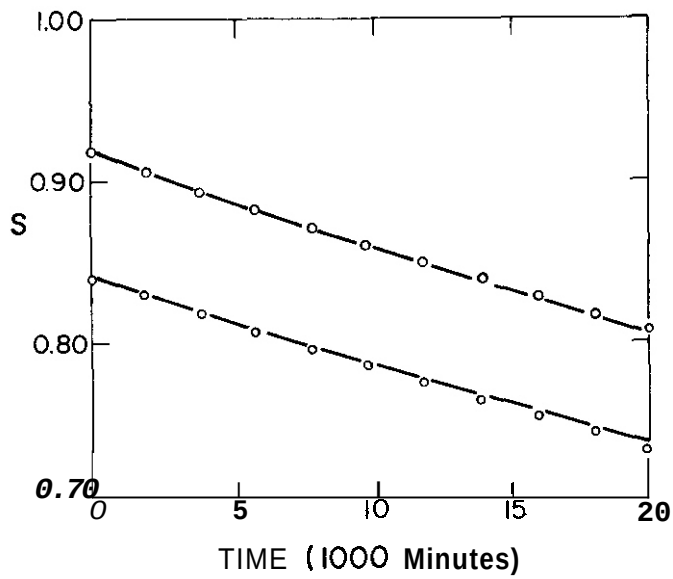

Fig. 8a - The change of order during fast neutron irradiation of Cu_3Au at 4°K from Kirk and Blewitt[19] (points). The two curves represent different starting values of the order parameter, The lines represent a data fit using the parameter values in Table 1 with $K = 1.4 \times 10^{-9}$ dpa/sec and $\varepsilon = 80$.

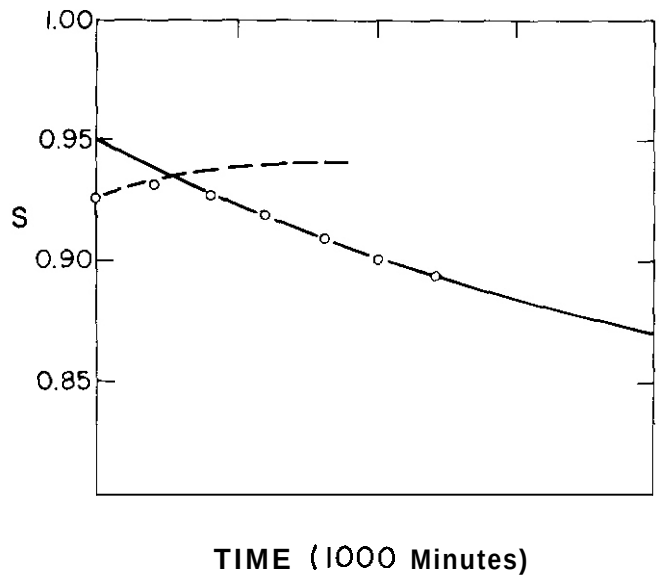

Fig. 8b - The change of order during fast neutron radiation of Cu_3Au at 150°C from Kirk and Blewitt[19] (points). The line represents the fit to the data using the E and K from Fig. 8a and $\rho_d = 1.7 \times 10^{13}/m^2$. Note the initial transient where the datum points deviate from the curve. For low dislocation densities the vacancies are removed primarily by recombination (dashed line). Under this assumption the initial transient can be fitted.

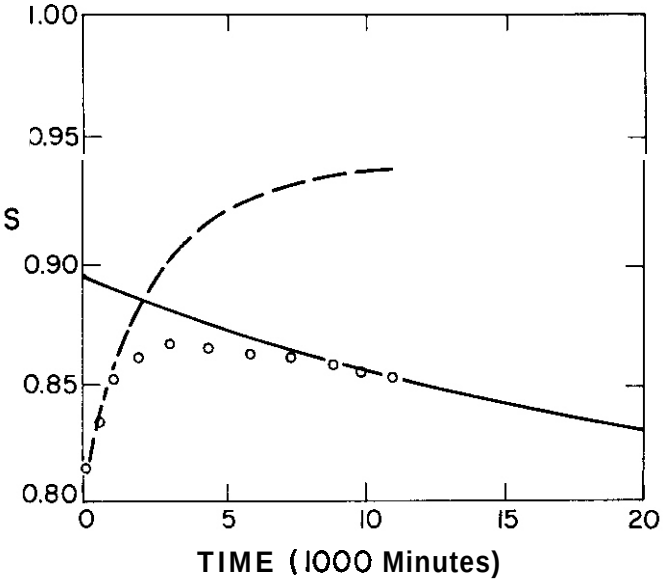

Fig. 8c - As for Fiq. 8b but for a lower initial order parameter and $\rho_d = 2.7 \times 10^{13}/m^2$ (solid line). Note again the recombination dominated curve (dashed line) fitting the initial **slope.**

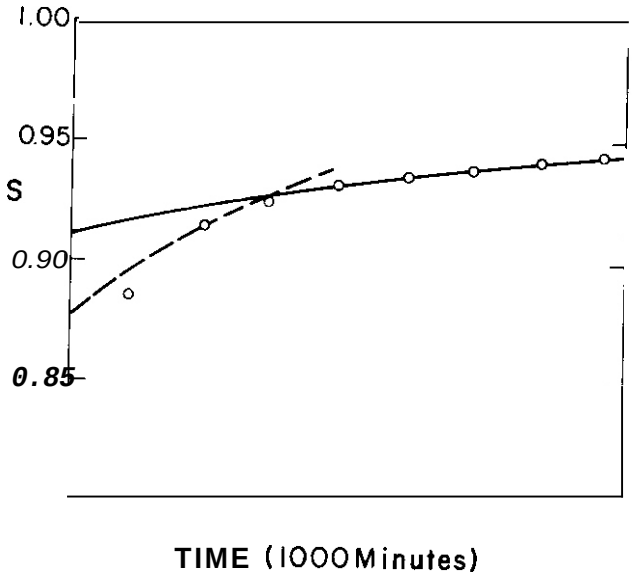

Fig. 8d - As for Fig. 8b but for thermal neutron irradiation (1975) at 135°C with ε = 20, K = 2.5 X 10^{-10} dpa/sec and ρ_d = 10^{12}/m2 (solid line) Note the recombination dominated curve (dashed line) only explains part of the transient.

the fast neutron irradiation rate of 2×10^{16} neutrons/m^2/sec gives a displacement rate of 1.4×10^{-9} dpa/sec. For the εK values taken from Fig. 8a this gives $\varepsilon = 80$.

With these values of εK the high temperature data can now be fitted. However, since no electron microscopy analysis of dislocation density is available we have no information with which to model how ρ_d varies with time. We, therefore, used constant values for this parameter. (There is no difficulty in accommodating a changing ρ_d in our model once such data becomes available.) Since most of the data covers only the early stages of irradiation (total dpa $\lesssim$ 0.01) and relatively low temperatures we anticipate that recombination will dominate early in the process when ρ_d is low but that intermediate values of ρ_d (10^{12} - $10^{16}/m^2$) will become influential later. The pre-exponents D_o in the diffusion coefficients D_{ov} and D_{oi} and the interstitial motion energy E_{im} were all taken from copper data.[22]

The vacancy motion energy was taken from the Cu_3Au literature[23-25] to lie in the range 0.8 - 1.1 eV. The energy of motion for an ordering jump was chosen to be slightly larger than E_m.

Determination of C_v also requires evaluation of the cascade loss fractions f_i and f_v for interstitials and vacancies, respectively. These are not well known but have been discussed by Wollenberger[26] who presents data supporting a value of $f_v = 0.7$ for copper under fast neutrons at low temperature (55-140°K). Kirk and Blewitt suggested a value of 0.95 from their experiment at 150°C. We take this latter value for f_v and f_i. The results are not sensitive to small changes in these parameters.

Figure 8b shows that using these parameters gives an excellent fit to Kirk and Blewitt's data after an initial transient was complete. These workers suggested that the transient may be due to very long free vacancy lifetimes in the early stages when the dislocation density was very low.

Under such conditions the vacancy concentration is controlled by the rate of recombination with interstitials. Fig. 8b demonstrates that by using a zero dislocation density the initial slope of the transient can be fitted. The vacancy lifetime under these conditions is ~250 s compared with the ~2 secs for the steady-state with a dislocation density of $2 \times 10^{13}/m^2$. Thus, although the same number of vacancies are produced in each case, the vacancy concentration and hence the ordering rate is much greater for the low dislocation situation.

The dislocations do not become a significant sink until ρ_d reaches $\sim 10^{11}/m^2$ so that similar curves are obtained to the one shown in Fig. 8b (dashed line), up to this dislocation density.

The length of the transient is a measure of the time needed far the dislocations to dominate as sinks. It is clear that ρ_d is changing much more slowly than the order parameters. (This is why one can speak meaningfully of a steady-state order even when the dislocation density is varying.) In fact, the dislocation density will steadily increase[27] and saturate after several dpa. In contrast order steady-state is reached after ~0.01 dpa. This implies that our so-called steady-state order will change somewhat with the dislocation density, tending to drift slowly lower with very long irradiation times.

This suggestion for the transient also explains why it has a larger magnitude for specimens with lower order (Fig. 8b). In such specimens the vacancies during their extended lifetime at the beginning of reaction meet more wrong atoms than in more highly ordered samples. All this is automatically accounted for in the model.

For the thermal neutron flux no low temperature data was available so that εK was chosen to fit the experimental data. The other parameters, however, are fixed from the fast neutron fit and were not changed. The curve was fitted successfully as shown in Figure 7c, by using $\varepsilon = 20$ and

$K = 2.5 \times 10^{-10}$ dpa/s. Taking cross sections for the (n,γ) reaction of 98 barns and 4.4 barns for gold and copper, respectively, and a given flux of 2×10^{16} neutrons/m^2/sec, we obtain $K \sim 10^{-10}$ dpa/s in reasonable agreement with our fitting parameter.

Note that in this case we have very small cascades, the component defects of which may be well separated if a replacement collision sequence occurs. To fit the data we required a vacancy survival rate of 100%, indicating that such sequences are quite common.

With the aid of our fitted line it is now clear that this data contains a transient also, no doubt for the same reason as before. Fig. 8c includes the low dislocation density result which in this case only explains part of the transient. A closer fit could be obtained by using a smaller value for E and a correspondingly higher K. However, this would deviate from the calculated K and the E value determined by Kirk and Blewitt.[19] If these values are reliable the results suggest that a further explanation is required for the remaining transient for thermal neutrons.

The predominance of long replacement collision sequences (implied by the high vacancy survival rate) for thermal neutrons indicates that the disorder in the early stages consists primarily of such sequences. Since each faulted row can be easily ordered by one vacancy moving along it, it is probable that the ordering rate will be increased initially, until overlap of sequences occurs. This is the probable explanation of the remaining transient.

In the fast neutron case where most replacements occur in the cascade, the disordered region is three-dimensional. Only the wrong atoms on the outermost layer of the disordered region are adjacent to the matrix which is defining the loop range order of the sites. Only in this outer layer will vacancies be able to re-order with anything like the high efficiency of vacancies moving along replacement collision sequence

traces. Since our simple model makes no allowance for such differences in the distributions of wrong atoms there will be part of the transient that cannot be fitted in the thermal neutron (high vacancy efficiency) case. As radiation proceeds overlap of collision sequences will increase the three-dimensional nature of disordered regions. The ordering effectiveness of vacancies will then approach the fast neutron case.

The remaining data for irradiation of Cu_3Au in the literature is much older and reactor dosimetry was less complete. Sufficient details of the nature and magnitude of the fluxes are, therefore, lacking. However, we were able to fit all these data successfully with our model using the same defect parameters established above. The only parameters changed were ρ_d and K.

Figure 9 shows our fit to the data of Cook and Cushing.[17] It is important that the values of E_f and E_m^o give the correct temperature variation since this data is taken at a temperature 100°C below that of Kirk and Blewitt.[19] The irradiation rate used by Cook and Cushing was estimated at 4×10^{16} neutrons/m^2/sec (3×10^{-9} dpa/s). These workers observed similar resistivity curves at 106°C and 35°C. These translate to the different order curves shown in Figure 9.

These curves were successfully fitted with the identical diffusional parameters to those in Fig. 8b, indicating that E_f and E_m^o correctly predict the temperature variation from 35°C-150°C. These data extend to twelve times the dpa of the data in Fig. 8b. It is, therefore, not surprising that we find a higher dislocation density necessary to fit the curve. No transient is visible in these curves, presumably due to the lower temperature.

Figure 10 shows our fits to the thermal neutron data of Glick, et al.[28] and fast neutron data of Siegel.[29] We emphasize that once again the only parameter changes involve ρ_d and K which take the values shown in the figure. Once again a very satisfactory fit is obtained.

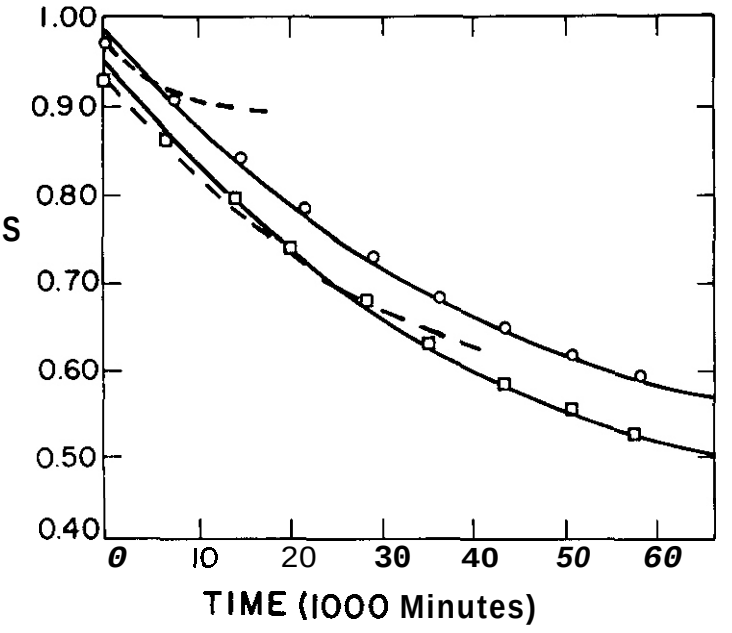

Fig. 9 - The data of Cook and Cushing[17] for fast neutron irradiation at 35°C and 106°C. The points are fitted with the curves shown using $K = 3 \times 10^{-9}$ dpa/sec and $\rho_d = 2.5 \times 10^{14}/m^2$ at 106°C (upper curve) and 35°C (lower curve).

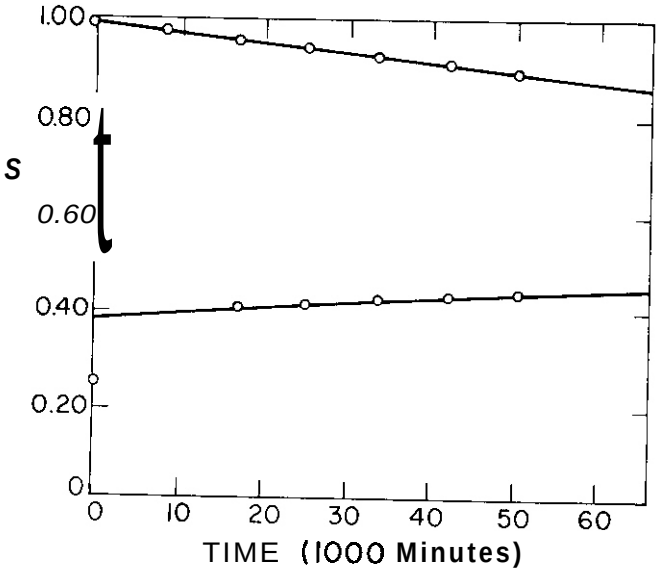

Fig. 10a - Order/disorder change under thermal neutron irradiation at 80°C measured by Glick et al.,[28] fitted using $K = 2 \times 10^{-9}$ dpa/sec and $\rho_d = 1.5 \times 10^{16}/m^2$. Note the very low value of S for the low curve.

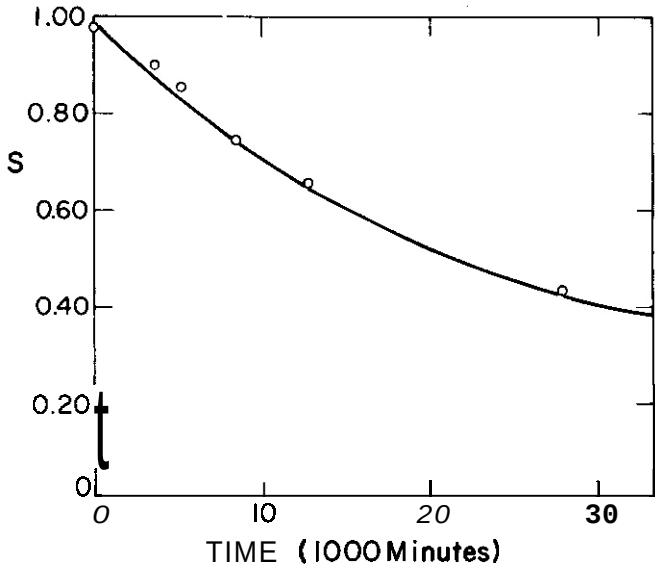

Fig. 10b - The fast neutron data of Siegel[29] at 40°C, fitted using $K = 8 \times 10^{-9}$ and $\rho_d = 8 \times 10^{14}/m^2$.

In Figure 10a, the data of Glick[28] during irradiation of an initially ordered and an initially disordered sample with thermal neutrons are shown. The ordered data can be fitted accurately with the same diffusional parameters as before. For the initially disordered sample, the data can be fitted except for the initial transient. The explanation for the transient is presumably similar to that given in the discussion for thermal neutron data above (Fig. 8c). However, the very low value of S probably means that a small domain size exists in the sample and a short range order model should really be used for the data.

Finally, Fig. 10b shows the fitting to the fast neutron data of Siegel.[29] Once again, the same diffusional parameters are used, indicating that the E_m and E_m^o values correctly predict the temperature variation.

Figures 8-10 contain only very small initial transients as compared to Fig. 7. The former were for data at a much lower temperature however. This has little effect on interstitial mobility so that vacancy lifetime is not affected much. (Vacancies are effectively stationary compared with interstitials at all these temperatures.) On the other hand, since the vacancy jump frequency is greatly reduced at the lower temperatures, the number of ordering jumps made by a vacancy is greatly reduced at the lower temperatures. As Figures 8-10 show the resulting differences between the curve for recombination only and the curve for higher dislocation density are much closer than in Fig. 7. As vacancies become less mobile at lower temperatures, recombination becomes more important than flow to dislocations even for high dislocation densities. The initial transients then become negligible.

5. Discussion

The successful fitting of such a varied collection of date with similar parameters in a straightforward phenomenological model is remarkable. It should not be thought that this is because the curves can be

fitted with a wide range of different parameter combinations. In fact the choice of the key parameters is very narrowly restricted.

The ordering energy V_o is fixed by the requirement of matching the thermal equilibrium order at low and intermediate temperatures. The multiple εK is fixed by the low temperature experiments. The diffusional parameters are not well known (D_{ov}, D_{oi}, E_{im}, E_v^o, E_{vf}, ν). The interstitial diffusion however must be rapid at these temperatures which implies that the exact value of motion energy E_{im} is less important than the fact that it is small. D_{ov} and ν can be adjusted to compensate for a change in vacancy motion energy E_m and hence it is possible to match the same data at a given temperature with various combinations. However, it is impossible to match the data at different temperatures in this way. In fact the strong temperature variation very closely limits the values of E_m and E_m^o to those given in Table 1. However, it is possible to decrease E_m and simultaneously increase E_m^o in such a way that the quality of fit only decreases slowly. From the current data therefore we can only fix their combination precisely. The current values are accurate to ±0.05 eV, but the combination is better than that. However, with more data at steady-state it should be possible to fix these energies very precisely since the shape of the predicted S_∞ versus temperature curve varies strongly with such changes. Since the same parameters used for the time dependent curves were used to determine the steady-state order curves of Fig. 4, we believe that the latter gives an accurate prediction. The only remaining variation is the slow change in the dislocation density as radiation proceeds. The next step in our theory will model such a changing dislocation density and its effects.

From the point of view of our model the current data is very incomplete. An ideal experiment would be to irradiate Cu_3Au for longer times at a wide range of temperatures. Each flux should also be used at low temperatures (below room temperature) to determine εK. It is essential that all experiments begin with large domain size and a well

defined order parameter. The dislocation density variation should be monitored also. With this information our model could be tested much more completely. The results so far suggest that these experiments could provide accurate data for point defect behavior in Cu_3Au and detailed information on cascades as a function of temperature.

There is an urgent need for an experimental test of Muto's[15] model relating resistivity and the long range order parameter.

We note also that radiation is a very useful tool in the study of order/disorder reactions. The enhanced ordering rate could well be used to produce more completely ordered materials at lower temperatures where the thermal reaction is too slow to go to completion. In addition, lower values of S can be obtained by low temperature irradiations than can be obtained by thermal treatments. This will permit the study of ordered alloys over a much wider range of S than has been used hitherto.

6. Conclusions

a) The radiation disorder model has been shown to successfully fit all available long time data for fast and thermal neutron irradiations of Cu_3Au.

b) The parameters critical to the fitting are:

E_m = 0.84 for vacancy motion
E_m^o = 0.84 eV for ordering vacancy jumps

The ratio of replacements to displacements, ϵ, is 80 for fast neutrons and 20 for thermal neutrons. For the former a survival rate for free vacancy production is 5%, for the latter it is 100%.

c) Initial transients occur in which the ordering rate is much greater. These are explained by the longer lifetime for vacancies at

early times when recombination alone controls the vacancy concentration.

d) Prediction for steady-state conditions have been made and their variation has been shown to be physically reasonable.

e) Interpretations of experiments which measure ordering rates and obtain activation energies directly from them are not reliable and this model should be used instead.

Acknowledgements

We are grateful for helpful discussions of this work with Dr. M. Guinan of Lawrence Livermore Laboratory and Drs. T. Blewitt and M. A. Kirk from Argonne National Laboratory. One of us (PW) is grateful for support from the Office of Fusion Energy, U. S. Department of Energy through Lawrence Livermore Laboratory which enabled some of the computational work to proceed.

VI. REFERENCES

1. K. R. Russell, Jnl. Nuclear Matls. 83, 176 (1979).

2. P. Wilkes, Jnl. Nuclear Matls. 83, 166 (1979).

3. K-Y. Liou and P. Wilkes, Jnl. Nuclear Matls. (in press).

4. E. M. Schulson, Jnl. Nuclear Matls. 83, 239 (1979).

5. M. L. Jenkins, M. Wilkens, Phil. Mag. 34, 1155 (1976).

6. W. L. Bragg and E. J. Williams, Proc. Roy. Soc., A145, 699 (1934).

7. L. R. Aronin, "Effect of Nuclear Radiation on the Structure and Properties of Metals and Alloys," Jnl. App. Phys. 25, 344 (1954).

8. V. S. Polenok, Fiz. Met. Metalloved 36, 195 (1973).

9. G. J. Dienes, Acta Met. 3, 549 (1955).

10. D. R. Chipman, Jnl. Appl. Phys. 27, P739 (1956).

11. J. Gilbert, H. Herman, A. C. Damask, Rad. Eff. 20, P37 (1973).

12. A. Brailsford, R. Bullough, Jnl. Nuclear Matls. 44, P121 (1972).

13. G. Oleownick, W. Schule, Fundamental Aspects of Radiation Damage in Metals, Vol. 1, NTIS, U. S. Department of Commerce, Springfield, VA, P341 (1975).

14. A. C. Hindmarsh, J. D. Byrne, Numerical Methods for Differential Systems, L. Lapidus anti W. E. Scheisser, eds., Academic Press, 147 (1976).

15. R. Muto, Inst. Phys. Chem. Res. Sci. Paper (Tokyo), 20, 99 (1936)

16. R. Landauer, Jnl. Appl. Phys 23, 779 (1952).

17. L. G. Cook and R. L. Cushing, Acta Met. 1, 539 (1953).

18. E. Passaglia and W. F. Love, Phys. Rev. 98, 1006, (1955).

19. M. A. Kirk and T. H. Blewitt, Met. Trans. 9A, 1729 (1978).

20. T. H. Blewitt, private communication.

21. D. T. Keating and B. E. Warren, Jnl. App. Phys. 22, 286 (1951).

22. N. L. Peterson, Jnl. Nuclear Matls. 69 & 70, P3 (1978).

23. S. Takainura and S. Okuda, Rad. Eff. 17, 151 (1973).

24. R. Feder, M. ilooney, anti A. S. Nowick, Acta Met. 6, 265 (1958).

25. R. A. Dugdale, Phil. Mag. 1, 537 (1956).

26. H. Wollenberger and U. Theis, to be published in Jnl. of Nuclear Matls.

27. W. G. Wolfer, Int. Conf. on Fundamental Mechanisms of Radiation Induced Creep and Growth, Chalk River, Canada, (1979).

28. H. Glick, F. C. Brooks, W. G. Witzig, and W. E. Johnson, Phys. Rev. 87, 1075 (1952).

29. S. Seigel, Phys. Rev, 75, 1823 (1949)

VII. Future Work

The next step in this work will be to model the changing dislocation density in the early stages of irradiation.

VIII. Publications

This paper has been submitted to Philosophical Magazine.

I. PROGRAM

Title: Effects of Irradiation on Fusion Reactor Materials
Principal Investigators: F. V. Nolfi, Jr. and A. P. L. Turner
Affiliation: Argonne National Laboratory

II. OBJECTIVE

The objective of this work is to determine the microstructural evolution, during irradiation, of first-wall materials with special emphasis on the effects of helium production, displacement damage and rates, and temperature.

III. RELEVANT DAFS PROGRAM PLAN TASK/SUBTASK

SUBTASK II.C.2.1 Mobility, Distribution, and Bubble Nucleation

IV. SUMMARY

The temperature dependence of void swelling in 316 stainless steel preinjected with helium and irradiated with Ni^+ ions, or irradiated simultaneously with Ni^+ ions and He^+ ions, has been measured by TEM. A bimodal cavity distribution was found for dual-ion irradiated samples, but not in preinjected single-ion irradiated samples. For both types of irradiation a swelling peak was found at 650°C as a result of a sharp peak in cavity number density at this temperature. A second, larger swelling peak due to a peak in cavity size occured at 600°C for dual-ion irradiation.

V. ACCOMPLISHMENTS AND STATUS

A. Temperature Dependence of Swelling in Single and Dual-Ion Irradiated 316 Stainless Steel -- G. Ayrault and M. A. Hoff

1. Introduction

A major question in the irradiation response of candidate fusion reactor structural materials is the influence of concurrent displacement damage and helium production. Dual-ion irradiation, using heavy-ions for damage production and helium ions to simulate gas production by transmutation events provides a means of investigating such effects in the absence of a high energy neutron source.

This report presents preliminary results on the temperature dependence of swelling in single and dual-ion irradiated 316 stainless steel. Dose and helium injection rate dependences of swelling will be determined in future stages of the program.

2. Irradiation Conditions

Type 316 stainless steel samples from the MFE heat were 50% cold-worked, then solution annealed at 1050°C for 0.5h and aged at 800°C for 10h. One set of samples was simultaneously irradiated with 3.0 MeV Ni^+ and 0.87 MeV degraded $^3He^+$ in the ANL Dual-Ion Irradiation Facility; the helium injection rate was 15:1 appm He:dpa. A second set of samples was preinjected at room temperature with 5 appm ^3He, and single-ion irradiated with 3.0 MeV Ni^+. For both sets the dose level was 12 dpa. The nominal irradiation temperatures were 550, 600, 625, 650 and 700°C; surface temperatures of all samples were measured with an infrared pyrometer during irradiation. After irradiation, the samples were electrochemically sectioned to a depth of 45008 (peak damage is at 5500Å), and backthinned for TEM inspection.

3. Precipitates

Most of the irradiated samples contained both cavities and intragranular precipitates, which were not present in unirradiated control samples with the same thermal history. In addition, the cavities were

coated with precipitates in all samples where cavities were found; examples of this are shown in Fig. 1.

4. Swelling in Dual-Ion Irradiated Samples

For dual-ion irradiation in the temperature range 550 to 650°C, a bimodal cavity-size distribution was found, Fig. 2a-e; at 700°C, only small cavities were observed, Fig. 2f. Large cavities were usually associated with the intragranular precipitates, while the small cavities were found on both precipitates and dislocations.

Void number densities, mean void size and void volume were determined from the TEM micrographs. The data are presented in Figs. 3, 4 and 5. Each data point is based on observations in at least three different regions of the sample; the error bars reflect variations between these regions. In numerical data analyses, the small and large cavities in the bimodal distribution were treated separately, and the cavity number density and size are plotted separately in Figs. 3 and 4. For void volume, Fig. 5, the two contributions have been summed, but when large cavities are present, they account for nearly all of the volume.

The most striking feature of these data is the sharp peak in swelling for the sample irradiated at 603°C. The large volume change was due to the large cavities of irregular shape shown in Fig. 2c. Stereo observations showed that many of these cavities were entirely contained in the foil, and dark-field images of the precipitate coating on cavity surfaces exactly reproduced the shapes seen in bright-field images (Fig. 1a, b) clearly indicating that they are truly voids and not etching artifacts associated with the surface. This swelling peak is, however, associated with considerable variations in $\Delta V/V$ from point to point in the sample. Four different areas gave volume changes ranging from 2-6%. The high swelling in this sample was not reproduced in a nominally identical sample, Fig. 2b, irradiated at 595°C. The reasons for these large regional and sample to sample variations are not clear at present.

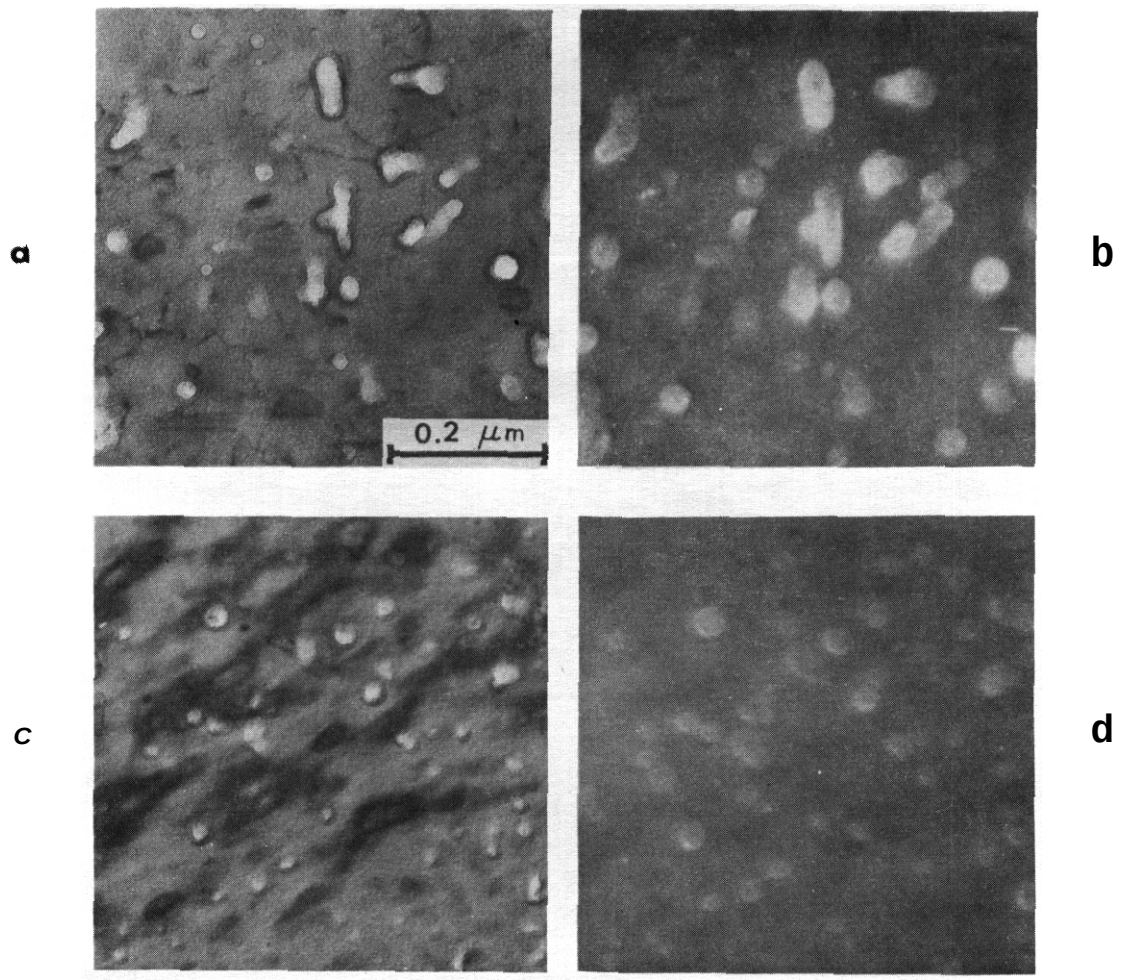

Figure 1. Bright-field dark-field pairs showing precipitate-coated cavities in preinjected single-ion and dual-ion irradiated 316 stainless steel (Dose = 12 dpa, dose rate = 3 x 10^{-3} dpa·s^{-1}) (a) 603°C dual-ion, (b) dark-field of same region as (a), (c) 650°C preinjected single-ion, (d) dark-field of same region as (c).

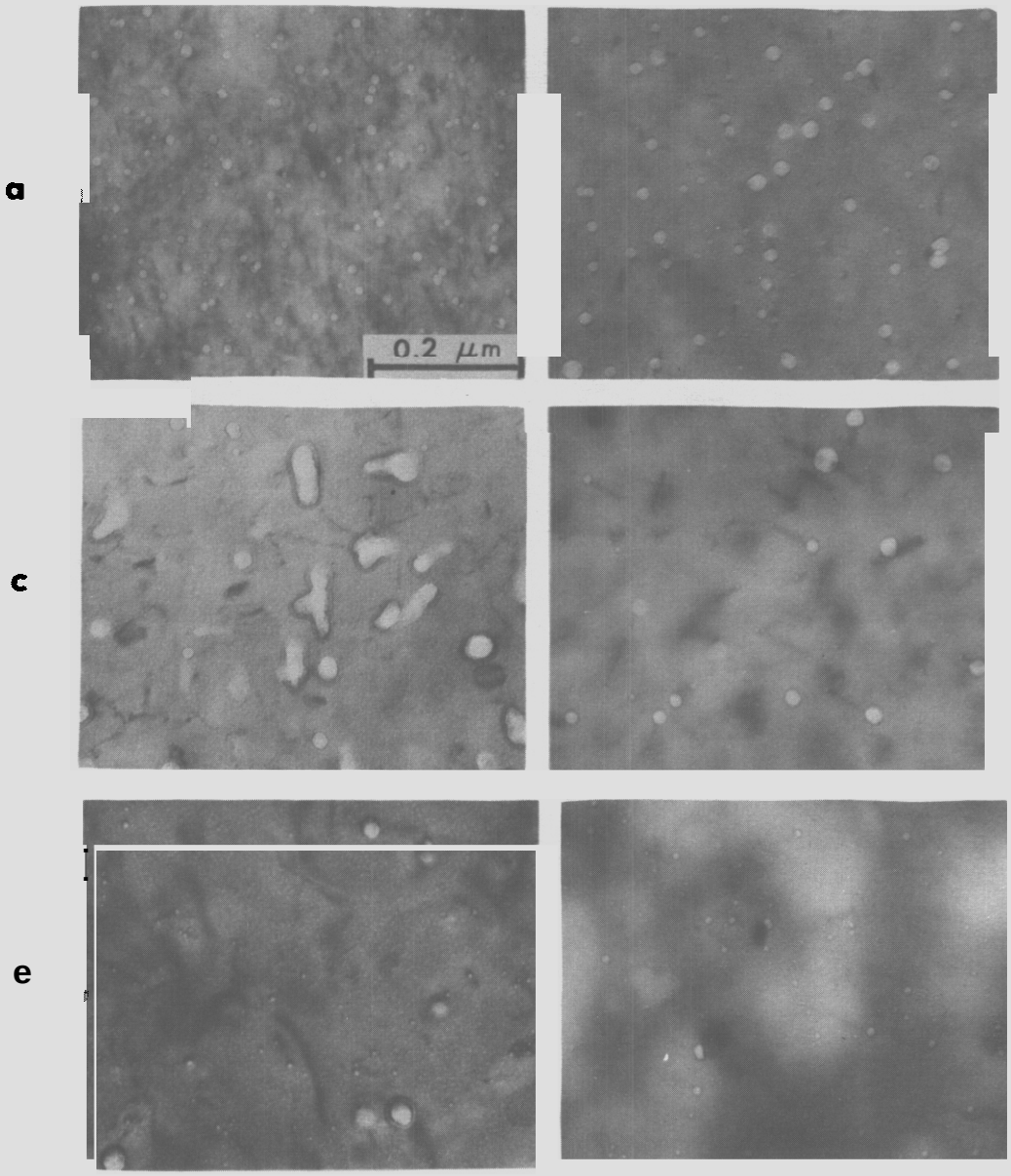

Figure 2. Absorption contrast micrographs of dual-ion irradiated 316 stainless steel (Jose = 12 dpa, dose rate = 3 x 10^{-3} dpa·s^{-1}, helium injection rate = 15:1 appm He:dpa). (a) 540°C, (b) 595°C, (c) 603°C, (d) 633°C, (e) 650°C, and (f) 700°C.

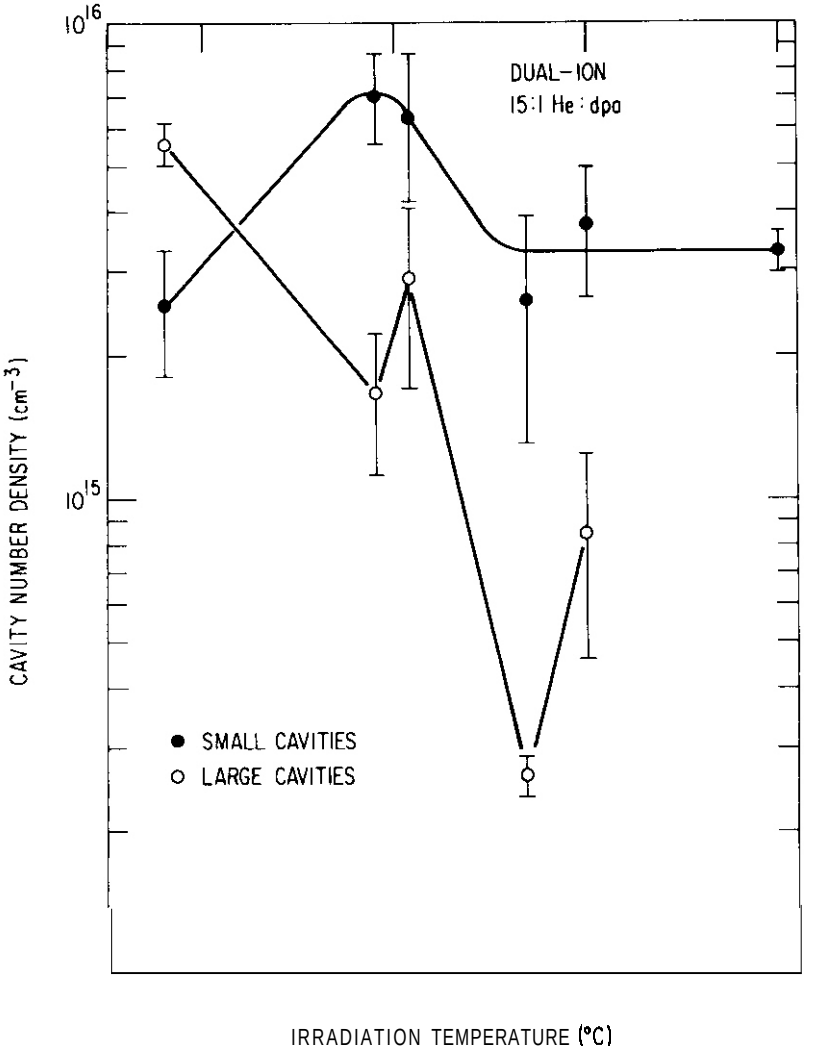

Figure 3. Temperature dependence of cavity number density in dual-ion irradiated 316 stainless steel (dose = 12 dpa, dose rate = $3 \times 10^{-3} dpa \cdot s^{-1}$). The densities of small and large cavities in the bimodal size distributions are plotted separately.

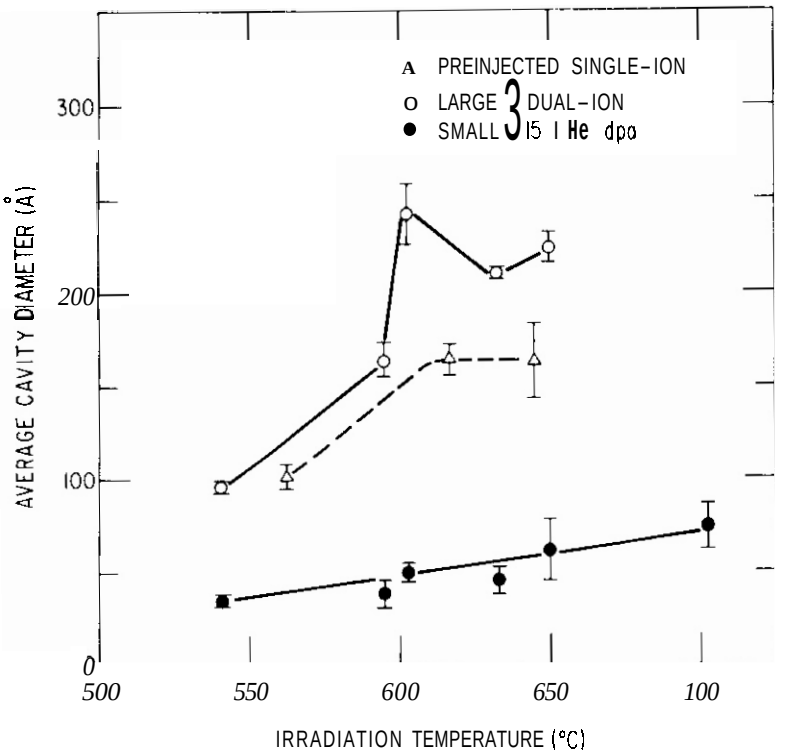

Figure 4. Temperature dependence of cavity size in dual-ion and pre-injected single-ion irradiated 316 stainless steel (dose = 12 dpa, dose rate = 3 x 10^{-3}dpa·s^{-1}). Small and large cavity sizes are plotted separately for the bimodal size distributions found in dual-ion irradated samples.

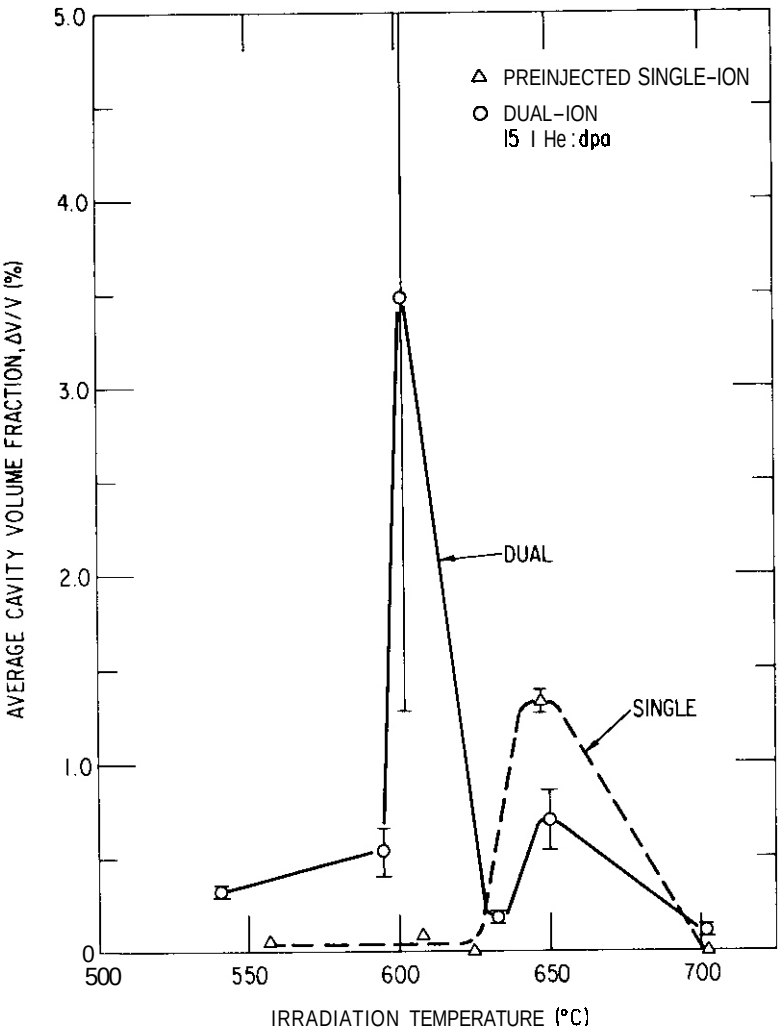

Figure 5. Temperature dependence of swelling in dual-ion and preinjected single-ion irradiated 316 stainless steel (dose = 12 dpa, dose rate = 3 x 10^{-3}dpa·s^{-1}).

A second peak in the swelling curve is found at 650°C. This peak is also out of the ordinary in that a swelling increase with temperature usually results from an increase in cavity size, but this peak is due primarily to a sharp rise in number density. Although duplicate dual-ion samples have not yet been inspected for this irradiation temperature we have confidence that the behavior is reproducible because it was repeated even more dramatically in the preinjected single-ion irradiations (see Fig. 6).

5. Swelling in Single-Ion Irradiated Samples

In the preinjected and single-ion irradiated samples, the cavity size distributions were not bimodal, and rapid swelling near 600°C was not observed. However the swelling peak at 650°C resulting from a peak in void number density was also observed for the single-ion irradiations. No cavities were observed in the 625 and 700°C sample and it is interesting to note that unlike all other irradiated samples, no intragranular precipitates were observed either. This suggests a relationship between precipitation and cavity formation. but does not explain the absence of both.

VII. FUTURE WORK

The unusual swelling behavior found in the samples examined to date requires that the consistancy of the behavior be checked on duplicate samples that are available. Additional samples have been irradiated at 575 and 675°C to give smaller temperature steps; these will be examined in the near future. Data on the effects of dose and helium injection rate currently being collected should give further insight to the behavior that has already been observed. Breakaway swelling at a critical dose or extreme sensitivity to helium injection rate could explain some of the variability observed. Further insight will be sought through investigation of irradiation induced or enhanced precipitation.

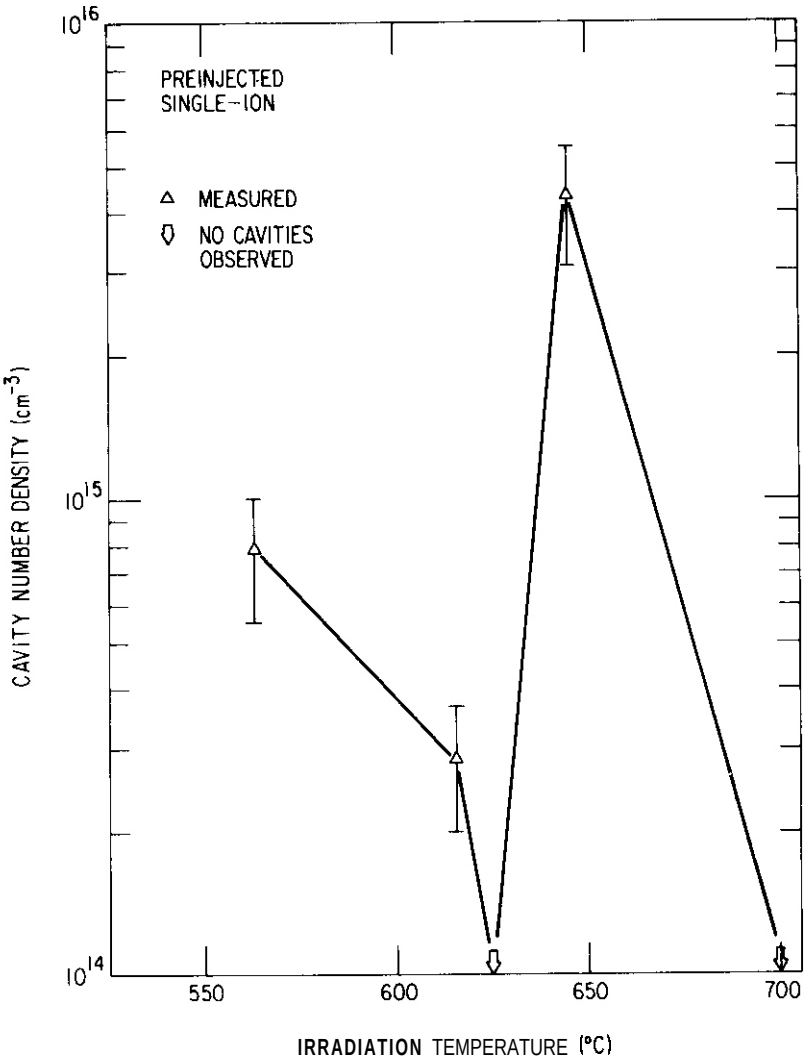

Figure 6. Temperature dependence of cavity number density in preinjected single-ion irradiated 316 stainless steel (dose = 12 dpa, dose rate = 3×10^{-3} dpa·s^{-1}).

I. PROGRAM

Title: Irradiation Effects Analysis (WHOTI/EDA)
Principal Investigator: 3. G. Doran
Affiliation: Hanford Engineering Development Laboratory

II OBJECTIVE

The objective of this work is to assess the effects of cyclic variations in irradiation, stress, and temperature on the evolution of the damage microstructure to enable the projection of steady-state irradiation data to cyclic conditions.

III. RELEVANT DAFS PROGRAM PLAN TASK/SUBTASK

II.C.5 Effects of Cycling on Microstructure

IV. SUMMARY

A computer model developed previously to simulate microstructure evolution during cyclical irradiation neglected the transients in defect concentrations at the beginning and end of each pulse. The model was refined to include approximations for this transient behavior. The effects of damage rate, irradiation temperature, and cycle period (50% duty factor) on void size, void concentration, and swelling are discussed. The revised model is more consistent with experimental observations than was the old model. Like the old model, it predicts a more pronounced sensitivity of microstructure evolution to displacement rate and temperature in cyclic irradiations than in steady irradiations.

V. ACCOMPLISHMENTS AND STATUS

A. The Effect of Pulsed Irradiation on Microstructure Evolution -- D. L. Greenslade and R. W. Powell (HEDL)

1. Introduction

A previous paper[1]) discussed a model to predict microstructure evolution during pulsed (HVEM) irradiation. The model assumed a square wave defect concentration in phase with the cyclical displacement rate. During the "beam on" condition, the defect (single vacancy or interstitial) concentrations were set equal to their steady state values. During the "beam off" condition, thermal equilibrium concentrations were used. This model did not agree with all of the results of a companion experimental study.

The purpose of this work was to incorporate transients in defect concentrations into the model anti to study the effects of peak damage rate, irradiation temperature, and cycle period. Irradiation parameter ranges examined were peak damage rates of 0.5×10^{-3} to 2×10^{-3} dpa/s, irradiation temperatures of $550 \pm 10°C$, and cycle periods of 100 to 1000s whereby the pulse duration was long compared to the lifetime of a vacancy. Unlike the earlier work, throttling (reduction of the void nucleation rate due to the annealing of sub-critical vacancy clusters between pulses) was not included.

2. Model Revisions

This work included verification of the validity of certain assumptions made in characterizing the transient defect concentrations. The approximations that were used greatly simplified calculations and thus reduced computer time. Typical defect concentration profiles during an irradiation cycle for both models are shown in Figure 1.

TS signifies the time for the interstitials to equilibrate with the dislocation structure and can be approximated by

$$TS \sim \frac{1}{D_i K_i^2} \qquad [1]$$

where D_i = interstitial diffusivity, and K_i = interstitial sink strength.

τ denotes the vacancy decay time and is approximated by

$$\tau \sim \frac{1}{D_v K_v^2} \ln \frac{C_v^{ss}}{C_v^{th}} \qquad [2]$$

where D_v = vacancy diffusivity, K_v = vacancy sink strength, C_v^{ss} = steady state (during "beam on") vacancy concentration, and C_v^{th} = thermal equilibrium vacancy concentration.

To calculate the transient defect concentrations, rate equations based upon the conservation of point defects were used. The two simultaneous, nonlinear, first-order differential equations describing the time rate of change of defect concentrations are

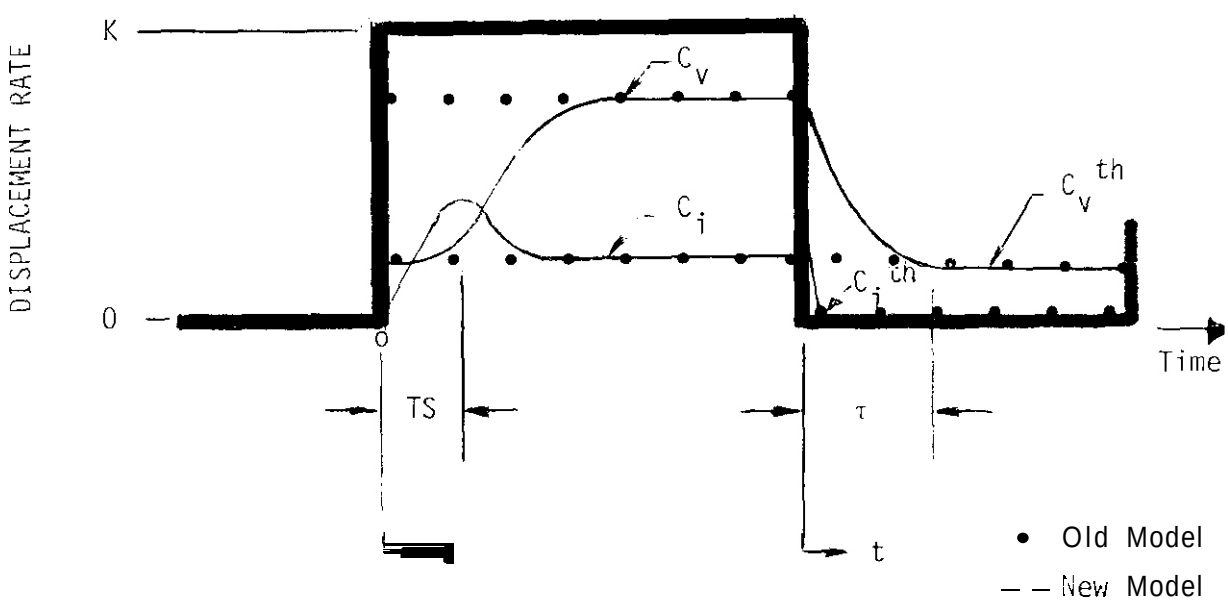

FIGURE 1. Typical Vacancy and Interstitial Concentration Profiles During an Irradiation Cycle (exaggerated to show details).

$$C_v = K + K_e - a\, C_i C_v - D_v K_v^2\, C_v \qquad [3]$$

$$C_i = K \qquad - a\, C_i C_v - D_i K_i^2\, C_i \qquad [4]$$

where C_v, C_i = vacancy and interstitial concentrations, respectively;
K_v, K_i = vacancy and interstitial sink strengths, respectively;
K = displacement rate;
K_e = thermal emission rate;
a = recombination constant;
D_v, D_i = vacancy and interstitial diffusivities, respectively.

Note that equations [3] and [4] are coupled by the recombination term.

To evaluate C_i and C_v as functions of time, certain simplifying assumptions were made. These are shown in Table 1. These approximations were then compared with the "exact" solution of the system which was obtained using a time consuming numerical method. Figures 2 and 3 justify the use of the approximations.

All the expressions listed in Table 1 which describe the defect concentrations during the irradiation cycle were then incorporated in the earlier computer model. Time steps were carefully altered so that the entire defect concentration profile was utilized in the microstructure model.

3. Review of Earlier Results

It is worthwhile to review the experimental observations[11] and the predictions of the earlier model. The experimental results of pulsed HVEM irradiation of a simple Fe-Ni-Cr alloy at 600°C were:

(1) the swelling rate decreased compared to steady irradiation,

(2) the swelling rate decreased as the cycle period was increased from 2.5 to 60 seconds,

(3) the average void size decreased while the void concentration increased as compared to steady irradiation.

TABLE 1

DEFECT CONCENTRATION EXPRESSIONS USED IN THE CURRENT COMPUTER MODEL

VALID TIME RANGE	EXPRESSION	ASSUMPTION (S)
Beam On Condition		
$0 < t < TS$	$C_i = \frac{K}{D_i K_i^2}\left(1 - e^{-D_i K_i^2 t}\right)$	No recombination
$TS < t < TSS^{\dagger}$	$C_i = \frac{K}{\alpha C_v^* + D_i K_i^2}$	$\dot{C}_i \approx 0$
$t > TSS$	$C_i = \frac{D_v K_v^2\left[-(1+\mu) + \sqrt{(1+\mu)^2 + \xi}\right]}{2\alpha}$	$C_i = C_v = 0$
	where $\mu = \frac{K_e \alpha}{D_i D_v K_i^2 K_v^2}$, $\xi = \frac{4\alpha K}{D_i D_v K_i^2 K_v^2}$	
$0 < t < TSS$	$C_v^* = \left\{ -1 + \sqrt{1 + \frac{2\alpha}{D_i K_i^2}\left(Kt + \frac{\alpha C_v^{th}}{2D_i K_i^2} + C_v^{th}\right)} \right\} \frac{D_i K_i^2}{\alpha}$	$\dot{C}_i \approx 0$
$t > TSS$	$C_v = \frac{D_i K_i^2\left[-(1-\mu) + \sqrt{(1+\mu)^2 + \xi}\right]}{2\alpha}$	$\dot{C}_i = \dot{C}_v = 0$
Beam Off Condition		
$t' > 0$	$C_i \approx 0$	No recombination
$t' > 0$	$C_v = \frac{K_e}{D_v K_v^2}\left(1 - e^{-D_v K_v^2 t}\right) + C_v^{ss} e^{-D_v K_v^2 t}$	$C_i \approx 0$

† TSS = time for defect concentrations to reach steady state.

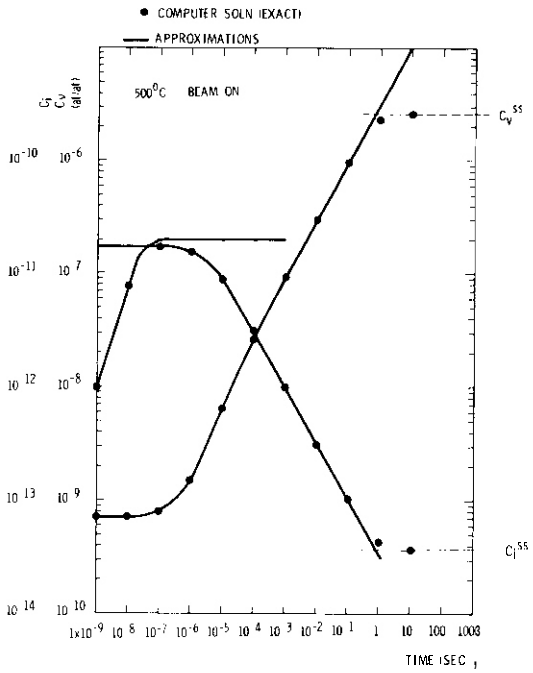

FIGURE 2. Defect Concentration Profiles During Initial Transient.

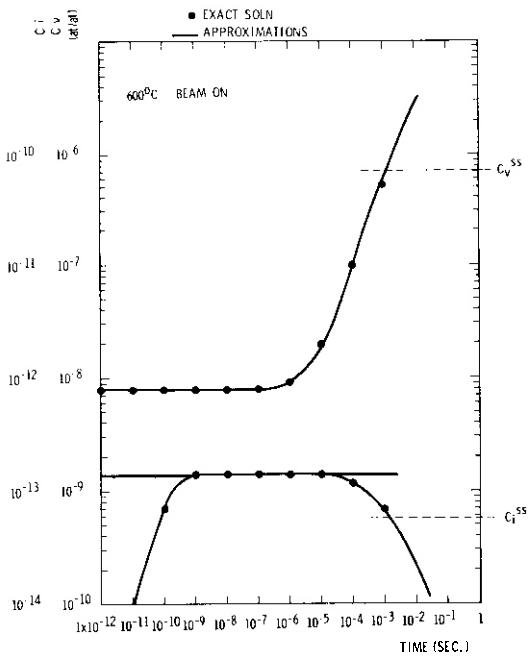

FIGURE 3. Defect Concentration Profiles During Initial Transient.

The earlier computer model, which introduced throttling of void nucleation, predicted that:

(1) the swelling rate should decrease compared to steady irradiation,

(2) the swelling rate should increase with increasing cycle period for the range of periods investigated experimentally,

(3) the void concentration should decrease compared to steady irradiation.

In the absence of throttling, the differences found between pulsed and steady irradiation were very small.

4. Parameter Study with Current Model

The effects of varying such parameters as the irradiation temperature, damage rate, and pulse period on the fluence dependence of void size, void concentration, and swelling are shown in Figures 4 through 15. Note that Figures 5, 8, and 11 show the differences between the old and new models due to changes in defect concentration characterization only; throttling was omitted from the old model in these cases.

The results can be summarized as follows (T_c refers to the critical cycle period below which no voids form, e.g., about 200 seconds at 560°C for the parameters used in this work; T_c increases with increasing temperature):

a. Effects on average void diameter ($\bar{d}_v$)

(1) $\bar{d}_v$ is greater than the steady irradiation value for periods greater than T_c.

(2) $\bar{d}_v$ increases as the period decreases to T_c.

(3) $\bar{d}_v$ increases for both steady and pulsed irradiation as temperature increases.

(4) $\bar{d}_v$ decreases as the damage rate increases (or, equivalently, as the number of cycles decreases).

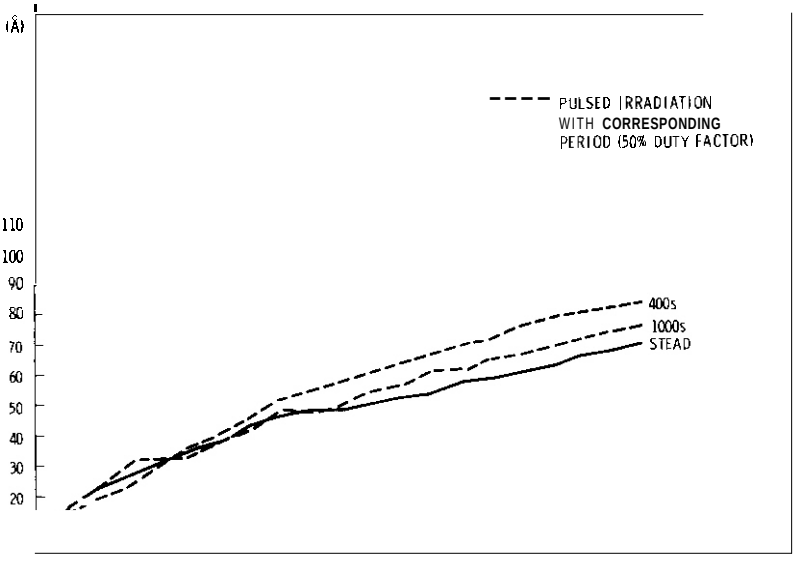

FIGURE 4. Fluence Dependence of Void Growth for Several Pulse Periods at 540°C.

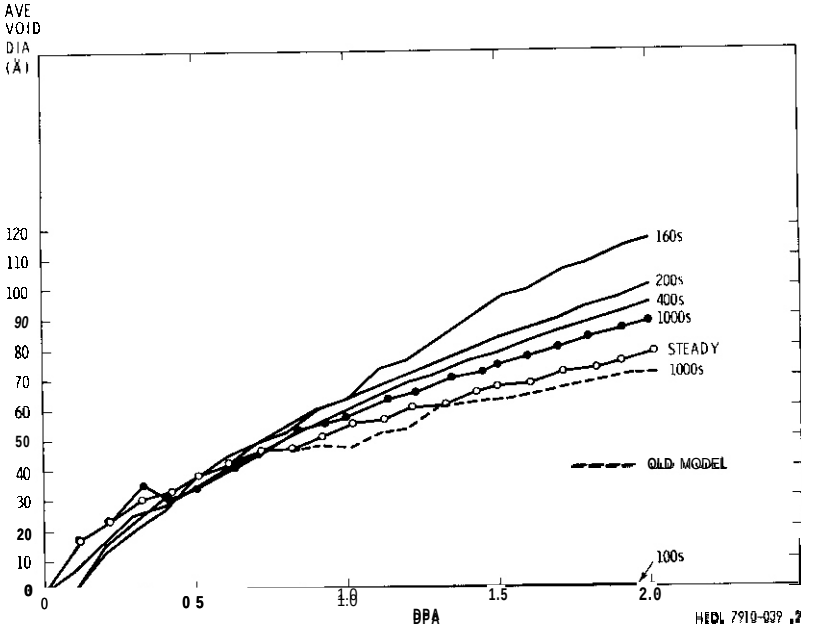

FIGURE 5. Fluence Dependence of Void Growth for Several Pulse Periods at 550°C.

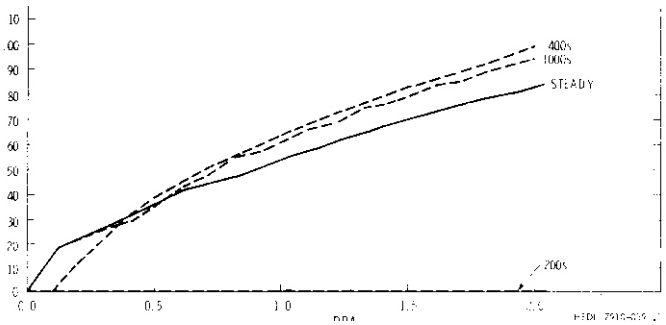

FIGURE 6. Fluence Dependence of Void Growth for Several Pulse Periods at 560°C.

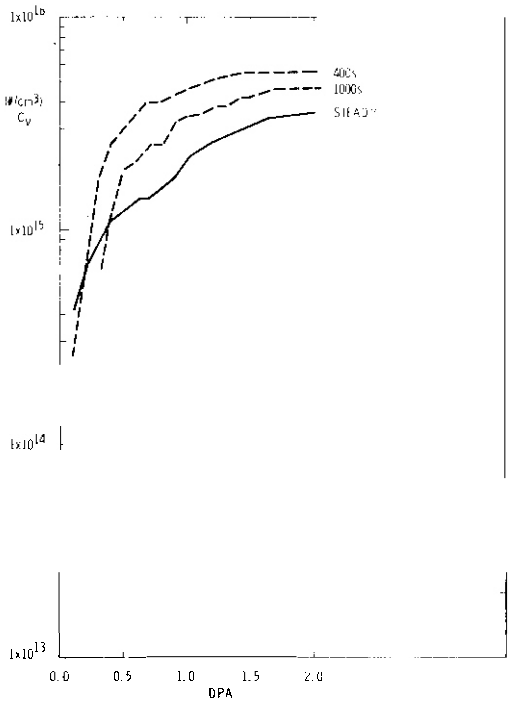

FIGURE 7. Fluence Dependence of Void Concentration for Several Pulse Periods at 540°C.

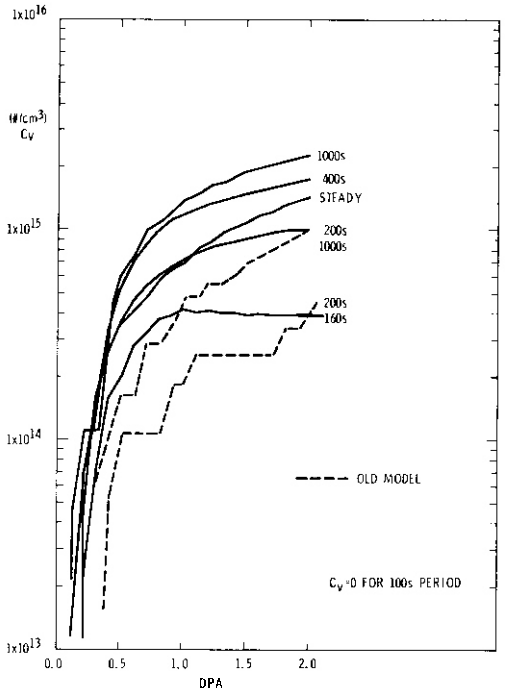

FIGURE 8. Fluence Dependence of Void Concentration for Several Pulse Periods at 550°C.

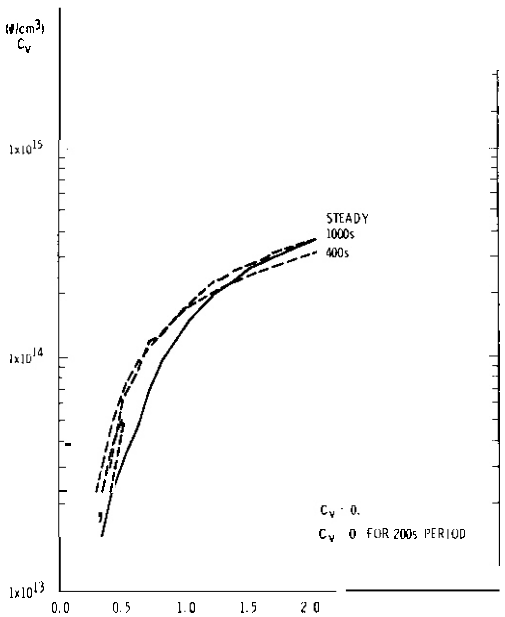

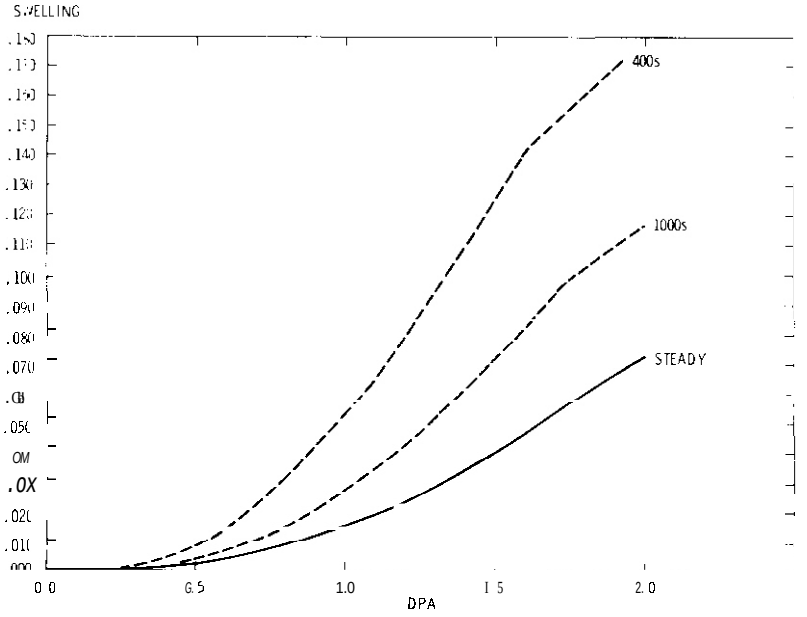

FIGURE 10. Fluence Dependence of Void Swelling for Several Pulse Periods at 540°C.

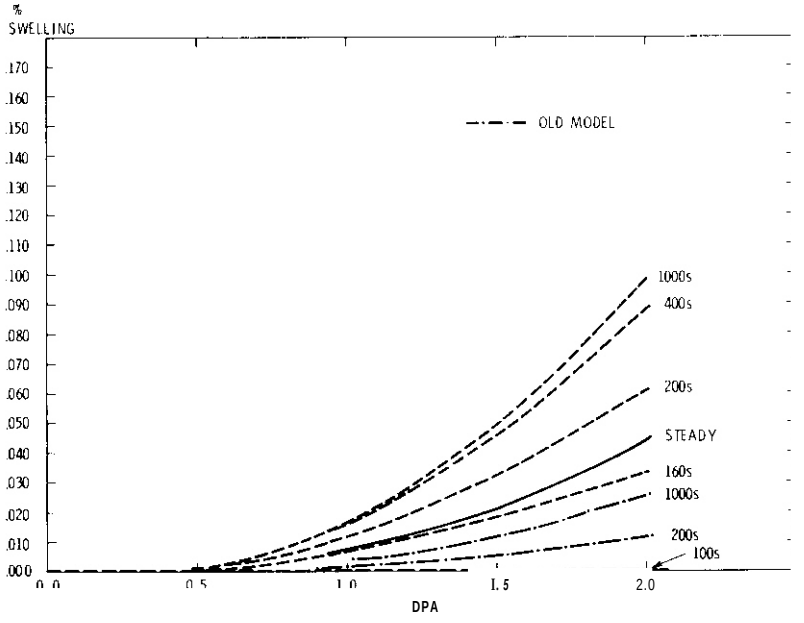

FIGURE 11. Fluence Dependence of Void Swelling for Several Pulse Periods at 550°C.

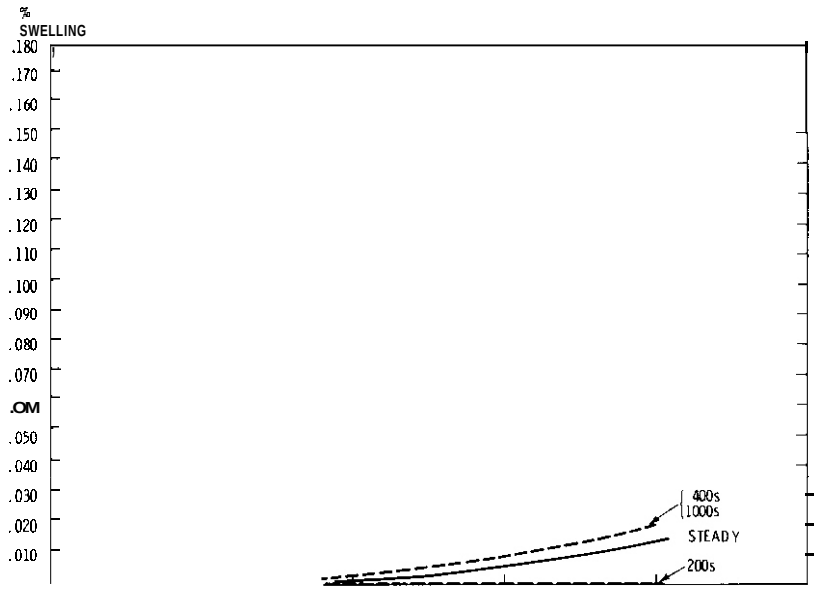

FIGURE 12. Fluence Dependence of Void Swelling for Several Pulse Periods at 560°C.

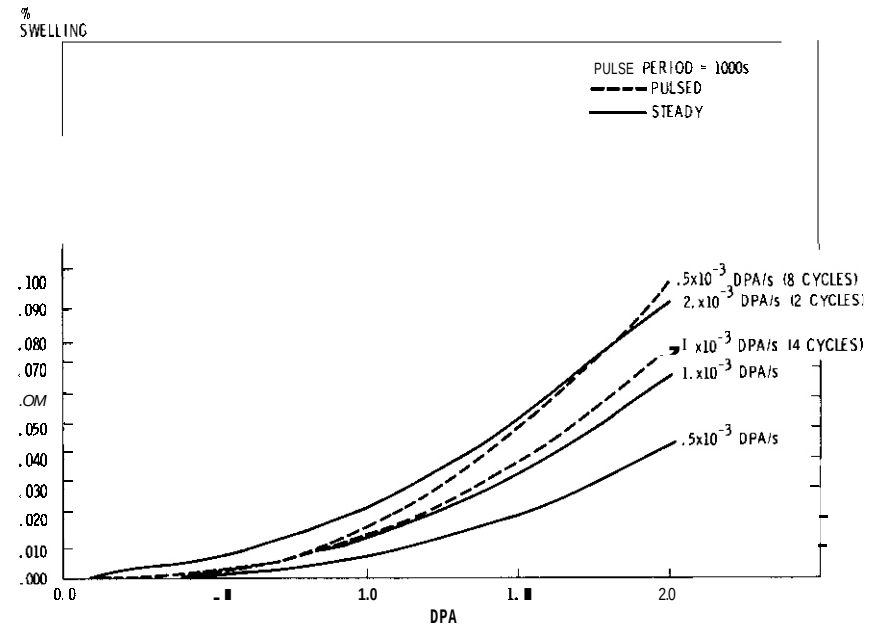

FIGURE 13. Fluence Dependence of Swelling for Several Damage Rates at 550°C Note that the pulsed and steady cases are indistinguishable at 2×10^{-3} DPA/s.

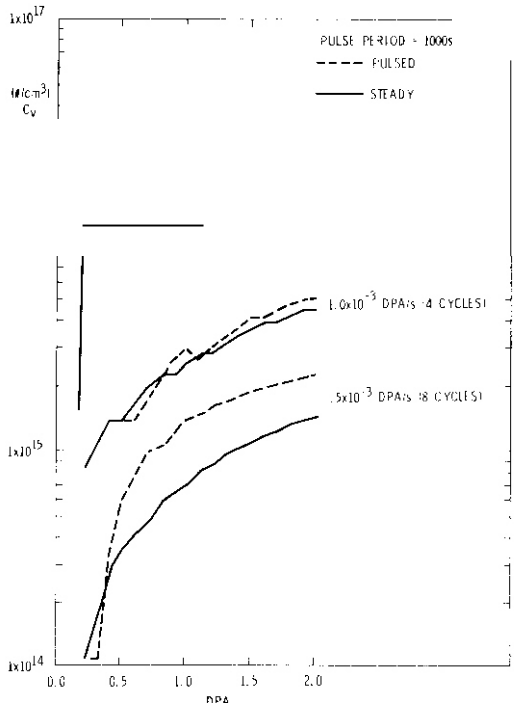

FIGURE 14. Fluence Dependence of Void Concentration for Several Damage Rates at 550°C.

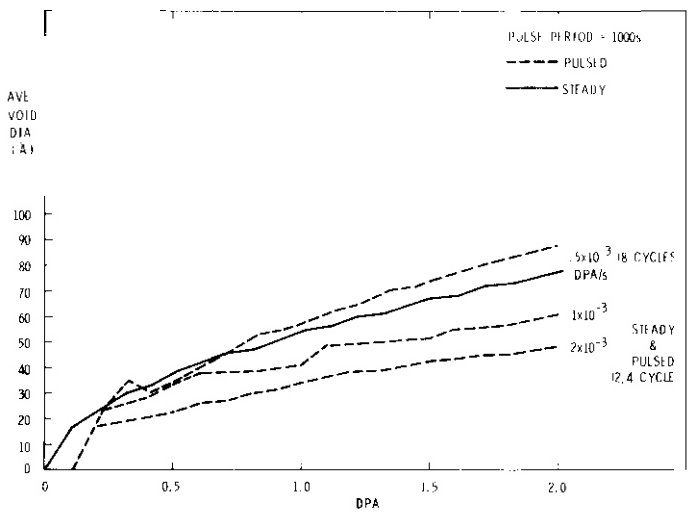

FIGURE 15. Fluence Dependence of Void Growth for Several Damage Rates at 550°C.

(5) $\bar{d}_v$ for pulsed irradiation approaches that of steady irradiation as the damage rate increases.

b. Effects on void density (C_v)

(1) C_v is greater than the steady irradiation value for some periods greater than T_c.

(2) C_v may increase or decrease with increasing period for periods greater than T_c, depending sensitively on temperature.

(3) C_v decreases as the temperature is increased and for periods greater than T_c approaches the steady irradiation value.

(4) C_v increases with damage rate.

(5) C_v for pulsed irradiation approaches that of steady irradiation as the damage rate increases.

c. Effects on swelling

(1) The swelling rates at 2.0 dpa are greater than steady irradiation values for some periods greater than T_c.

(2) The swelling rate may increase or decrease with increasing period; the sensitivity of the swelling rate to the period increases with decreasing temperature.

(3) Swelling rate decreases as temperature increases for both pulsed and steady irradiation.

(4) The dependence of the swelling rate on displacement rate is not monotonic because of opposing effects. The void concentration increases with displacement rate while the mean void size decreases (just as under steady irradiation). The magnitudes are such as to create a minimum in swelling rate near the intermediatedisplacement rate (1×10^{-3} dpa/s) used here. At higher displacement rates, the pulsed and steady irradiations produce higher (and essentially equal) swelling rates.

(5) As the damage rate increases, pulsed irradiation swelling behaved essentially the same as steady irradiation swelling.

5. Conclusions

This work has resulted in the establishment of some useful approximations and a model that agrees somewhat more closely with experimental observations than a previous model. The current model yields larger void concentrations under pulsed conditions than under steady irradiation for certain cycle periods. Throttling effects, however, were neglected which may have caused the void concentration for the shorter pulse period irradiations (<200 s) to be overestimated. In the earlier work, the inclusion of throttling produced the major differences between pulsed and steady irradiations. In the present work, significant differences were found even in the absence of throttling.

VI. REFERENCES

1. R. W. Powell and G. R. Odette, "The Effect of Pulsed HVEM Irradiation on Microstructure Evolution in a Simple Fe-Ni-Cr Alloy," HEDL-SA-1619, Proceedings First Topical Meeting on Fusion Reactor Materials, Miami Beach, Florida, January 29-31, 1979.

VII. FUTURE WORK

Experiments to determine the temperature dependence of the effects of cyclic irradiation are planned. Attempts to incorporate throttling into the revised model will continue.

VIII. PUBLICATIONS

None.

I. PROGRAM

Title: Simulating the CTR Environment in the HVEM

Principal Investigators: W. A. Jesser, R. A. Johnson

Affiliation: University of Virginia

II. OBJECTIVE

The objective of this work is to investigate the influence of temperature and helium-ion irradiation on the occurrence of deformation twinning during fracture of type 316 stainless steel.

III. RELEVANT DAFS PROGRAM TASK

Task II.C.13 Crack Initiation and Propagation

IV. SUMMARY

Unirradiated, austenitic stainless steel samples pulled to fracture are free from deformation twins when tensile tested at room temperature but contain deformation twins when tested at 600°C. Neutron-irradiated samples tested to failure at room temperature and elevated temperature are free from deformation twins. Helium-irradiated samples exhibit deformation twinning during fracture tests at 600°C. In summary, elevated temperatures or helium irradiation can promote the formation of deformation twins in stainless steel pulled to fracture while neutron irradiation does not significantly promote the formation of deformation twins.

V. ACCOMPLISHMENTS & STATUS

The Occurrence of Deformation Twinning during Tensile Testing of Type 316 Stainless Steel Irradiated *by* Helium Ions.

J. A. Horton & W. A. Jesser, Department of Materials Science, University of Virginia, Charlottesville, Virginia.

1. Introduction

It is commonly observed that high stresses are required to produce deformation twins. Consequently the idea of a critical stress necessary for twinning emerges. A large amount of work hardening permits high stresses to be reached. One finds that low temperatures and high strains are associated with high stresses, and hence lead to the occurrence of deformation twins[1,2]. The concept of a large critical stress for the initiation of deformation twinning suggests that the hardening produced by irradiation might promote the formation of deformation twins in irradiated materials. Contrary to this expectation, deformation twins apparently do not occur readily in irradiated material.

It is the purpose of this report to present selected conditions under which deformation twinning occurs in irradiated material during tensile testing at elevated temperatures.

2. Experimental Details

Tensile samples of type 316 stainless steel, shaped as ribbons with an electropolished central region transparent to 500 kV electrons, were pulled at elevated temperature in the high voltage electron microscope. Unirradiated samples as well as samples irradiated with 80 keV helium ions were tensile tested at 600°C. The crack propagation behavior was characterized in the HVEM and the fracture surfaces were characterized

in the SEM. For details of the equipment and tensile test conditions of similar, low-temperature deformation experiments, one may refer to previous DAFS reports. The flux and fluence of helium for the present experiments is typically near 3×10^{14} $cm^{-2}sec^{-1}$ and 3×10^{17} cm^{-2}.

3. Experimental Results

a. Twinning in Unirradiated Ribbons

Deformation twinning in type 316 stainless steel is not observed in samples tensile tested at ambient temperature. However, when the test temperature is elevated to 600°C, deformation twinning may occur in the very thin ligaments which form along the crack flanks during the last stages of fracture. In addition to the ligaments, coarse slip steps occur near the crack flanks in the thick regions of the sample. The ligaments which form tend to resemble "teeth" whose edges lie near low index direction and whose thickness is a few hundred angstroms. These teeth are present in both the low temperature as well as the high temperature tests; however, only the teeth formed during tensile deformation at elevated temperature contain twins. A micrograph of twin-containing teeth is shown in figure 1 which is from a group of 12 similar teeth in a row along the crack flank. A typical tooth from this group is selected for characterization and is labelled in the figure. The electron beam direction corresponds to $[\bar{1}10]$ and the main edge of the crack flank is near [111]. The tooth is shaped like a dog-leg having an obtuse, dog-leg angle of 145° between the [110] edge which extends from the crack flank and the adjacent $[11\bar{1}]$ edge of the ligament. Only that part of the tooth

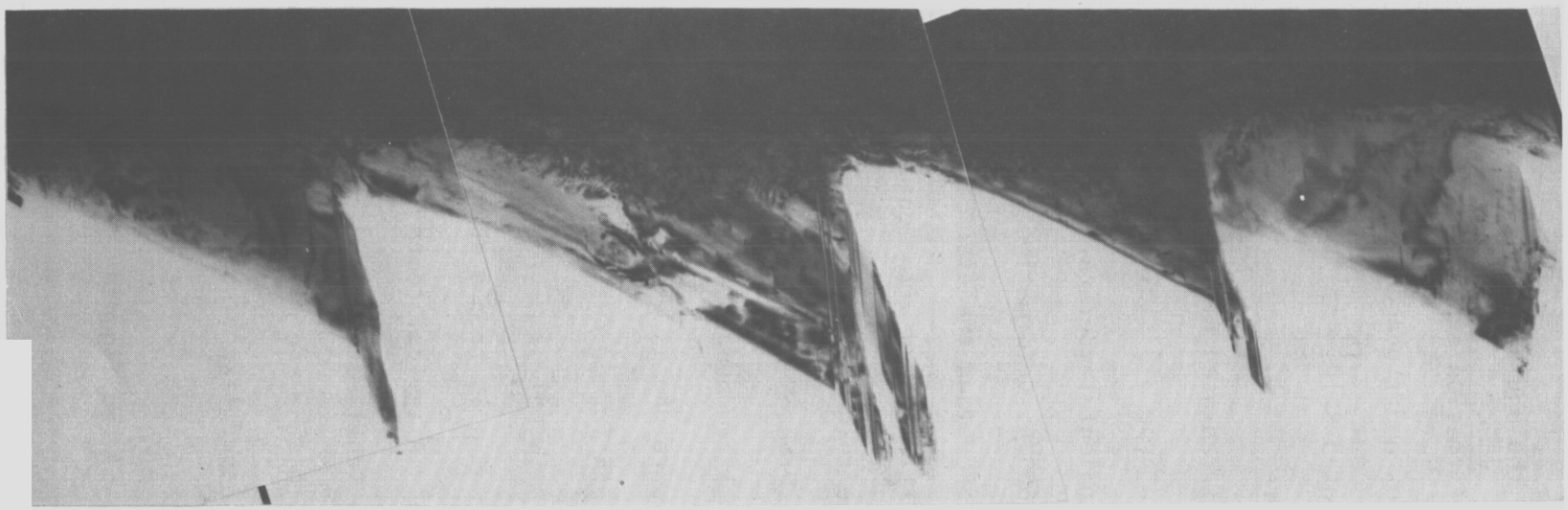

Figure 1. Transmission electron micrograph of ligaments along a crack flank in unirradiated type 316 stainless steel tensile-tested at 600°C. The crack flank direction is [111]. The film plane is (110).

bounded by this $[11\bar{1}]$ edge contains a significant number of twins all of which are long thin regions parallel to $[11\bar{2}]$.

The tensile axis was determined to lie along $[33\bar{4}]$ because many of the ligaments showed narrow regions which had necked-down to become parallel to $[33\bar{4}]$ with fracture edges normal to this direction. The tensile axis parallel to the $[33\bar{4}]$ direction is 16° from the main crack flank normal and gives rise to the highest Schmid factors of .336 on the slip systems $(1\bar{1}\bar{1})[01\bar{1}]$ and $(\bar{1}1\bar{1})[10\bar{1}]$ and of .485 on only one twin system $(\bar{1}\bar{1}1)[2\bar{1}1]$. The twin system which produced the twins in the ligaments is $(111)[11\bar{2}]$ and has a Schmid factor of .194 in this case. Clearly the simple consideration of a tensile axis and highest Schmid factor is inadequate to explain the results.

One can rationalize the formation of deformation twins on the $(111)[11\bar{2}]$ twin system with the lower Schmid factor when the overall nature of the teeth along the crack flanks is considered. The series of teeth are formed by slip processes which lead to a series of holes whose edges are parallel to low index directions, e.g. [110]. When the bridging material between two neighboring holes becomes narrow, high stress concentrations occur which may alter the stress state in the bridging ligament. Evidence for this modified stress state is found in the ligament of the selected tooth under consideration. Figure 2 shows a high magnification micrograph of the twinned region of the selected tooth. One observes that this region, which is 21 mm thick, has fractured along its length by the propagation of a small crack parallel to

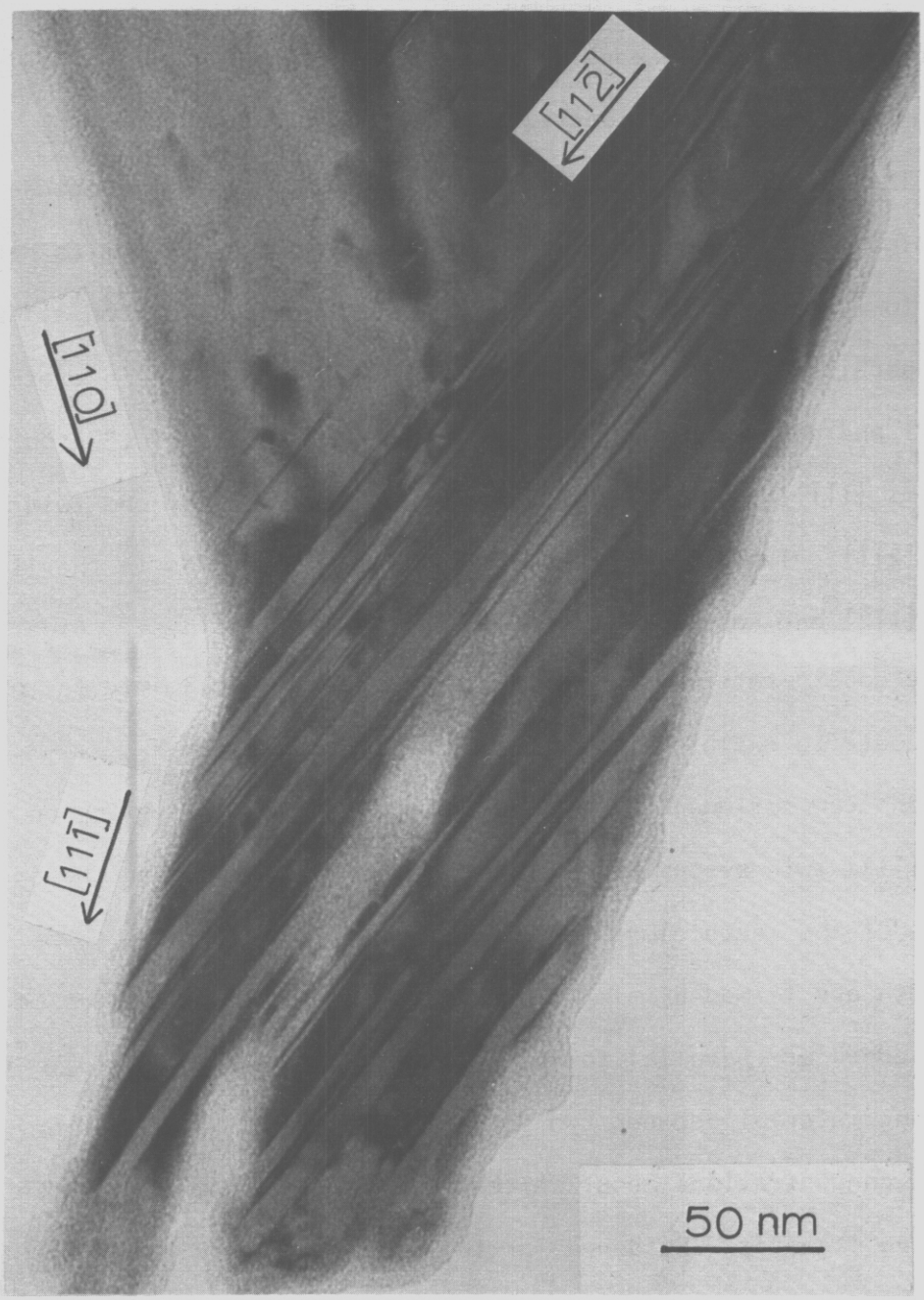

Figure 2. Transmission electron micrograph of a single "tooth" from figure 1. Note the set of parallel deformation twins and small crack in the ligament.

the direction of the tensile axis. Such a secondary fracture is consistent with a localized tensile stress in the film plane and nearly normal to the crack propagation direction, i.e. a localized tensile axis rotated from $[33\bar{4}]$ toward $[111]$. This effective localized tensile axis direction likely is near $[44\bar{1}]$ which corresponds to the axis having the maximum Schmid factor on the $(111)[11\bar{2}]$ twin system and thereby could account for the formation of twins on the $(111)[11\bar{2}]$ system.

The dog-leg angle of 145° may arise from a combination of the twin shear on $(111)[11\bar{2}]$ and conventional slip on the favored $\{111\}\langle\bar{1}10\rangle$ systems. The combined effect of the twinning shear and conventional slip could transform the edge direction $[110]$ of the tooth into the observed edge direction near $[11\bar{1}]$. A shear angle of 35° in the ligament plane is sufficient to accomplish the transformation. In order to determine the amount of this shear accommodated by the formation of the deformation twins, a dark field micrograph was produced from the twin reflection. A measurement of the cumulative twin thickness in the ligament showed that 53% of the ligament was twinned. The amount of shear accommodated by the twins is 10° and hence 25° of the shear angle remains to be accommodated by homogeneous slip. Evidence that homogeneous slip of the correct sign is present is found in the long edge of the tooth approximately parallel to $[110]$. This edge near $[110]$ is deformed from one end to the other through an angle of 10° in the same sense as that which carries $[110]$ into $[11\bar{1}]$. All of the teeth resembled each other in this respect and all of the dog-leg angles observed in the group of teethwerenearly equal to each other.

b. Twinning in Irradiated Ribbons

The occurrence of deformation twins in neutron-irradiated ribbons of type 304 stainless steel has not been documented here for either high-temperature tensile tests or tensile tests conducted at ambient temperature. There have been isolated observations of preexisting twins in some samples and these may act as sites for crack propagation. Indirect evidence obtained from the shape of the fracture edge and fracture surface suggests that twinning occurs during deformation of helium-irradiated stainless steel pulled at room temperature.

The first direct evidence for deformation twinning in irradiated type 316 stainless steel has been obtained for samples irradiated with 80 keV helium ions to a fluence of 3×10^{17} cm^{-2} and tensile-tested to fracture at 600°C. The mean, projected range of the 80 keV helium ions is near 282 nm; however, the depth beneath the entrance surface mechanically affected by the helium is observed to be much greater than the mean range. The thickness of the ribbon in the region containing twins is roughly 2000 nm. The twinned regions are detected by means of a combined secondary electron detector image and transmission electron image formed from the thick regions of the sample and the adjacent electron transparent regions. The shape of the sample surface combined with the selected area diffraction patterns of the thin regions permit one to determine with reasonable confidence the location and orientation of the twins. Figure 3 shows a scanning electron micrograph of the sample near the fracture edge. The crack flanks form a projected shape resembling an

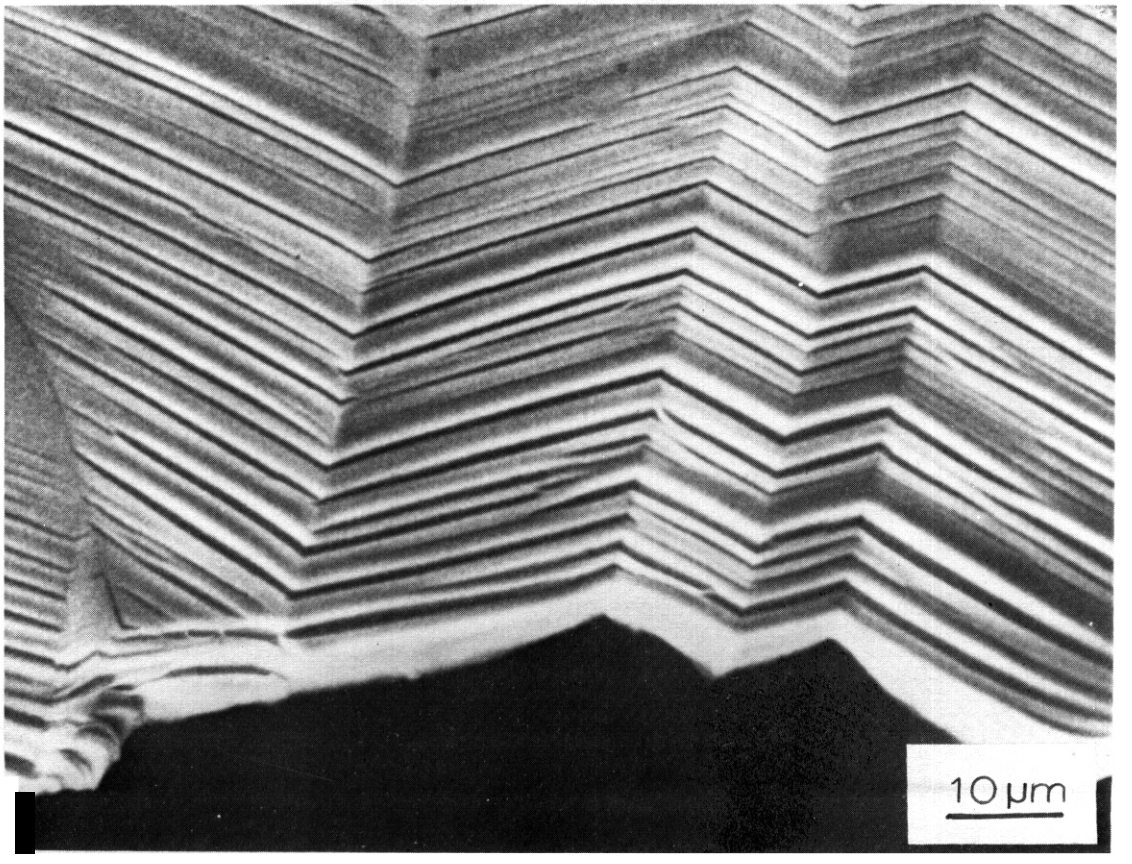

Figure 3. Scanning electron micrograph of a crack flank in type 316 stainless steel irradiated with helium ions of 80 keV to a fluence of 3×10^{17} cm^{-2} and tensile-tested at 600°C. Note the coarse slip steps and "roof-top" appearance associated with deformation twinning.

"M" with each segment of the fracture edge lying along <110> directions. This feature was confirmed from the diffraction patterns. The diffraction patterns further revealed that alternating regions of matrix and twin occur. The twin has its long axis along the $[11\bar{2}]$ direction which is normal to the average fracture edge which is [111]. The plane of the ribbon is $(1\bar{1}0)$ in the thin regions and likely is the same orientation in the nearby thick regions. A profusion of coarse slip lines along <110> are also visible in figure 3. The ribbon is not planar in the twinned region but resembles a roof top when viewed parallel to the plane of the ribbon and normal to the fracture edge, i.e. when viewed along $[11\bar{2}]$, the long axis of the twin. The ridge of the roof top is along $[11\bar{2}]$ and is elevated out of the average $(1\bar{1}0)$ plane of the ribbon so that an 8° angle is made between $(1\bar{1}0)$ and the plane of the "roof".

The tensile axis is apparently near $[11\bar{2}]$ which corresponds to the highest Schmid factor of .408 on the slip systems $(1\bar{1}\bar{1})[01\bar{1}]$ and $(\bar{1}1\bar{1})[10\bar{1}]$. The operation of these slip systems can account for the coarse slip lines along [110] in the matrix and the corresponding [110] in the adjacent twin. The formation of the twin with a coherent (111) plane intersecting the $(1\bar{1}0)$ surface along $[11\bar{2}]$ cannot be explained by a tensile axis near $[11\bar{2}]$. The operation of the slip system $(\bar{1}1\bar{1})[10\bar{1}]$ in a homogeneous manner may account for the 8° angle mentioned above; it would further cause a displacement of the fracture edge from its alignment along [110] to a new orientation rotated about 11° from [110]. This would result in the observed 130° angle between adjacent segments of the

"M" instead of the 109.5° angle expected between adjacent segments of the "M" in the absence of any slip in the twin or adjacent matrix. Clearly significant slip is occurring and the idea of a simple tensile axis, while sufficient to account for the slip, is inadequate to explain the twin formation. Just as with the teeth of the previous section, a tensile axis other than the "macroscopic" one was invoked to explain the results, here too a significant stress on the twin system $(111)[11\bar{2}]$ seems to require the presence of a modified localized stress.

The helium-irradiated samples showing "teeth" along the crack flanks did not reveal twins in the ligaments. The helium-irradiated samples formed twins only in thick regions. Observation of the top and bottom surfaces of the samples confirmed that the deformation twin extends through the entire thickness of the sample. Likewise, the coarse slip steps are found on both top and bottom surfaces of the matrix and also the twin.

4. Discussion

It was found that in unirradiated stainless steel, the thin ligaments which were pulled out from the crack flanks under conditions of high strain contained long narrow deformation twins, all parallel to each other, and roughly aligned with the propagation direction of a small crack in the ligament. Since cracks tend to propagate along directions normal to a tensile axis, the observation of a set of long deformation twins along a similar direction is consistent with previous observations in thin fcc crystals that often deformation twins form along a direction

normal to the tensile axis.[3-5]

From the shape and angles of the edges of the unirradiated and helium ion-irradiated stainless steel, one can conclude that both deformation twinning and homogeneous slip are present in the samples. The coarse slip steps on the top and bottom surfaces of the unirradiated and irradiated samples indicate that persistent slip on a very narrow packet of slip planes may also occur in these samples in a similar manner to that observed in unirradiated a-brass[6]. Further, from the lack of a macroscopic tensile axis providing a high Schmid factor on the twinning system, it is suggested that a uniaxial stress state is not present in these samples, but rather that at least a biaxial stress state is responsible for the deformation. The effect of irradiation by helium ions is to enhance the coarse slip and to promote the formation of deformation twins in the thick region of the sample while suppressing deformation twinning in the ligaments.

The minimum shear stress required to move a partial dislocation of Burgers vector, b_P, which creates an extended stacking fault behind the dislocation as it moves, is γ/b_P, where y is the stacking fault energy. If one takes the value of γ as that quoted for type 304 stainless steel, 21 ergs/cm^2, and an average Schmid factor of 0.4 on the twinning system, then the minimum applied normal stress required for deformation twinning is 360 MPa. The ultimate tensile strength of type 304 stainless steel neutron-irradiated to 40 dpa and tensile tested at 600°C is near 400 MPa which agrees with the above estimate of 360 MPa.[7] A stress of 400 MPa was

reached in a room temperature test of unirradiated type 316 stainless steel to a strain of 12% and in this case deformation twins were observed.[8] It would appear that deformation twins would be common if the critical stress criterion were a sufficient one. Venables proposed that the difficulty of nucleating twins accounted for their rarity in fcc crystals.' Matthews presented observations in thin films that agreed with this idea.[5]

It is tempting to approach the role of irradiation and the role of temperature on the formation of deformation twins from the point of view of providing nucleation sites for twin growth. In the case of the unirradiated samples, the combination of high strain, high temperature and available ligament edges for twin nucleation may allow the twins to nucleate and grow while the same conditions at low temperature may not lead to twin nucleation. In the case of the samples irradiated with helium ions, the high helium to dpa ratio may be favorable for twin nucleation and growth at the helium entrance surface where both helium concentration and dpa values are high. This suggestion is in agreement with results of Kohyama, who observed that deformation twinning accompanied blister formation in some helium-irradiated metals.[10] The effect of the helium irradiation on the pulled-out ligaments from beneath the surface is not clear but possibly the presence of helium in the thin ligaments hinders twin nucleation and growth.

5. Conclusions

In austenitic stainless steel samples pulled to fracture at elevated temperature, deformation twinning occurs in the ligaments of unirradiated

specimens and in the "thick" regions of specimens irradiated with helium ions. Deformation twinning is absent in neutron-irradiated samples tested under similar conditions to those of the helium-irradiated and unirradiated samples. It is also absent in the ligaments of helium-irradiated samples.

Homogeneous slip, inhomogeneous slip confined to a narrow packet of slip planes, and deformation twinning may occur in the sample regions near the fracture surfaces of unirradiated and helium-irradiated stainless steel. The exaggerated, inhomogeneous slip is enhanced at elevated temperatures in both unirradiated and irradiated samples.

The application of Schmid factors calculated from a "macroscopic" tensile axis and the concept of a critical shear stress for twinning may not be sufficient to account for the occurrence of deformation twins. The nucleation of twins may be the controlling factor.

VI. REFERENCES

1. R. E. Reed-Hill, The Inhomogeneity of Plastic Deformation, ASM, Metals Park, Ohio, 1971, 285.

2. J. A. Venables, Deformation Twinning, R. E. Reed-Hill, J. P. Hirth, and H. C. Rogers, eds., Gordon and Breach Sci. Pubs., NY, 1964, 77.

3. A. Catlin, W. P. Walker, and K. R. Lawless, Acta Met. 8, 1960, 734.

4. S. Maruyama and H. Kiko, Electron Microscopy, 6th Int. Cong. for El. Micro., Kyoto, 1966, R. Uyeda, ed., 1, 1966, 311.

5. J. W. Matthews, Acta Met. 18, 1970, 175.

6. H. G. F. Wilsdorf and J. T. Fourie, Acta Met. 4, 1956, 271.

7. D. R. Harries, J. Nucl. Mat. 82, 1979, 2.

8. J. A. Mazza, J. Iron and Steel Inst., Aug, 1966, 783.

9. J. A. Venables, J. Chem Phys. Solids 25, 1964, 685.

10. A. Kohyama, Univ. of Tokyo, private communication.

VII. FUTURE WORK

Further investigations into the relation between microstructure and fracture behavior in austenitic stainless steel are planned.

DISTRIBUTION

UC-20 (122)

UC-20c (80)

DOE/RRT-HQ (7)
Mail Stop B-107
Washington, DC 20545

Asst Director, Materials Tech
NA Oavies
JF Decker
PB Hemmig
KG Moses
RE Price
FT Scott

DOE/RL (3)
Richland, WA 99352

WA Burns
GM Chenevert
LA Pasquini

Argonne National Laboratory (3)
9700 South Cass Avenue
Argonne, IL 60439

LR Greenwood
A. Taylor
H. Wiedersich

Brookhaven National Laboratory
Associated Universities
Upton, NY 11973

Chairman, Nuclear Energy Dept

Columbia University
Plasma Physics Laboratorr
New York, NY 10027

RA Gross

General Atomic Company: (3)
P.O. Box 81608
San Diego, CA 92138

C. Baker
GR Hopkins
L. Rovner

Lawrence Livermore Laboratory (2)
University of California
P.D. Box 808
Livermore, CA 94550

MW Guinan
CM Logan

Los Alamos Scientific Laboratory (3)
University of California
P.O. Box 1663
Los Alamos, NM 87544

DJ Dudziak
CR Emigh
W. Green

Massachusetts Institute of Technology
Cambridge, MA 02139

L. Lidsky, Nuclear Engineering Dept

McDonnell-Douglas Astronautics
P.O. Box 516
St. Louis, MO 63166

D. Kummer

Mound Laboratory
P.O. Box 32
Miamisburg, OH 45342

Manager, Tech Appl and Development

National Bureau of Standards
Gaithersburg, MD 20760

CD Bowman

Naval Research Laboratory (2)
Metallurgy Division, Code 6390
Washington, DC 20375

I. Manning
JA Sprague

North Carolina State University
Department of Nuclear Engineering
Raleigh, NC 26707

JR Beeler, Jr.

Oak Ridge National Laboratory (7)
P.O. Box X
Oak Ridge, TN 37830

Director, Thermonuclear Div,
(Bldg 9201-2)
RJ Colchin, Bldg 9201-2
FG Perey
M. Roberts, Bldg 9204-1
JO Steigler
C. Weisbin
FW Wiffen

Pacific Northwest Laboratory (4)
P.O. Box 999
Richland, WA 99352

JL Brimhall
T. Chikalla
AB Johnson
LC Schmid

Princeton University (2)
Plasma Physics Laboratory
Forrestal Campus
P.O. Box 451
Princeton, NJ 08540

C. Osgood
K. Wakefield

HEDL (39)

HR Brager		W/A-57	FM Mann		W/F-429	RE Schenter	W/F-420
WL Bunch/			WN McElroy		W/C-39	JO Schiffgens	W/F-57
LL Carter		W/C-47	WN Nygren		W/A-58	FA Schmittroth	W/B-47
BA Chin		W/A-58	EK Opperman		W/A-58	RL Simons	W/A-57
DG Doran	(10)	W/A-57	NF Panayotou		W/A-53	AL Trego	W/E-15
FA Garner		W/A-57	RE Peterson		W/E-18	MJ Wilson	W/C-115
DS Gelles		W/A-57	RW Powell		W/A-57	GL Wire	W/A-38
RE Gold		W/C-39	WE Roake		W/E-2	Central Files	(5) W/C-110
HL Heinisch		W/A-57				Publ Services	(2) W/C-115

Rockwell International Energy Systems
8900 DeSoto Avenue
Canoga Park, CA 91304

D. Kramer

Sandia Laboratories (2)
Albuquerque, NM 37115

FL Vook (2)

Sandia Laboratories
Liverrnore, CA 94550

WD Wilson

University of Michigan
Nuc1ear Engineering Department
Ann Arbor, MI 48105

T. Kammash

University of Virginia
Charlottesville, VA 22901

WA Jesser

University of Wisconsin
1500 W. Johnson Drive
Madison, WI 53706

P. Wilkes

Westinghouse R&D Center (2)
Beulah Road
Pittsburgh, PA 15234

HR Holland
JA Spitznagel